UNIVERSITY OF CALIFORNIA
RIVERSIDE

Unraveling Fischer-Tropsch Chemistry with Density Functional Theory Calculation on V(100) and Other Catalysts

A Dissertation submitted in partial satisfaction
of the requirements for the degree of

Doctor of Philosophy

in

Chemistry

by

Yin Luo

March 2014

Dissertation Committee:

Dr. Gregory Beran , Chairperson
Dr. Chia-en Chang
Dr. Michael Pirrung

The Dissertation of Yin Luo is approved:

Committee Chairperson

University of California, Riverside

Acknowledgments

In the last five and a half years, I have been pursuing my Ph.D degree under the supervision of Professor Gregory Beran in Department of Chemistry at UC Riverside. The kinds of research frustrations on the way to the Ph.D degrees were not anticipated when I was a young undergraduate student, and even in my first three years here. At this moment that I could conclude my Ph.D project in the dissertation, I wish to express my sincere gratitude to all the people that bring me here.

First, I am really grateful to my advisor Dr. Gregory Beran, for his excellent guidance, caring, and patience and also building the harmonious research atmosphere in our group. Working under his guidance made me learn much as a researcher. The caring and patience make it possible that I finish the dissertation. I would like to thank my labmates, Dr. Kelly Theel, Dr. Kaushik Nanda, Dr. Shuhao Wen, Yuanhang Huang, Josh Hartman, Yonaton Heit, Nicole Godfrey, for their generous help.

I also wish to thank Dr. Francisco Zaera group, our experimental collaborator. To develop the better computational model, the discussions regarding the experiments with Professor Zaera, Dr. Xiangdong Qin and Huaxing Sun, are very helpful.

I also wish to thank all of my friends I have met during my study in UCR, who give me a warm memory in Riverside.

Finally, I would like to thank my parents. They are always there with me and help me through the good times and the bad times.

To my dear parents.

ABSTRACT OF THE DISSERTATION

Unraveling Fischer-Tropsch Chemistry with Density Functional Theory Calculation on V(100) and Other Catalysts

by

Yin Luo

Doctor of Philosophy, Graduate Program in Chemistry
University of California, Riverside, March 2014
Dr. Gregory Beran , Chairperson

Fischer-Tropsch (FT) synthesis has long been one of most important industrial reactions for synthetic fuel production, but much controversy still surrounds the nature of the hydrocarbon chain-propagation intermediates. A few years ago, temperature programmed desorption and x-ray photoelectron spectroscopy experiments provided surface science evidence for key vinyl intermediates on single-crystal V(100) surfaces, with methylene dehydrogenation as the rate-determining step. To understand the FT chemistry on V(100) and how it relates to FT chemistry on practical catalysts like cobalt or iron, we use density functional theory and microkinetic modeling to investigate the energetics and competition among different possible hydrocarbon product formation routes.

Focusing on the stepwise hydrogenation steps from surface carbide to methane gas product, the first project reconciles apparent discrepancies between the DFT predictions and the earlier experimental results, and it provides new insights into the methane formation mechanism on V(100). In the mechanism developed here, methylene dehydrogenation is fast, not rate-determining, as long as vacant surface

sites are available. Nevertheless, the resulting microkinetic model correctly reproduces the methane isotopic distribution obtained in temperature-programmed desorption experiments.

Next, the hydrocarbon-chain growth chemistry leading to C_1-C_3 (e.g. methane, ethylene and propene) is explored. In line with the popular alkenyl mechanism, vinyl intermediates are kinetically preferred over ethyl ones. However, we also find that the chain-growth pathway that couples methylidyne and methyl has even faster kinetics, suggesting that ethylidene may be another key intermediate in FT chemistry, at least on V(100). Comparison with DFT modeling results on Fe(100) suggests this pathway may also be important on more practical iron FT catalyst.

Contents

List of Figures

List of Tables

Chapter 1

Introduction

1.1 Fischer-Tropsch Synthesis

1.1.1 Background

Crude oil, a major fossil fuel, forms the mainstay of our energy supply. Fractionation, isomerisation and hydrogenation allow crude oil to be separated into many different kinds of hydrocarbon chemicals: gasoline ($C_4 \sim C_{12}$) with the boiling point between 80°C and 205°C as a primary fuel used in automobile engines in the short and medium term, diesel ($C_9 \sim C_{18}$) with higher boiling point 180°C $\sim$ 360°C used in aircrafts and ships, and also other heavier and higher boiling hydrocarbon mixtures for heating and in power stations. However, oil supply limits, decreasing stocks and rising price make it important to find replacements for conventional fuels. To directly and effectively function in current engine systems, such replacements must contain high proportions of hydrocarbons similar to those derived from crude oil. Therefore the possible sources of hydrocarbon fuel like

natural gas (mainly methane) and coal, have been intensively explored, as their reserves are currently estimated to be sufficient for 56 and 109 years,[1] compared to 53 years of global crude oil.[1]

Renewable sources like biofuels (mainly derived from carbohydrates produced in sugar or starch crops such as sugarcane and corn starch, and also from non-food sources such as agriculture and municipal waste)[2] and biomass (woody crops and similar bio-materials)[3] have increased in popularity. However the land area required to grow the crops and the time taken to renew the harvest on the scale needed, is problematic. Furthermore, significant arguments have been raised about whether biofuels are actually carbon neutral, and whether widespread biofuel adoptions could actually result in increased carbon emissions and thereby accelerate global warming,[4] contrary to the environmental-friendly intensions motivating their use.[5]

In this way, with technical problems limiting other energy alternatives such as solar, wind, tidal or nuclear power, hydrocarbon fuel synthesis from natural gas and coal has attracted substantial interest. Both the Bergius process developed in 1913[6] and the Karrick process invented in the 1920s[7] can produce synthetic fuels from hydrogenation of coal with hydrogen gas at 400°C to 500°C and 20 to 70 MPa hydrogen pressure, or with water steam at 450°C to 700°C in absence of air. However the Bergius process is expensive and consumes large quantities of water. The Karrick process is cheaper, requires less water and destroys less of the thermal value of coal than the Bergius process (only 25% of thermal value destroyed in the Karrick process, compared to about a half loss in the Bergius process), but it

has not been tested at large scale. Natural gas and coal both could extend the hydrocarbon-chain to liquid petroleum, termed coal-to-liquids (or CTL, as shown in Figure 1.1) and gas-to-liquids (or GTL, as shown in Figure 1.2).

Generally there are two stages in GTL process and indirect coal liquefaction in CTL process: (1) gasification to syngas (a mixture of carbon monoxide and hydrogen), and (2) subsequent conversion of the syngas into liquid hydrocarbon fuels. To distill out the syngas, gasification process on coal could be described by the following equations (reaction enthalpy data are derived from standard heat of formation ΔH_f°[8]):

$$\mathrm{C} + \mathrm{H_2O} \longrightarrow \mathrm{CO} + \mathrm{H_2} \quad (\Delta \mathrm{H} = 131.3 \mathrm{kJ/mol})$$

$$\mathrm{C} + \mathrm{O_2} \longrightarrow \mathrm{CO_2} \quad (\Delta \mathrm{H} = -393.5 \mathrm{kJ/mol})$$

$$\mathrm{CO_2} + \mathrm{C} \longrightarrow 2\mathrm{CO} \quad (\Delta \mathrm{H} = 172.5 \mathrm{kJ/mol})$$

The oxygen in these reactions must be supplied to provide energy to enable the endothermic steps to form carbon monoxide and hydrogen. Because coal is a refractory carbon-based polymeric solid that also includes S−, N−, P−, and heavy metal-containing (mercury Hg, arsenic As and selenium Se etc.) materials, all of which are environmentally harmful substances that need to be removed before fuel conversion,[9] the CTL process is both technically and chemically challenging.

Compared to coal, natural gas is much easier to clean up and offers a convenient source of methane through natural-gas processing by separating impurities and various non-methane hydrocarbons and fluids, including low molecular weight hydrocarbon compounds, e.g. ethane ($\mathrm{C_2H_6}$), propane ($\mathrm{C_3H_8}$), butanes ($\mathrm{C_4H_{10}}$),

Figure 1.1: Coal-To-Liquids: a process referred to as coal liquefaction which allows coal to be utilized as an alternative to oil. There are two different methods, direct coal liquefaction (left) and indirect liquefaction (right). Direct coal liquefaction: dry coal is mixed with recycled solvent to form coal slurry which is subjected to high temperature and high pressure in the presence of hydrogen gas and catalyst. The liquid products that are produced are of low quality and they require further refining to achieve high grade fuel products, e.g. the Bergius process developed in 1913[6] and the Karrick process invented in the 1920s.[7] Indirect coal liquefaction: the first step requires the gasification of coal to produce syngas (a mixture of CO and H_2 gas). The second step involves conversion of syngas into liquid fuels using methods like the Fischer-Tropsch process or methanol process.

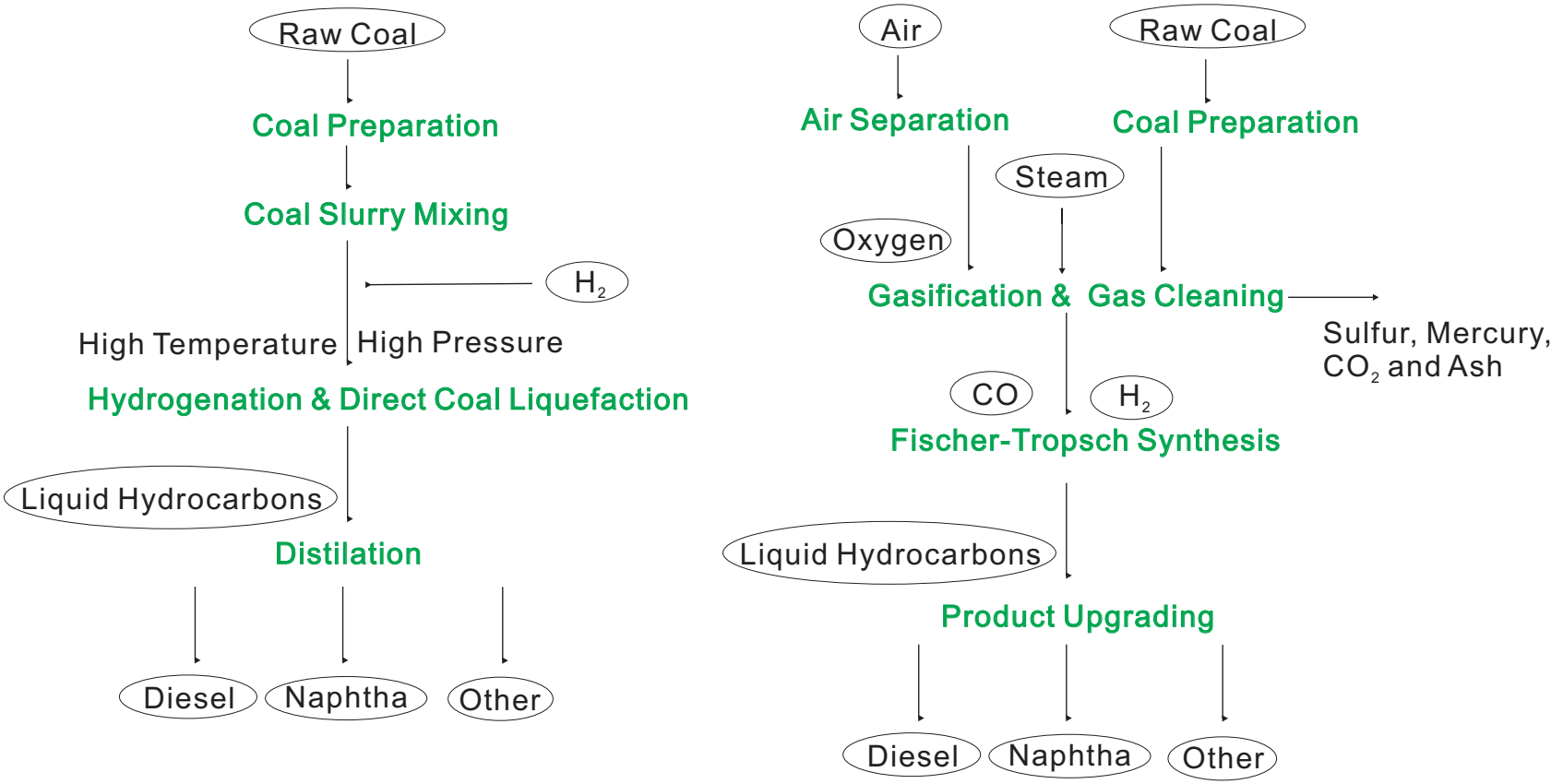

Figure 1.2: Gas-To-Liquids: a refinery process to convert natural gas into long-chain hydrocarbons such as ultra-clean gasoline or diesel fuel and other useful chemicals, through two stages (steam reforming to produce syngas and then conversion of syngas into liquid fuels by Fischer-Tropsch process etc.) followed by a product upgrading process.

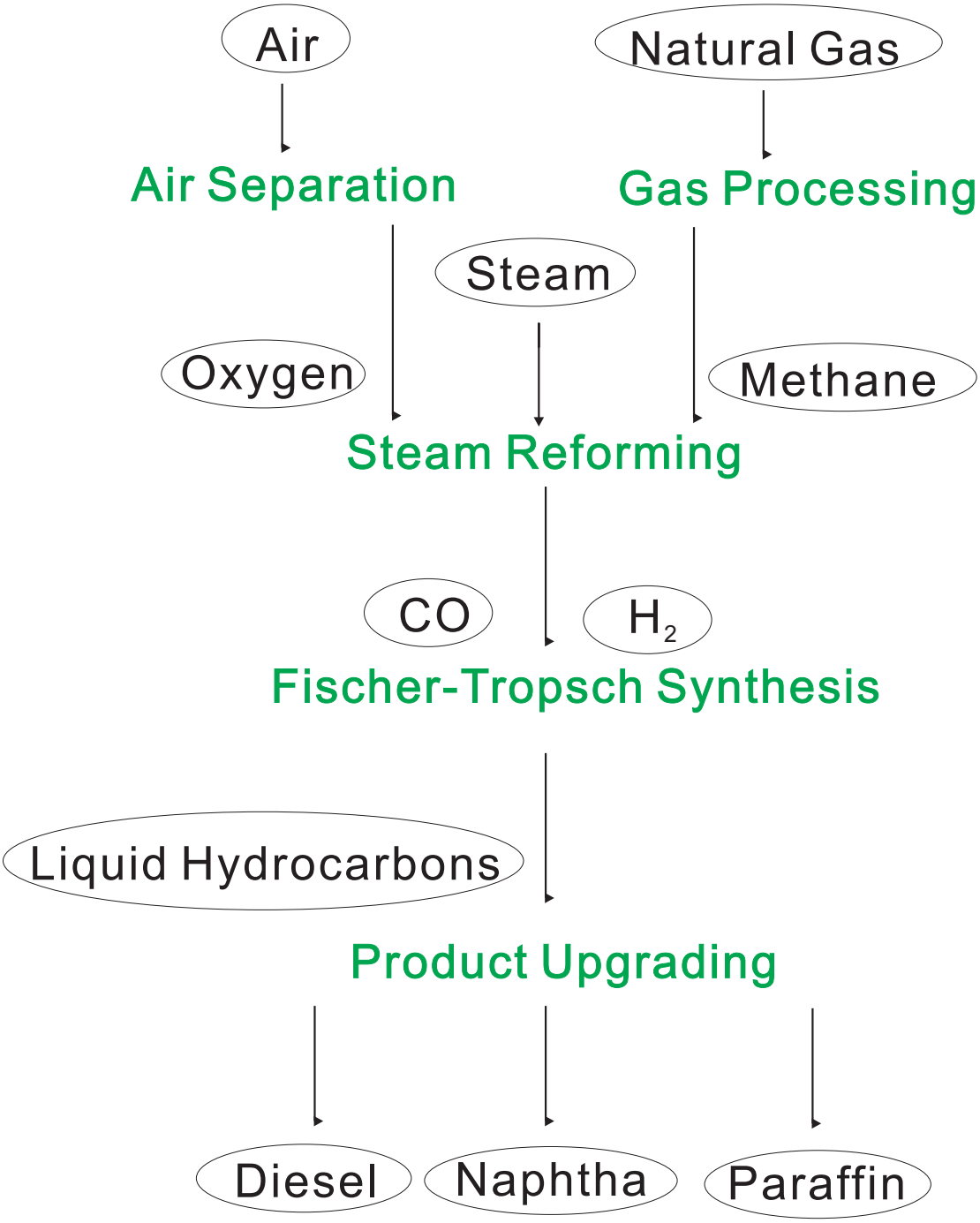

pentanes (C_5H_{12}), and other common contaminates such as water, carbon dioxide (CO_2) and hydrogen sulfide (H_2S). However, the major difficulty in the use of the fuel with low boiling point (-164°C) is transportation: natural gas pipelines are economical and common on land and across medium-length stretches of water (e.g. Langeled, Interconnector and Trans-Mediterranean Pipeline), but are impractical across large oceans; liquefied natural gas (LNG) carriers are used to transport across the ocean while tank trucks/trains can carry liquefied or compressed natural gas (CNG) over shorter distances. In this way, natural gas is preferred to be converted into liquid petroleum by the GTL process.[10] Natural gas is first converted into syngas via a steam reforming reaction (reaction enthalpy data are derived from standard heat of formation ΔH_f°[8]); and also a partial oxidation is needed to drive the process as the reforming is endothermic.[8]

$$CH_4 \ + \ H_2O \ \longrightarrow \ CO \ + \ 3H_2 \quad (\Delta H = 206.2 kJ/mol)$$

In the second stages of both CTL and GTL, syngas is converted either into liquid fuel or into valuable chemicals, e.g. methanol synthesis[11,12] to methanol and Fischer-Tropsch (FT) synthesis[13–15] to long-chain hydrocarbons. There are also other processes that lead to paraffinic hydrocarbons, e.g. some reactions analogous to FT, called Fischer-Tropsch-type reactions, to produce low-molecular-weight hydrocarbons in natural hydrothermal fluids under the ocean,[16] or to synthesize lipids under hydrothermal conditions.[17] Methanol synthesis and FT reaction both are heterogeneously catalyzed processes which have been applied in multi-million-tonne-scale facilities, when metallic iron or cobalt catalyst on an oxide support is used in FT and methanol is produced with copper-zinc oxide catalyst. Methanol

synthesis is now reasonably well-understood.[11,12,18] Here we focus on the relatively less understood FT reaction, which usually is carried out in steel reactors, at somewhat elevated temperatures and pressures, typically 100-300°C and 1-100 atmospheres, to mainly produce linear 1-n-alkenes together with methane, also some internal alkenes and n-alkanes,[19,20] according to,

$$3H_2 \ + \ CO \ \longrightarrow \ H_2O \ + \ CH_4$$

$$2nH_2 \ + \ nCO \ \longrightarrow \ nH_2O \ + \ C_nH_{2n}$$

FT synthesis was first commercialized in Germany during World War II. Being petroleum-poor but coal-rich, Germany used the FT processes to produce hydrocarbons as motor fuel. Fischer-Tropsch chemistry provided 90% of Germany's consumption in 1935-1945, and 9.1% of the total German oil supply.[21] And since the 1950s, the industrial side has been further developed with a series of plants operated by Sasol in South Africa, a country with large coal reserves, but little oil, using coal and now natural gas as feedstocks. Uncertainty in the supply of oil and its rising price have stimulated current industrial interest in FT synthesis. New plants are being commissioned widely, e.g. the largest GTL facility (named Pearl) is currently being constructed in Qatar by Shell, and new CTL facilities exist in China.[22] Besides ultra-clean gasoline or diesel fuel, FT synthesis also produces other useful chemicals, such as α-olefins, which are commercially significant feedstocks for the chemicals and polymer industries, and oxygenates (e.g. $2H_2 + CO \longrightarrow CH_3OH$ and $4H_2 + 2CO \longrightarrow H_2O + C_2H_5OH$). But even in the best cases, the FT process is rather unselective and produces a range of products. Thus many attempts are made to tune the reaction by developing strategies

to make individual compounds more selectively, and to boosting the efficiency by developing improved catalysts. A more detailed understanding of FT mechanism would greatly facilitate such improvements, but the mechanism of FT synthesis remains controversial a century after its discovery.[23]

Several different approaches have been developed to investigate the mechanism. One is the engineering-based macroscopic kinetic and thermodynamic analyses of the overall process which has been very successful in optimizing process conditions for reaction, summarized in reviews by Temkin,[24] Frennet and Hubert,[25] and Wojciechowski.[26] A second approach is the molecular-level investigation on surface reactions to specify reaction intermediates detected and characterized in the mechanism, summarized in reviews by Ugo,[27] Muetterties and Stein,[28] and Zaera.[19,29] Due to the short-lived nature of reaction intermediates and their minute amounts on metal surfaces, the processes occurring on catalyst surfaces are extremely hard to study directly. When most of experiments are performed under so-called ultra-high-vacuum (UHV) conditions (under pressure in the range of 10^{-9}-10^{-10} Torr), reactions of well-defined organometallic complexes are used to model individual steps, or single crystals with well-characterized structures are adopted in order to simplify surface studies, with a variety of surface-sensitive techniques.[30,31] The slow-energy electron diffraction (LEED) and surface-extended x-ray absorption fine structure (SEXAFS) are used for structural determinations. The characterization of electronic level could be figured out by ultraviolet photoelectron spectroscopy (UPS), x-ray photoelectron spectroscopy (XPS), and electron energy-loss spectroscopy (EELS). When high-resolution electron-loss spectroscopy (HREELS)

and reflection-absorption infrared spectroscopy (RAIRS) are used for vibrational studies, secondary ion mass spectroscopy (SIMS), Auger electron spectroscopy (AES) and ion scattering spectroscopy (ISS) could analyze compositions. Also temperature-programmed-desorption (TPD) is helpful on reactivity determinations. Such sophisticated spectroscopic and diffraction methods could identify many species on the surface that are proposed to be reaction intermediates. Different mechanisms have been suggested: some are reasonable and agree well with experimental observations, when others are more speculative.

With the efficient parallel algorithms for density functional theory (DFT) calculations in periodic systems and significant improvements in computer hardware, predictive modeling of heterogeneous catalysis has become possible in the past few years[32] (e.g. in industrial ammonia synthesis[33,34]). A third approach, theoretical computations, can tell us much about the difficult-to-measure process occurring on the surfaces to investigate the FT mechanism from *ab initio*[35–37] to DFT calculations.[38–53] Along any particular elaborate mechanism involving various intermediate species, one can calculate individual elementary reaction energetics and map them onto an energy profile network. Such DFT studies on FT chemistry have been performed a number of times, and a variety of potentially important reaction intermediates have been proposed based on these studies including C-CH, CH-CH, CH-CH_2, CH-CH_3 and CH_2-CH_3.

1.1.2 Mechanisms of Fischer-Tropsch synthesis

The hydrogenation of CO leads to similar mixtures of hydrocarbons over metals as different as iron, cobalt, ruthenium and rhodium.[54] Even nickel, which is too hydrogenating and chiefly a methanation catalyst, can yield higher hydrocarbons in certain circumstances, e.g. when supported on titanium(IV) oxide.[55] Overall, to produce alkenes and alkanes from the CO hydrogenation, C-C and C-H bonds are formed with the cleavage of C-O bond, when the formation of water might be a thermodynamic driving force. With the transition metal catalysts, most commonly cobalt, iron and ruthenium, FT synthesis begins from deoxygenation of the coordinated CO, assisted with hydrogen, to give H_2O plus a surface carbide (*C). The surface carbide is stepwise hydrogenated to surface methylidyne (*CH), surface methylene ($*CH_2$), surface methyl ($*CH_3$),[14,56] as illustrated in Figure 1.3. And methane formation is from the final hydrogenation on surface methyl.

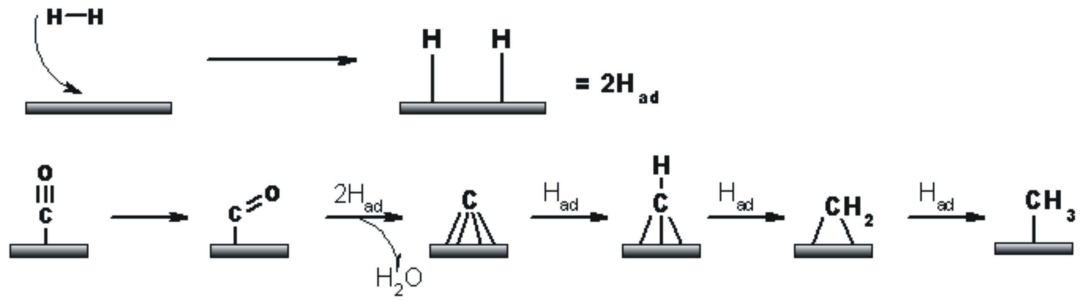

Figure 1.3: Generally accepted initiation steps in FT synthesis

Much of the debate surrounding the mechanism of FT synthesis concerns whether the hydrocarbon chain-growth steps occur via the so-called alkyl[57–62] or alkenyl mechanisms,,[23,63–67]as shown in Figure 1.4. Methylene surface groups

($^*CH_2$) are proposed as the starting intermediates to hydrocarbon chain growth. In the most-widely accepted alkyl mechanism, the $^*CH_2$ inserted into the metal-$^*CH_3$ bond to produce the ethyl ($^*CH_2CH_3$) intermediates. On the other hand, in the controversial alkenyl mechanism proposed by Maitlis,[23,66,67] the carbon-carbon coupling happens between $^*CH_2$ and $^*CH$ to form vinyl ($^*CH{=}CH_2$) intermediates. Additional alternative pathways have been suggested based on periodic density functional theory (DFT) studies on idealized metal surfaces. Hu's group investigated methane selectivity on Rh, Co, Ru, Fe, Re flat and stepped surfaces and argues that C-CH and CH-CH coupling might be preferred in the competition between hydrogenation to methane and hydrocarbon-chain growth, according to the estimation of effective barriers (ΔE_{eff}).[48,68–73] Ru(0001) surface is studied by van Santen group, which indicates that CH-CH_2 and CH-CH_3 are important.[35,74,75] Calculations of Ziegler group are focused on Fe(100) surface, which shows $^*CHCH_3$ (ethylidene surface species) might be a key intermediate from the energy profile.[38,76]

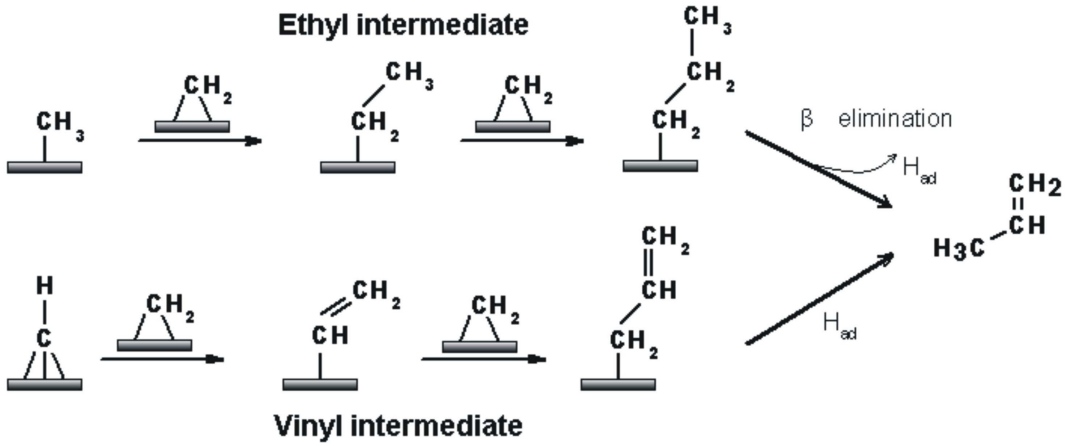

Figure 1.4: Potential hydrocarbon chain growth mechanisms

Recently, however, Shen and Zaera observed that the metallic vanadium (100) surface produces small amounts of propene through Fischer-Tropsch chemistry, with their ultrahigh vacuum temperature-programmed desorption (TPD) experiments.[77] They deduced the mechanism of propene formation by comparing propene TPD data obtained from different co-adsorption systems: no significant propene formation after co-adsorbing with CH_2I_2 is attributed to inactivity of ethyl and ethylene surface moieties; co-adsorption between vinyl and methylene or ethyne surface species that lead to considerable propene production might indicate the feasibility of a direct CH_2-$CHCH_2$ coupling, as a step in alkenyl mechanism. Also the dominant CH_2D_2 production in deuterium isotope labeling experiments initiated with $*CD_2$ might support the dissociation of methylene as the rate limiting step. The TPD and x-ray photoelectron spectroscopy (XPS) experiments provided the first strong surface-science evidence for the alkenyl mechanism, with vinyl formation and its coupling with methylene proposed to be the key propene formation steps.

1.2 Thesis work

Shen and Zaera's experiments (XPS and TPD) have been carried out in ultra-high-vacuum (UHV) chamber, the experimental conditions of which are very different from those in real heterogeneous catalytic reactions at moderately high temperatures and pressures (100-300°C and 1-100 atmospheres). The recognition of the 'pressure gap' emphasizes that results obtained from measurements under

Figure 1.5: Computational simulation used to connect vanadium experiments and practical FT synthesis: unifying the theoretical and experimental interpretations on V(100) surface, evaluation FT chemistries on V(100) and traditional FT catalysts (e.g. Co, Fe and Ru) based on theoretical computation, and unifying the theoretical and experimental interpretations traditional FT catalysts (e.g. Co, Fe and Ru).

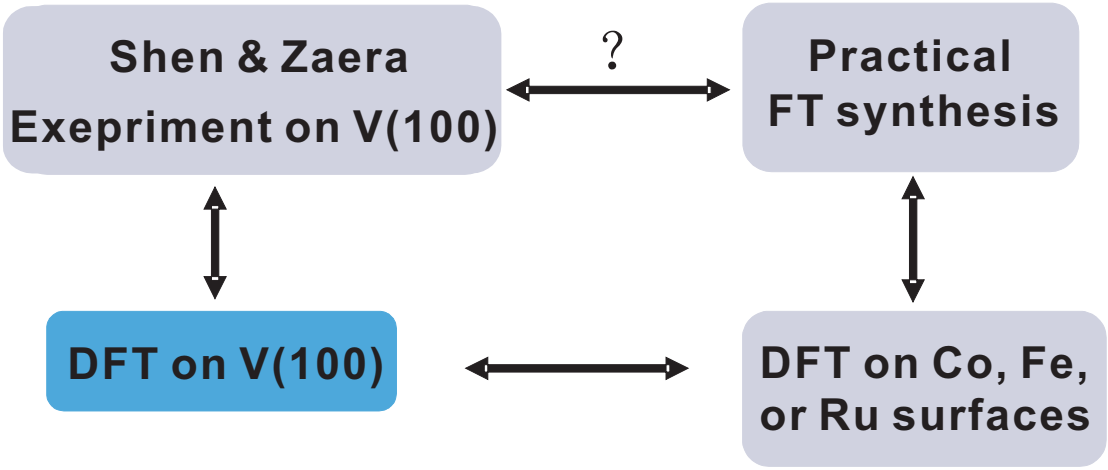

UHV conditions cannot automatically be expected to apply to the very different set of industrial conditions. Also the single-crystal metal surface could not describe the complicated conditions on the real catalyst particles, e.g. stepped areas, edges and defects. Furthermore, vanadium is a poor Fischer-Tropsch catalyst, so the significance of these experimental findings to practical Fischer-Tropsch synthesis is unclear, as shown in Figure 1.5. A coherent understanding of Fischer-Tropsch synthesis is needed to help connect Zaera experimental findings (vinyl intermediates) and practical FT synthesis chemistry, through alternative three step pathway: unifying the theoretical and experimental interpretations on V(100) surface, evaluation FT chemistries on V(100) and traditional FT catalysts (e.g. Co, Fe and Ru) based on theoretical computation, and unifying the theoretical and experimental interpretations traditional FT catalysts (e.g. Co, Fe and Ru).

Here we do not attempt to solve the problems of UHV condition and real cat-

alyst particles. Instead, we focus on the role of the metal. Compared to studies on complex real-world catalysts, the single-crystal, ultrahigh vacuum Zaera experiments provide an excellent opportunity of validating DFT predictions of the Fischer-Tropsch surface chemistry and unifying the theoretical and experimental interpretations, whether the alkenyl mechanism through vinyl intermediates is favored rather than alkyl mechanism through ethyl intermediates, or if there is a better explanation for experimental data on V(100). We seek to use DFT calculations and microkinetic modeling (1) to develop a detailed mechanism for propene synthesis on V(100) that can be validated against the ultrahigh vacuum experimental data, and (2) to assess the relevance of these vanadium experiments for chemistry occurring on the surfaces of traditional Fischer-Tropsch catalyst surfaces such as cobalt, iron and ruthenium. A number of DFT studies have been already performed to help understand the FT mechanism. Cheng, Hu and Ciobica et al.[69,78–80] investigated the selectivity between methane production and C_1-C_1 coupling on Fe, Co, and other traditional FT catalysts in terms of reaction energy profile and estimation of coupling rates. Lo and Ziegler[52,81–83] built the kinetic model to test factors, e.g. temperature, partial pressure of H_2 and CO, that influence methane production and also compare the C_1-C_1 and C_1-C_2 couplings on Fe surfaces. These studies will provide useful comparisons for our new vanadium results that will help us understanding the role of the metal on FT chemistry.

The work described in this dissertation can be divided into three parts, i.e. (a) methane formation on V(100); (b) propene formation on V(100); (c) FT chemistry on other traditional catalysts. There is an intimate relationship among these

three projects: at the beginning, the energetics and kinetics of methane formation on V(100) are examined, a set of TPD experiments with isotope-substituted intermediates is simulated using microkinetic model, which could reproduce the experimental data qualitatively; then the simulation could be applied to the hydrocarbon-chain growth process, represented by propene formation, to investigate the key intermediates, and ethylidene (*$CHCH_3$) is considered favored over vinyl and ethyl; finally, a general picture of FT chemistry is expected through the comparisons with other practical FT catalysts.

Chapter 2

Computational and Experimental Methods

2.1 Overview of computational scheme

The FT mechanisms involve many potential reaction steps with different gaseous and surface species. The computational approach used to model each of these steps is summarized in Figure 2.1. The first step is to optimize the geometries of reactants and products for each elementary reaction step. Individual reactants and products can either be gaseous or adsorbed on the surface. The second step is to find the transition state for each reaction. Because reaction coordinates for surface reactions can be complicated, the nudged elastic band (NEB) approach is used to identify the minimum-energy reaction pathway and obtain a guess for the transition state structure. The transition state structure is then refined through a series of constrained optimization and conventional transition

state searching. Third, harmonic vibrational frequency calculations are applied to confirm the nature of each transition state and to obtain thermochemistry data and reaction rate constants. Finally, microkinetic modeling is performed using the reaction rate constants and thermochemistry obtained from the DFT calculations. The microkinetic modeling provides insights into the potentially complex reaction mechanisms occurring on the surface. It also enables the simulation of the temperature-programmed desorption experiments, allowing for detailed comparisons between the model predictions and experimental observations. The next several sections describe each of these computational steps in detail.

2.2 Electronic structure calculations

The Fischer-Tropsch chemistry was modeled using planewave DFT calculations as implemented in the Dacapo software package.[84–86] The V(100) surface was modeled as a 2×2 unit cell (corresponding to 0.25 ML coverage of adsorbates, e.g. one *CH adsorbate per four binding sites on the vanadium surface in Figure 2.2) with a two-layer slab model first, and then upgraded to a four-layer slab. Species were adsorbed on only one side of the slab, and vacuum spacing equivalent to four vanadium layers separated successive periodic images of the slab. As vanadium exhibits no surface magnetic moment,[87–90] spin unpolarized calculations with the PW91[91,92] and RPBE functional,[93] were used. The valence electronic states were expanded in a plane wave basis with the energy cutoff of 340 eV, and core electrons were described by the ultrasoft pseudopotentials.[94] The Brillouin zone

Figure 2.1: Computational scheme for constructing the microkinetic model from DFT calculations. (1) The adsorbed structures of the reactants and products are computed. Harmonic vibrational frequency calculations are performed on these structures to confirm the stability of the structures (no imaginary frequencies) and to estimate enthalpies, entropies, and free energies. (2) NEB calculations are performed to identify the reaction coordinates and to obtain an initial guess for each transition state structure. (3) The structure of kinetically important transition states are refined through a series of constrained optimizations and conventional transition state searching. Harmonic frequency calculations are again performed to confirm the nature of the transition state (by the presences of a single imaginary frequency) and to compute thermochemical parameters. (4) The DFT reaction energetics and barriers are used to parameterize the microkinetic model. Microkinetic simulations are then used to understand the chemical mechanism and the temperature-programmed desorption experiments.

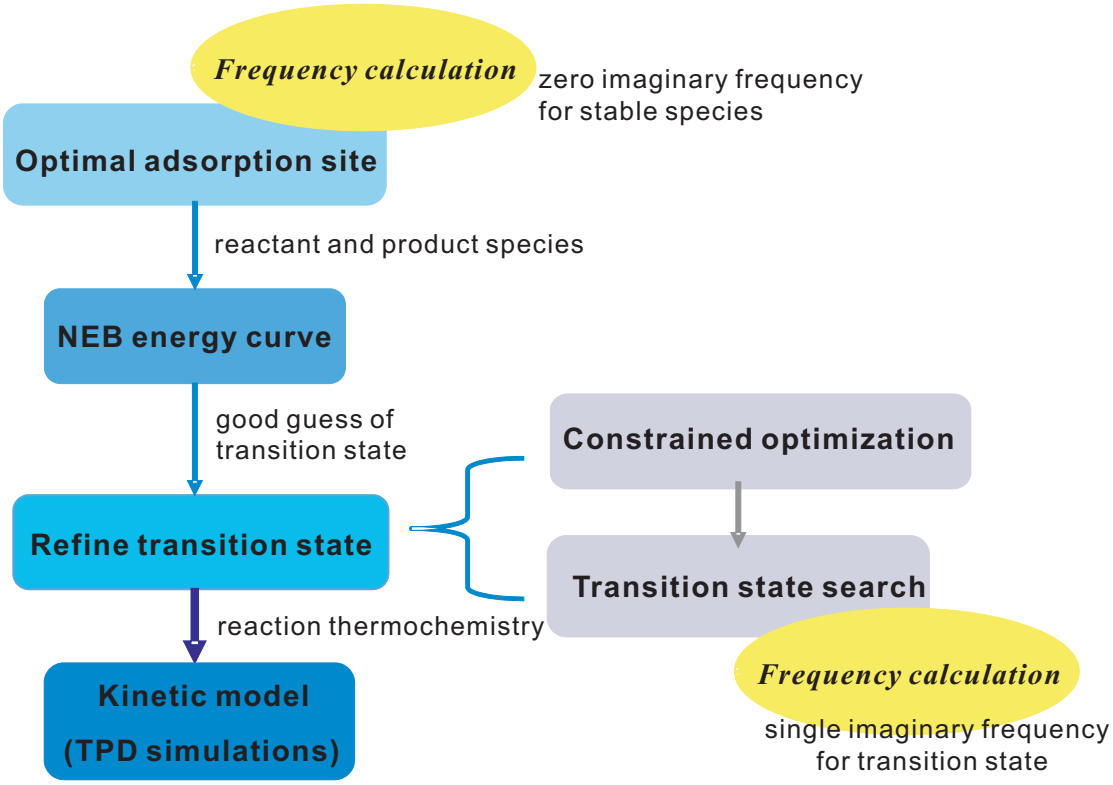

was sampled by a (4, 4, 1) k-point Monkhorst-Pack grid. Tests indicated that the results were reasonably converged with respect to basis and k-point sampling. As shown in Figure 2.3 and Figure 2.4, test calculations with higher planewave cutoffs and additional k-point sampling gave nearly identical results.

Figure 2.2: Only one four-fold site out of total four sites on 2×2 unit cell of V(100) surface is occupied by *CH molecule, which corresponds to 0.25 ML: top view (left), side view (right).

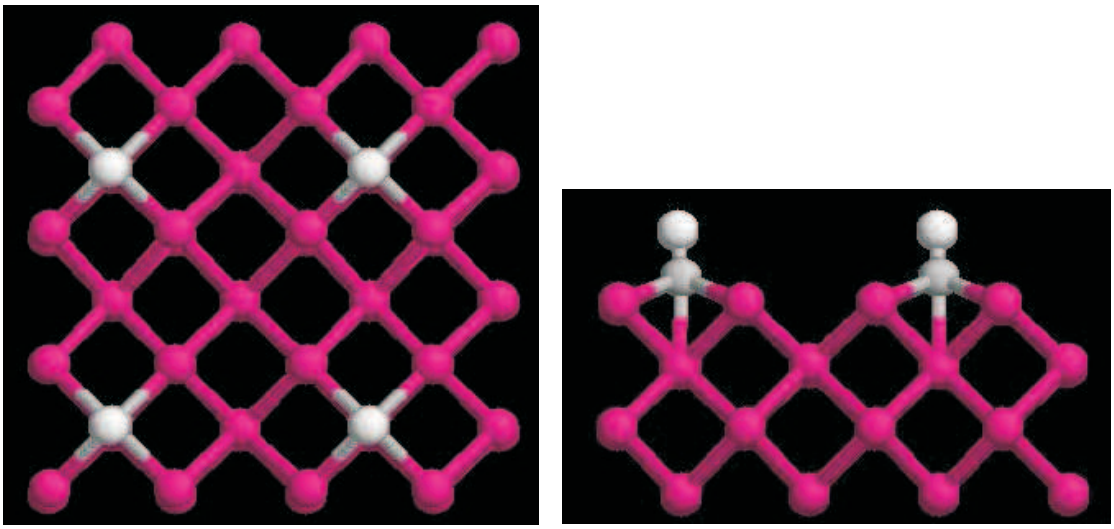

Figure 2.3: Convergence of the hydrogen adsorption on V(100) as a function of the planewave cutoff energy. The energies are well converged for cutoffs of ∼330 eV and higher, with variations below 0.0032 eV.

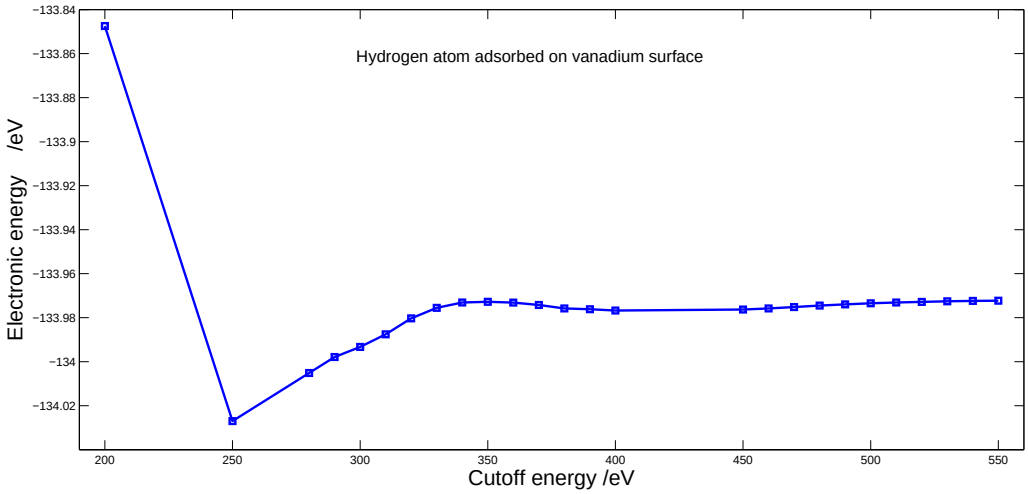

Figure 2.4: Convergence of the bare V(100) surface and adsorbed hydrogen adatom on V(100) as a function of the k-point sampling of the Brillouin zone. K-point samplings ranged from (2, 2, 1) Monkhorst-Pack grid to a (9, 9, 1) one. The (4, 4, 1) grid provides energies that are within 0.0173 eV and 0.0015 eV of the converged values for the bare V(100) surface and adsorbed hydrogen adatom, respectively.

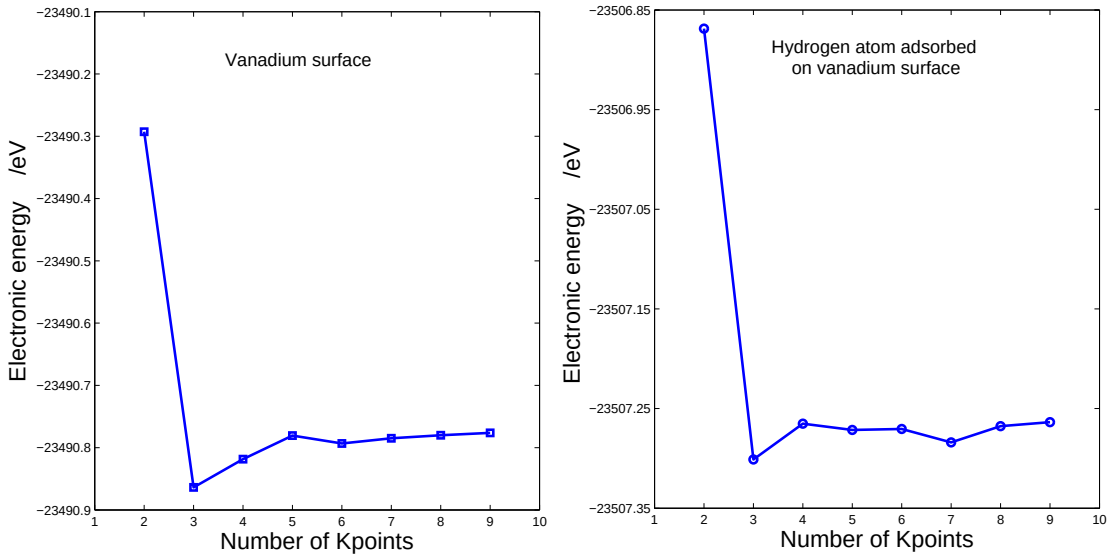

Starting from the two-layer vanadium slab model, geometries were optimized by relaxing adsorbates and atoms in the top surface layer. Atomic positions in the lower vanadium layers and the unit cell lattice parameter (a =3.03 Å[95]) were fixed at their experimental values (Figure 2.5). In general, the top-most layer are optimized to allow for surface relaxation, while the lower layers are constrained to the experimental positions to mimic bulk-like effects and minimize the artifacts introduced by modeling the true surface with a theoretical one that is only a few layers deep. For each adsorbate, three potential adsorption sites (on-top, two-fold, and four-fold) were investigated to determine the most stable binding sites. Unfortunately, while the two-layer slab calculations run quickly, the surface is too thin, which can sometimes lead to unphysical adsorption geometries and/or erroneous binding energies. Therefore, the low-energy structures identified on the

two-layer slab were refined using a four-layer slab model to obtain more reliable structures and energies, In the four-layer model, the top two metal layers were fully relaxed. Figure 2.6 and Table 3.1 show representative results from the four-layer model. Harmonic vibrational frequencies (at the Γ point) for key reaction intermediates and transition states were computed via finite difference, e.g. in Table 2.1 and 2.2.

Figure 2.5: Electronic energy profile of a clean vanadium(100) surface as a function of the unit cell parameter a. DFT predicts an optimal lattice parameters of $a = 2.99$ $\mathring{A}$, which is very similar to the experimental value[95] of $a = 3.03$ $\mathring{A}$. The computed energy difference between the predicted and experimental two lattice parameters is only 0.0234 eV.

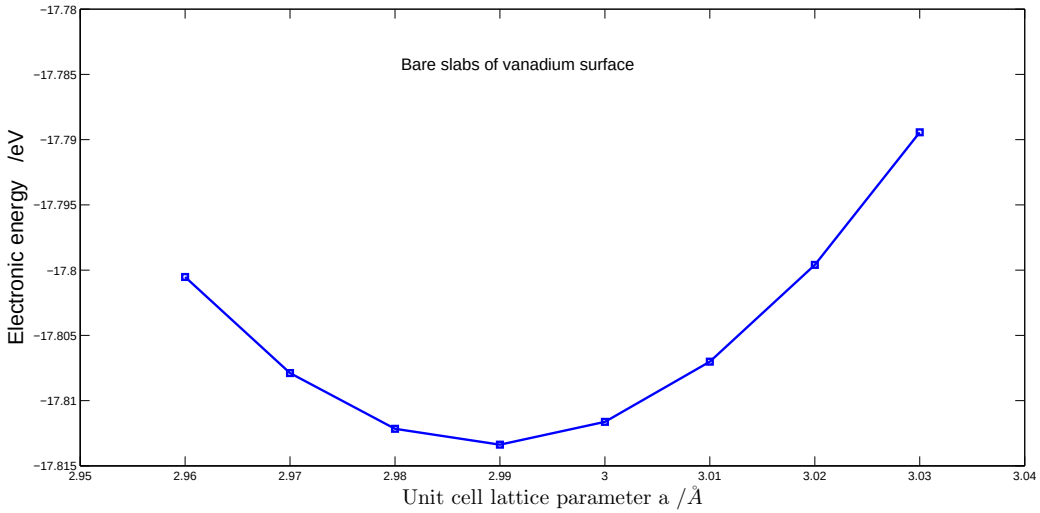

Figure 2.6: Further refinement of *CH_3 geometry on V(100) from a two-layer slab model to a four-layer slab model to obtain more accurate energetics.

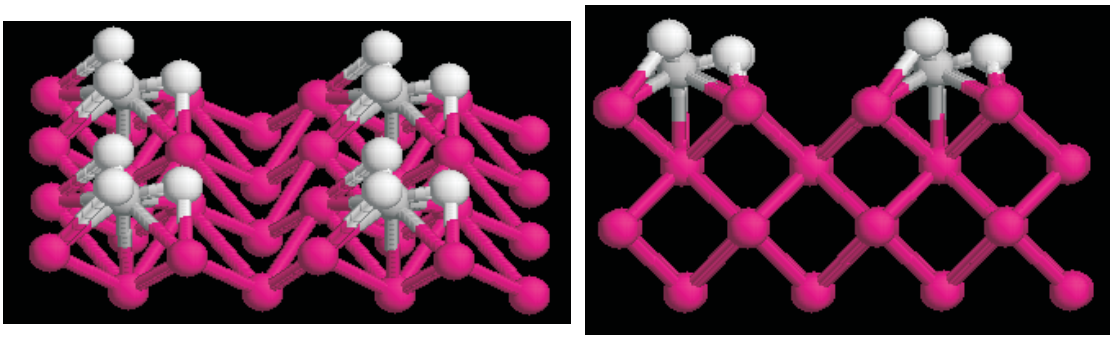

To locate transition states for each reaction, the nudged elastic band (NEB)[96–98] method was first used to identify the reaction coordinates and to find approximate transition states for the various surface reactions. The NEB method works by connecting a series of structures ('images') along the reaction path via a series of 'springs'. The total energy of the set of images is then minimized. The springs are used to maintain separation of the images along the reaction path (i.e. to prevent them all from optimizing into the reactant or product basins). This set of images provides an approximate Minimum Energy Path (MEP) for the reaction. In the limit of an infinite number of images, the NEB would produce the true MEP, and the maximum along this MEP would correspond to the reaction transition state. In practice, only seven images were employed in the NEB calculations performed here, and the highest-energy image provides only a guess for the transition state structure, as seen in Figure 2.7. While these approximate transition states are useful for investigating potential reaction pathways, further refinement of the transition states is required for important chemical reactions in the mechanism. To do so, a series of constrained optimizations were performed to scan the potential energy surface along the bond-breaking/forming coordinate in the vicinity of the transition state guess. The highest energy structure from these constrained optimizations was then used as a guess for conventional transition state searches. The resulting transition states were confirmed by the presence of a single imaginary harmonic vibrational frequency (e.g. Table 2.2).

Figure 2.7: NEB curve for hydrogenation of $*CH_2$: seven images are connected together to trace out a path between reactants ($*CH_2$ and *H) and product ($*CH_3$). The set of images is optimized down toward the minimum energy path. The geometry of saddle point (image 5) along MEP provides a good guess for the transition state.

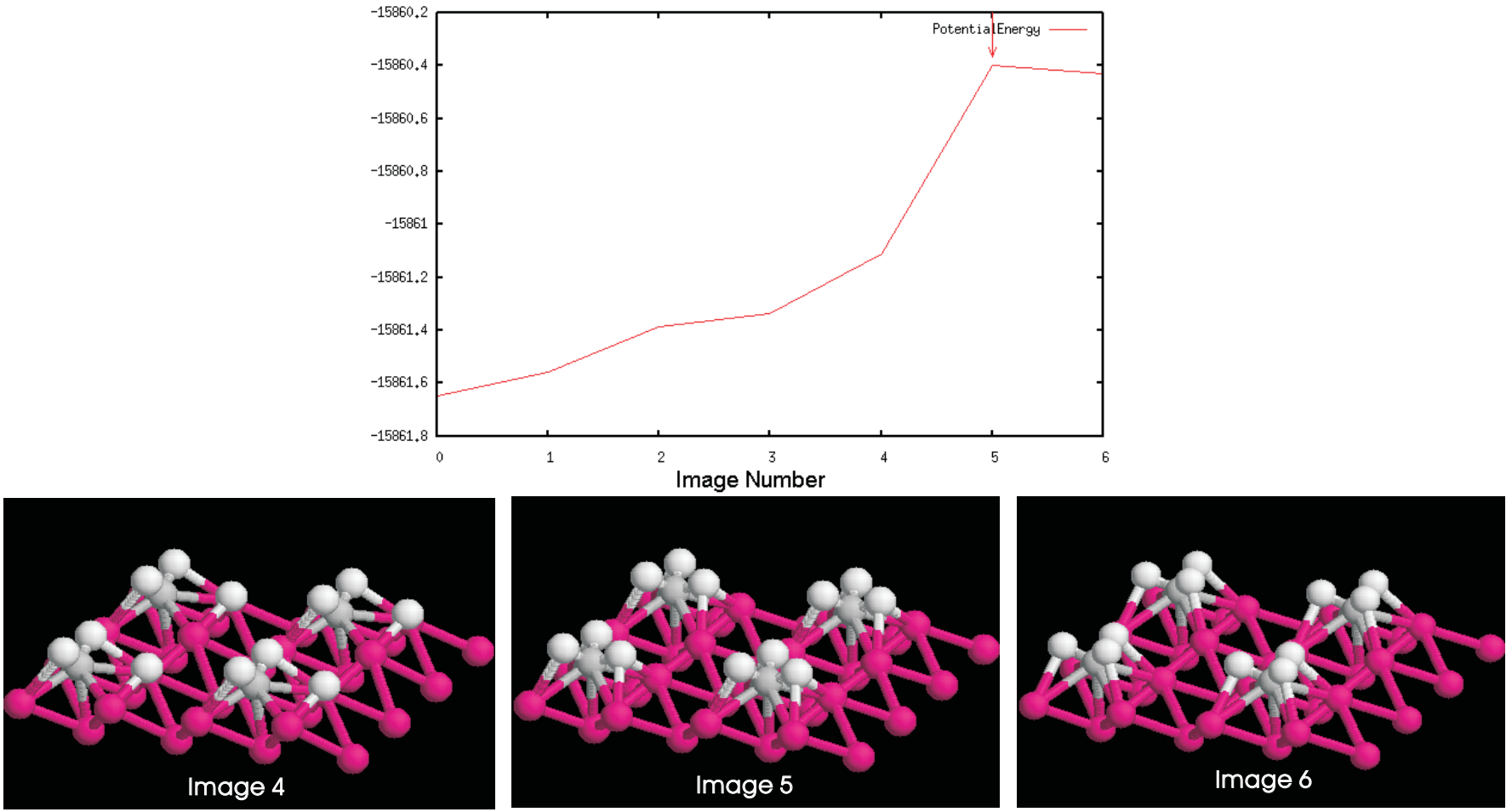

2.3 Reaction thermochemistry

The evaluation of reaction rates and thermodynamics (enthalpy, entropy, and free energy) requires the calculation of the partition functions for the species involved in the reaction. Standard ideal gas partition functions were used for gaseous species:[99]

$$\epsilon_{\text{tot}} = \epsilon_{\text{trans}} + \epsilon_{\text{rot}} + \epsilon_{\text{vib}} + \epsilon_{\text{elec}} \tag{2.1}$$

$$q_{\text{tot}} = q_{\text{trans}} q_{\text{rot}} q_{\text{vib}} q_{\text{elec}} \tag{2.2}$$

$$H_{\text{tot}} = H_{\text{trans}} + H_{\text{rot}} + H_{\text{vib}} + H_{\text{elec}} \tag{2.3}$$

$$S_{\text{tot}} = S_{\text{trans}} + S_{\text{rot}} + S_{\text{vib}} + S_{\text{elec}} \tag{2.4}$$

$$q_{\text{trans}} = \left(\frac{2\pi M k_B T}{h^2}\right) V \tag{2.5}$$

$$q_{\text{rot}} = \frac{\sqrt{\pi}}{\sigma}\left(\frac{8\pi^2 M k_B T}{h^2}\right)^{3/2} \sqrt{I_1 I_2 I_3} \tag{2.6}$$

$$q_{\text{vib}} = \prod_{i=1}^{3N_{atom}-6} \frac{e^{-h\nu_i/2k_B T}}{1 - e^{-h\nu_i/2k_B T}} \tag{2.7}$$

$$q_{\text{elec}} = \sum_{i=0}^{\infty} g_i e^{-\epsilon_i/k_B T} \approx g_0 e^{-\epsilon_0/k_B T} = g_0 \tag{2.8}$$

The total partition function can be written as a product of translational, rotational, vibrational and electronic terms. As enthalpy and entropy contributions involve taking the logarithm of partition function (q), the product of q's thus transforms into sums of enthalpy and entropy contributions. For each of the partition functions, the sum over allowed quantum states runs to infinity. However, as the energies become larger, the infinite summation can be written in a closed form. The above parameters include the total molecular mass M, volume of (ideal) gas V, three moments of inertia I_i, symmetry index σ (the number of proper symmetry

operations, e.g. σ =2 for H_2, 12 for CH_4, 4 for C_2H_4), vibrational frequencies ν_i obtained from harmonic vibrational frequency calculation, and degeneracy factor g_i with the same energy ϵ_i (e.g. g_0 is the electronic degeneracy of the ground state wave function).

For the adsorbates which are strongly bonded to the surface, as the three translational modes could be well described as a surface-adsorbate vibrational stretching mode, and two frustrated translations which behave like vibrations, the partition functions for the surface species were approximated as harmonic vibrational partition functions:

$$q_{vib} = \prod_{i=1}^{3N_{atom}} \frac{e^{-h\nu_i/2k_BT}}{1 - e^{-h\nu_i/2k_BT}} \tag{2.9}$$

Similar procedures have been used previously.[100] Enthalpies and entropies were calculated at 300 K and 1.0 bar. For the TPD simulations, free energies were computed as a function of temperature using the 300 K enthalpies and entropies according to $\Delta G(T) = \Delta H(300\ K) - T\Delta S(300\ K)$. Any temperature dependence of ΔH and ΔS away from 300 K was neglected.

When necessary, isotopic substitutions were treated by appropriately mass-weighting the Hessian in the harmonic vibrational frequency calculations, as the change in reduced mass affects the vibrational modes of species. In the cases where the adsorbate hydrogens were not equivalent, frequency calculation were applied to all possible isotopic substitution patterns. For example, $*CH_3$ in a four-fold site on the vanadium surface has non-equivalent hydrogens, there are three sets of frequency results related to $*CH_2D$ with all three possible D positions, listed

Table 2.1: DFT-computed vibrational frequencies of some gas-phase and surface species and intermediates at 0.25 ML coverage.

Species	Frequencies (cm^{-1})
	Gas-phase species
CH_4(g)	3120, 3119, 3117, 2999, 1512, 1512, 1295, 1294, 1292
H_2(g)	4431
	Surface species and intermediates
*C	1317, 1220, 1173, 1103, 851, 596, 541, 431, 406, 286, 243, 242, 223, 221, 220, 212, 203, 182, 178, 164, 157, 141, 131, 114, 104, 86, 83
*CH	2909, 529, 421, 417, 291, 277, 277, 236, 232, 224, 220, 213, 205, 200, 196, 196, 194, 178, 174, 163, 156, 147, 132, 128, 122, 102, 71, 68, 47, 38
*CH_2	2510, 2454, 1164, 762, 629, 480, 474, 385, 384, 289, 266, 257, 241, 238, 222, 220, 200, 198, 194, 192, 184, 180, 173, 172, 167, 164, 150, 140, 121, 110, 100, 74, 16
*CH_3	3020, 2927, 2862, 1376, 1334, 1153, 518, 431, 378, 305, 299, 278, 256, 252, 250, 239, 229, 218, 217, 213, 206, 204, 195, 187, 186, 181, 177, 160, 156, 151, 143, 132, 118, 109, 58, 52
*CH_3(4-fold)	2721, 2059, 1962, 1426, 1232, 1151, 769, 564, 367, 323, 300, 287, 269, 264, 262, 255, 241, 238, 225, 223, 209, 199, 191, 189, 177, 170, 158, 156, 153, 149, 146, 138, 113, 74, 61, 37
*H	1196, 1185, 386, 304, 291, 268, 255, 253, 243, 233, 233, 215, 214, 206, 202, 198, 187, 186, 183, 176, 173, 157, 155, 149, 131, 110, 37
*H_2	3392, 1167, 587, 293, 285, 277, 274, 251, 240, 224, 217, 209, 202, 196, 193, 185, 182, 176, 170, 167, 156, 152, 145, 140, 127, 126, 121, 106, 76, 69
H_2O*	3776, 3668, 1526, 446, 330, 293, 284, 281, 269, 262, 246, 224, 218, 214, 199, 195, 191, 188, 182, 177, 173, 171, 167, 158, 153, 153, 142, 140, 128, 110, 105, 103, 65
*OH	3774, 654, 481, 425, 303, 302, 279, 274, 265, 252, 238, 233, 227, 226, 208, 199, 190, 188, 178, 173, 160, 154, 148, 141, 132, 127, 118, 108, 100, 70
*O	466, 355, 356, 271, 271, 266, 248, 248, 238, 224, 217, 198, 198, 173, 173, 173, 167, 167, 163, 163, 152, 146, 144, 144, 109, 109, 104
V(100)	294, 290, 287, 284, 273, 237, 236, 232, 216, 206, 198, 194, 192, 190, 184, 183, 182, 175, 162, 158, 155, 154, 126, 124

Table 2.2: DFT-computed vibrational frequencies of the transition states for some elementary reaction steps at 0.25 ML coverage.

Reaction	Frequencies (cm^{-1})
Elementary reaction step transition states	
*C + *H $\longrightarrow$ *CH + *	**875***i*, 1266, 1084, 554, 551, 524, 302, 292, 278, 256, 247, 241, 241, 230, 226, 210, 207, 207, 194, 192, 187, 186, 170, 157, 141, 138, 128, 110, 100, 52
*CH + *H $\longrightarrow$ *CH_2 + *	**876***i*, 2832, 1147, 1075, 705, 477, 462, 426, 374, 313, 306, 287, 265, 261, 256, 252, 246, 241, 234, 226, 217, 212, 203, 199, 179, 174, 167, 154, 134, 106, 98, 88, 74
*CH_2 + *H $\longrightarrow$ *CH_3 + *	**998***i*, 3033, 2791, 1544, 1291, 846, 693, 540, 482, 384, 308, 297, 291, 278, 266, 253, 248, 242, 239, 231, 220, 211, 208, 199, 193, 184, 181, 174, 163, 152, 149, 142, 133, 132, 112, 105
*CH_2 + *H $\longrightarrow$ *CH_3(4-fold) + *	**330***i*, 2521, 2346, 1416, 1275, 1085, 1030, 795, 464, 392, 354, 311, 299, 285, 276, 267, 255, 250, 237, 234, 229, 207, 206, 195, 191, 189, 183, 174, 160, 156, 145, 129, 121, 119, 98, 45
*CH_3(4-fold) $\longrightarrow$ *CH_3	**137***i*, 2817, 2499, 2464, 1403, 1262, 1211, 726, 484, 367, 343, 307, 297, 275, 267, 249, 243, 241, 237, 230, 222, 212, 209, 197, 194, 188, 177, 172, 165, 162, 156, 149, 143, 137, 133, 81
*CH_3 + *H $\longrightarrow$ CH_4(g) + 2*	**1118***i*, 3061, 3019, 2921, 1478, 1382, 1352, 1164, 873, 670, 416, 334, 325, 316, 311, 297, 291, 253, 252, 239, 236, 231, 229, 220, 208, 199, 188, 187, 172, 170, 156, 154, 143, 135, 121, 113, 84, 80, 52
*H + *H $\longrightarrow$ *H_2 + *	**143***i*, 3532, 1094, 528, 297, 289, 268, 248, 242, 231, 227, 223, 218, 212, 205, 192, 188, 181, 173, 171, 164, 158, 151, 145, 140, 132, 121, 108, 88, 72
*H_2 $\longrightarrow$ H_2(g) + *	-
*O + *H $\longrightarrow$ *OH + *	**1272***i*, 920, 659, 565, 365, 317, 306, 304, 279, 274, 268, 264, 244, 240, 222, 213, 207, 205, 197, 189, 186, 177, 169, 161, 151, 142, 133, 108, 99, 67
*OH + *H $\longrightarrow$ H_2O* + *	**985***i*, 3672, 1178, 701, 535, 505, 334, 317, 300, 296, 275, 266, 257, 245, 239, 234, 212, 210, 206, 198, 193, 189, 186, 184, 178, 171, 170, 160, 148, 136, 130, 122, 69

in Table 2.3. This changes the resulting vibrational frequencies and partition functions, leading to different thermochemistry and rate constants depending on the isotopomers involved in a particular reaction, as shown in Table 2.4 with the example of thermochemistry difference with $*CH_3$ isotopomers.

Table 2.3: DFT-computed vibrational frequencies for isotopic substitutions with $*CH_3$ and $*CH_2D$: changes in the reduced mass change upon substituting hydrogen atoms with deuterium leads to different vibrational frequencies. $*CH_2D$ has three sets of vibrational frequencies due to the non-equivalent hydrogen positions.

Species	Frequencies (cm^{-1})
$*CH_3$(4-fold)	2721, 2059, 1962, 1426, 1232, 1151, 769, 564, 367, 323, 300, 287, 269, 264, 262, 255, 241, 238, 225, 223, 209, 199, 191, 189, 177, 170, 158, 156, 153, 149, 146, 138, 113, 74, 61, 37
$*CH_2D$(4-fold)	2721, 2014, 1466, 1278, 1190, 1027, 636, 519, 363, 310, 295, 285, 269, 263, 262, 249, 238, 238, 224, 218, 208, 199, 190, 188, 174, 169, 157, 156, 152, 148, 146, 138, 112, 74, 60, 37
	or 2721, 2004, 1473, 1280, 1190, 1028, 636, 519, 363, 309, 295, 285, 269, 264, 261, 249, 240, 236, 224, 218, 209, 199, 190, 188, 174, 169, 156, 156, 152, 149, 145, 138, 112, 74, 60, 37
	or 2061, 1987, 1961, 1423, 1089, 1034, 762, 485, 349, 295, 294, 285, 269, 263, 261, 249, 239, 237, 224, 218, 209, 199, 190, 188, 175, 169, 157, 155, 151, 148, 144, 137, 112, 74, 61, 37

Table 2.4: Thermochemistry data (zero-point energy correction, enthalpy correction, and entropy) for isotopic substitutions on $*CH_3$: the thermochemistry of $*CH_2D$ or $*CHD_2$ was calculated by averaging over all three possible D positions. Replacing hydrogens with deuteriums stabilizes these species enthalpically.

species	zero-point energy correction (eV)	enthalpy correction (eV)	entropy (meV/K)
$*CH_3$	1.082	1.531	2.912
$*CH_2D$	(1.015+1.015+1.010)/3	(1.469+1.469+1.464)/3	(2.941+2.941+2.948)/3
$*CHD_2$	(0.948+0.942+0.942)/3	(1.406+1.401+1.401)/3	(2.969+2.976+2.976)/3
$*CD_3$	0.874	1.337	3.002

2.4 Microkinetic modeling

2.4.1 Kinetics for elementary reaction step

To understand the FT mechanism and compare against the experimental data, a microkinetic model was constructed for the reactions on V(100). The microkinetic model parameters (rate and equilibrium constants) were calculated as a function of temperature from the predicted thermochemistry according to:

$$K_c(T) = e^{-\Delta G_{rxn}(T)/RT} \tag{2.10}$$

$$k_{for}(T) = \frac{k_B T}{h} e^{-\Delta G_{act}(T)/RT} \tag{2.11}$$

$$k_{rev}(T) = \frac{k_{for}(T)}{K_c(T)} \tag{2.12}$$

where $K_c(T)$ is the equilibrium constant, $k_{for}(T)$ is the forward reaction rate constant, $k_{rev}(T)$ is the reverse reaction rate constant, $\Delta G_{rxn}(T)$ is the reaction free energy, and $\Delta G_{act}(T)$ is the free energy of activation. As stated previously, the temperature variation of ΔH and ΔS was ignored when computing $\Delta G(T)$.

Surface reactions and gas desorption both take place in the FT process. For an elementary surface reaction, $*A + *B \rightleftharpoons *C + *vac$, where the asterix indicates a surface species and $*vac$ refers to a vacant surface site, the net reaction flux at temperature T is given by:[101]

$$flux(T) = r_{for}(T) - r_{rev}(T) = k_{for}(T)\theta_A\theta_B - k_{rev}(T)\theta_C(1 - \theta_{tot}) \tag{2.13}$$

In this expression, θ_i represents the surface coverage of species i and $(1 - \theta_{tot})$ gives the fraction of vacant sites on the surface.

For an elementary gas desorption reaction, $*A \longrightarrow A(g) + *vac$, the reaction flux at temperature T is given by:

$$desorption\ flux(T) = r_{for}(T) = k_{for}(T)\theta_A \tag{2.14}$$

And if it is an associated desorption, $*A + *B \longrightarrow C(g) + 2 * vac$, the reaction flux at temperature T is given by:

$$desorption\ flux(T) = r_{for}(T) = k_{for}(T)\theta_A\theta_B \tag{2.15}$$

In both cases, we assume the UHV pumps out gaseous products, so we neglect the potential for re-adsorption.

Generally, the reaction flux for any elementary step j could be expressed like:

$$reaction\ flux_j = k_{for,j}\prod_{l=1}^{S_{\mathrm{R}}}\theta_l^{-\nu_{j,l}} - k_{rev,j}\prod_{l=1}^{S_{\mathrm{P}}}\theta_l^{\nu_{j,l}} \tag{2.16}$$

where $\nu_{j,l}$ is the stoichiometric coefficient of species i in reaction j; $k_{for,j}$ and $k_{rev,j}$ are the rate constants for the forward and reverse reaction j that could have been estimated by thermochemistry data; θ represents the variable of species surface coverage. As the product formation rate and reactant consumption rate are both proportional to the reaction flux rate, gaseous species and stationary surface species are treated using the following formulation,

$$\frac{\mathrm{d}\theta_i}{\mathrm{d}t} = \sum_{j=1}^{\mathrm{no.rxns}}\nu_{j,i}[k_{for,j}\prod_{l=1}^{S_{\mathrm{R}}}\theta_l^{-\nu_{j,l}} - k_{rev,j}\prod_{l=1}^{S_{\mathrm{P}}}\theta_l^{\nu_{j,l}}] \tag{2.17}$$

In this way, the complete set of time-dependent ordinary differential equations (one for each gaseous or surface species) with variables of all species concentrations (or surface coverages θ_i), is solved using a stiff ordinary differential equation solver

(`ode15s` in Matlab), time stepping to steady state for a specified reaction time. The DFT-predicted thermochemistry is combined with the microkinetic model to estimate rate constants for each elementary reaction step. For the simulations of methane formation with isotopic labeling (Chapter 3), twenty-eight gaseous and surface species and thirty-five reactions are included in the model, as shown in Table 3.2. For the propene formation mechanism discussed in Chapter 4, the microkinetic model covers twenty-four gaseous and surface species and twenty-eight reactions, as shown in Table 4.3. If one includes isotopic substitutions, the reaction mechanism expands to include sixty-one gaseous and surface species and ninety reactions. The structure of microkinetic model code in Matlab is illustrated in Appendix A. And the sets of differential equations used to simulate methane and propene formation are listed in Appendix B and C.

2.4.2 Temperature-programmed desorption simulation

Many of the key observations in the Shen and Zaera experiments originate from TPD experiments, which allow one to observe how the surface chemistry changes as a function of initial species concentrations and temperature.[101] Therefore, we simulate the TPD experiments in order to validate the DFT-predicted mechanism. The experimental TPD was conducted in an ultra-high-vacuum (UHV) chamber evacuated with a turbo-molecular pump to a base pressure of about $2\times10^{-}10$ Torr, and a mass spectrometer was employed to detect and identify the surface reaction products by recording the time evolution of the partial pressures of different masses.[77,102] Figure 2.8 shows a typical TPD process. The sample gas is initially

dosed on to the single-crystal metal surface at low temperature. Then the system is heated at a constant rate β, stimulating surface reactions and gaseous product desorption. In a TPD spectrum, the peak height indicates the desorption rate, while the integral over the peak (i.e. its area) corresponds to the total amount of gas desorbed. The temperature in TPD simulation is time-dependent, as shown in Equation 2.18. Therefore, the reaction thermochemistry and rate constants in the kinetic model must be re-evaluated repeatedly as the temperature changes, as indicated in Equation 2.19, where $k_{for,j,T}$ and $k_{rev,j,T}$ are rate constants for the forward and reverse reaction j at the specified temperature or at the certain time step.

$$\mathrm{d}T = \beta \mathrm{d}t \tag{2.18}$$

$$\frac{\mathrm{d}\theta_i}{\mathrm{d}t} = \sum_{j=1}^{\text{no.rxns}} \nu_{j,i}[k_{for,j,T} \prod_{l=1}^{S_\mathrm{R}} \theta_l^{-\nu_{j,l}} - k_{rev,j,T} \prod_{l=1}^{S_\mathrm{P}} \theta_l^{\nu_{j,l}}] \tag{2.19}$$

When simulating Shen and Zaera experimental TPD results, two aspects of the chemistry neglected in the microkinetic model merit discussion. First, in the TPD experiments, the initial methylene intermediates were produced by thermal activation of diiodomethane, CX_2I_2(g) (X = H or D), which is used as a precursor and decomposes to *CX_2 and *I on the surface. Based on previously reported experiments,[103] the surface iodine appears to be fairly non-reactive — iodine-containing products like methyl iodide were observed only after high CH_2I_2 exposures. It may, however, occupy surface adsorption sites, until it either desorbs or diffuses into the bulk at high temperatures ($>$ 1000 K.)[102] To avoid the complexities of dealing with iodine (e.g. constructing a proper pseudopotential and worrying about rela-

Figure 2.8: TPD simulation process: the sample gas was dosed on to the single-crystal metal surface at low temperature. Subsequent heating of the catalyst surface at a constant rate β stimulates surface reactions and produces gas desorption. The peak height indicates the gas desorption rate, and the integral of the peak area corresponds to the amount of gas desorbed.

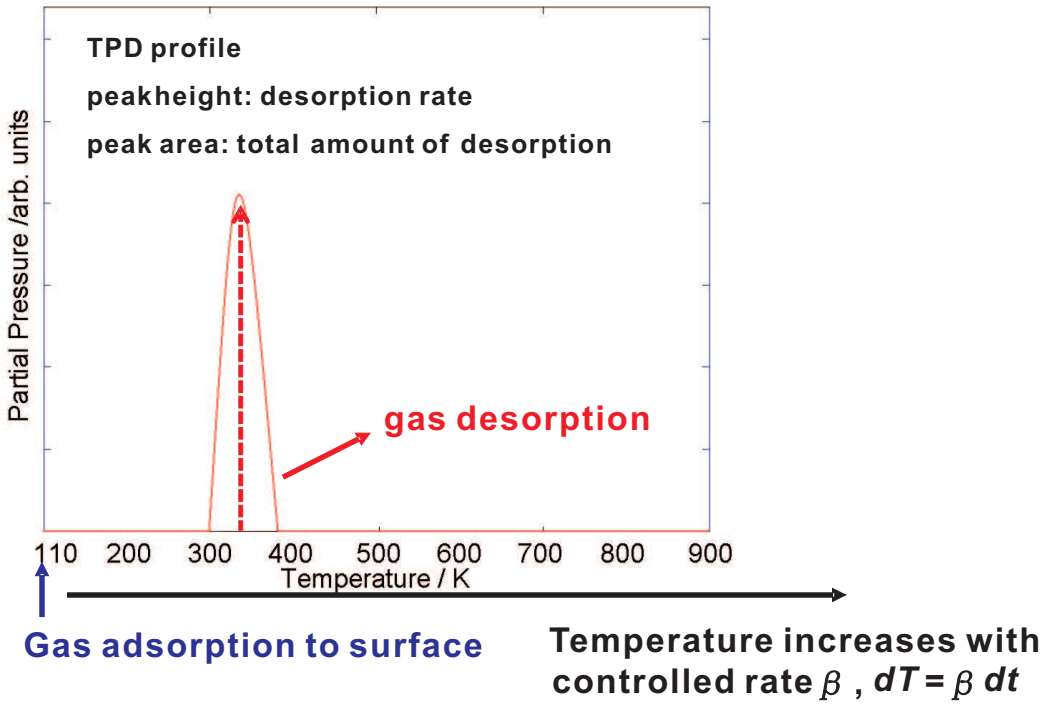

tivistic effects), the surface was simply seeded with $*CH_2$, and all iodine chemistry was neglected.

Second, it is virtually impossible experimentally to clean metallic vanadium surface completely. As several groups have noted, residual oxygen remains on the surface despite repeated cycles of sputtering and annealing.[104–107] Fortunately, the oxygen coverage was estimated at 0.1 ML or less in the experiments examined here,[107] and no oxygenated products were identified experimentally.

Although the oxygen and iodine surface chemistry was not treated explicitly, the possibility that these species occupy some surface sites was considered through simple "low-" and "high-coverage" models that vary the amount of vacant surface sites available. These models neglect all surface-coverage dependence of the adsorption and reaction energies.

Also the following choices and assumptions were made regarding the TPD conditions and the behavior of the reaction mechanism:

1. **Reaction reversibility:** The experiments were performed under ultrahigh vacuum, so the methane and H_2 gases produced are assumed to be pumped away quickly. Therefore, product desorption is assumed to occur irreversibly in our model, when all other surface reactions are modeled as reversible.

2. **Initial $*CD_2$ concentration:** Based on the iodine 3d XPS spectra[77] for varying amounts of methylene diiodide adsorbed on a clean V(100) surface at 110K, multilayer CH_2I_2 condensation occurs once exposures exceed 3.0 L. Because of its large size, saturation of diiodomethane is estimated to occur when $\sim$20% of the surface sites are occupied. After C-I bond breaking is

triggered, at above 200 K, iodine atoms are assumed to occupy surface sites, so full surface blocking is expected. There are no vacant surface sites under these conditions. Based on that information, it is estimated that in our experiments, the 1.0 or 1.5 L CD_2I_2(g) exposures used probably correspond to fractional coverages in the vicinity of ∼0.1 ML $*CD_2$.

3. **Residual hydrogen:** We assume that the free surface hydrogen comes from ∼0.10 ML of residual water in the ultrahigh vacuum chamber (from adsorption of $\sim 3 \times 10^{-10}$ torr of background water for ∼5 min) via rapid stepwise dehydrogenation ($E_{act} \sim$ 5 and 31 kJ/mol) to remove the first and second hydrogens, respectively.

4. **Iodine chemistry:** As mentioned above, the iodine atoms originating from CD_2I_2 dissociation were not explicitly included in the model. Instead, their effect of occupying surface sites was explored here by looking at the changes in surface chemistry as a function of the fraction of vacant sites available, that is, in "low-" or "high-coverage" regimes. In the low-coverage regime, iodine does not occupy any vacant sites, and the initial concentration of vacant sites is given by $\theta_{vac} = 1 - \theta_{CH_2} - \theta_{H_2O}$. In the high-coverage regime, most of the surface sites are assumed to be occupied and "inert" by reducing the initial fraction of available vacant sites. A limiting value of 0.01 ML vacant sites was used for the high-coverage model, but the qualitative features of the results were found to be relatively independent of this specific high coverage fraction as long the number of vacant sites is small compared to the amount

of $^*CD_2$. Note that co-adsorbate interactions are not treated in our model either.

5. **Heating rate:** The TPD simulations were started at 100 K, and the temperature was ramped at a heating rate of 1 K per 100 seconds, which is 10^3 times slower than the rate used experimentally. Predicting quantitative rate constants is difficult, especially at low to moderate temperatures. Therefore, it is unsurprising that the overall predicted rates are too slow, and a slower heating rate was required to observe the appropriate chemistry.

2.4.3 Real-time flux analysis

The TPD profile simulation is focused on reaction rate of gas desorptions, solved by the microkinetic model. But the microkinetic model provides other detailed data records, e.g. reaction rate constants and species coverages as a function of time. In this way, real-time flux analysis could be carried out to reveal the most important features of the kinetics.

For each reaction, the flux can be tracked as a function of time, according to:

$$reaction\ flux_{j,t} = k_{for,j,t} \prod_{l=1}^{S_{\mathrm{R}}} \theta_{l,t}^{-\nu_{j,l}} - k_{rev,j,t} \prod_{l=1}^{S_{\mathrm{P}}} \theta_{l,t}^{\nu_{j,l}} \tag{2.20}$$

where $k_{for,j,t}$ and $k_{rev,j,t}$ are the rate constants for the forward and reverse reaction j at the specified time, θ_t represents the surface coverage of species at the specified time. All the parameters on the right side could be collected from our TPD simulation data records.

The appearance and disappearance of each gaseous and surface species at a

particular time, which is composed of all the reaction fluxes involved, could be summarized as:

$$species\ flux_{i,t} = \frac{\mathrm{d}\theta_{i,t}}{\mathrm{d}t} = \sum_{j=1}^{\text{no.rxns}} \nu_{j,i}[k_{for,j,t}\prod_{l=1}^{S_\mathrm{R}}\theta_{l,t}^{-\nu_{j,l}} - k_{rev,j,t}\prod_{l=1}^{S_\mathrm{P}}\theta_{l,t}^{\nu_{j,l}}] \qquad (2.21)$$

From here, sorting these involved reaction fluxes, we could find out active pathway(s) related to the particular species. In this way, coupled with flux analysis on each reaction and each species involved, the microkinetic model provides insight into the favored pathway(s) for $C_1 \sim C_3$ gas formation on vanadium surface.

2.5 Experimental data acquisition and analysis

Temperature-programmed desorption data were acquired by using a V(100) single crystal and a standard ultrahigh vacuum (UHV) apparatus equipped with mass spectrometry detection. The experimental details have been provided before.[77,102] New, previously unpublished TPD information on the thermal chemistry of CD_2I_2 on V(100) at two different coverages was analyzed using an established deconvolution procedure[108] and well-known methane cracking ratios[109] to eliminate any overlaps arising from multiple species with the same mass contributing to a given TPD peak.

2.6 Limitations and errors in the theoretical modeling

The DFT calculations used to parameterize the microkinetic model do have significant limitations that will likely affect the agreement between simulations with experiments. Errors arise from both the approximate density functionals used and the simplicity of the surface model. Benchmark studies on the chemisorption energies of atoms and molecules on transition-metal surfaces,[93,110] e.g. oxygen, CO and NO on Ni(100), Ni(111), Rh(100), Pd(111) surfaces, suggest that typical DFT adsorption energy errors relative to experiments are ∼150 kJ/mol with the LDA functional,[111] ∼50 kJ/mol with the PW91[91,92] or PBE functionals,[112] and ∼25 kJ/mol with RPBE[93] and revPBE functionals.[113] DFT methods tend to underestimate barrier heights for chemical reactions unless the hybrid functionals are used.[114–117] But it can also be argued that DFT could overestimate the reaction barriers in several cases, e.g. the oxidative addition of CH_4 to Pd,[118] and the cleavage of O-O and C-O bond on transition-metal-containing enzymes.[119] It is also well-known that DFT calculations using the GGA for the exchange-correlation effects overestimate the barrier for C-H bond scission in many systems.[120] For example, the DFT-GGA barrier for the methane decomposition on Ni(111) is calculated to be 108 kJ/mol,[121] whereas the experimental values of 65 kJ/mol on Ni(100) and 75 kJ/mol on Ni(111) are obtained in molecular beam experiments.[122] For the C-H bond breaking of ethylene to vinyl on Pd(111), the barrier of 151 kJ/mol by DFT-GGA(PW91) calculation[123] is also much higher than the values

of 65-75 kJ/mol as the experimental results.[124]

Such errors can have a large effect on the calculated rate constants. For instance, a typical error of 25 kJ/mol in the activation barrier leads to a rate constant that is off by a factor of ∼400 at 500 K. The effect of such errors is even larger at lower temperatures, as shown in Table 2.5. At 200K, for instance, a 25 kJ/mol error in the activation barrier alters the rate by 7 orders of magnitude. It is unsurprising that the overall predicted rates are too slow with the DFT activation barrier overestimation, and this increases the timescale of reaction significantly. However, relatively reaction rates are widely believed to be much more reliable than absolute ones. This means that one can use DFT modeling to identify which reaction pathways are kinetically important. In this way, relative reaction rates are expected to be better than absolute rate.

Table 2.5: Impact factor of potential DFT barrier errors on the rate constants at different temperatures. The errors are particularly significant at lower temperatures (e.g. 200-300K).

Temperature	Impact factor of DFT overestimation of barrier heights on rate constant				
	+0 kJ/mol	+5 kJ/mol	+15 kJ/mol	+25 kJ/mol	+35 kJ/mol
200 K	1.00	0.0494	1.209×10^{-4}	2.954×10^{-7}	7.221×10^{-10}
300 K	1.00	0.1347	0.0024	4.435×10^{-5}	8.049×10^{-7}
500 K	1.00	0.3004	0.0271	0.0024	2.205×10^{-4}
800 K	1.00	0.4715	0.1048	0.0233	0.0052
1000 K	1.00	0.5480	0.1646	0.0494	0.0148

Beyond the DFT errors, one should also consider the errors in the model surface used. Even though the ultrahigh vacuum Zaera experiments[77] use single-crystal V(100) surfaces instead of the much more complicated real-world catalyst particles,[24–26] the simple 2×2 unit cell model used here cannot capture many of the complexities of the real surface. The experimental surface will exhibit defects and

edges sites, it will likely have residual species adsorbed on the surface even after repeated cycles of sputtering and annealing, and it may even undergo surface reconstructions.

Under-coordinated defect and edge sites are catalytically important in many reactions. For example, step sites play an important role in ethane reforming on nickel surfaces,[125] the active B_5 sites are believed to be involved in the rate-determining N_2 dissociation step for ammonia synthesis on ruthenium catalyst particles,[33,34] and carbon monoxide cleavage is favored on cobalt step sites.[48,68]

The models used here also typically ignore the co-adsorption effects that occur among FT species or between FT species and surface impurities. In some cases, high concentrations of surface species can lead to surface reconstructions. For example, if enough oxygen is present, the strong vanadium-oxygen bonding can lead to a (1×5) reconstruction on V(100)[104–106] or even the formation of a thin V_2O_3 + VO_2 mixed surface oxide film.[107] Other impurities such as residual hydrogen or carbon could also complicate the story. The experimentalists believe they cleaned the surfaces adequately and that the V(100) surfaces has not undergone such reconstructions, but complete characterization of the experimental surfaces is difficult.

Finally, the microkinetic models used here assume that the adsorbates diffuse readily enough to allow mixing of the reactants on the surface. In reality, of course, a crowded surface may hinder adsorbate diffusion, and some species may not diffuse readily at the temperatures used in the experiments.[126] This would mean that the surface would exhibit heterogeneous surface coverage of different

species, and that the local adsorbate environment might play an important role in determining the chemistry of individual surface adsorbates. In principle, one could construct a kinetic Monte Carlo model and try to incorporate the effects of the local reaction environments, but the sheer number of species involved in the chemistry here makes such an approach dauntingly complex.

Overall, despite the inherent DFT errors and modeling limitations, DFT and microkinetic modeling have proved useful in understanding heterogeneous catalysis processes,[33,34,38–53] and they provide interesting new insights to the FT chemistry explored in the following chapters.

Chapter 3

Methane-formation on V(100)

3.1 Introduction

In FT technology, the first step is the steam reforming of natural gas, coal or biomass to form syngas (mixture of CO and H_2), and then FT synthesis converts the syngas into a wide range of hydrocarbon products (paraffins and olefins) from C_1 up to C_{100}, and a small amount of oxygenates. With the hydrocarbon-chain growth and product upgrading processes, FT synthesis could yield high quality fuels (especially diesel) and specialty chemicals. However, the simplest product does not require hydrocarbon-chain growth. Rather, stepwise hydrogenation of C produces methane (Figure 3.1). In this way, methane formation is a relatively easy process. In fact, on vanadium catalysts, methane is the dominant carbon product. This makes methane formation an excellent starting point for investigating FT synthesis on V(100). In this chapter, we use DFT to predict the thermochemistry of adsorbed single-carbon ($*C_1$) species and their hydrogenation reaction kinetics

on V(100) and then assess this model by comparing its predictions against those from kinetics experiments.

Figure 3.1: Stepwise hydrogenation from *C to CH_4(g)

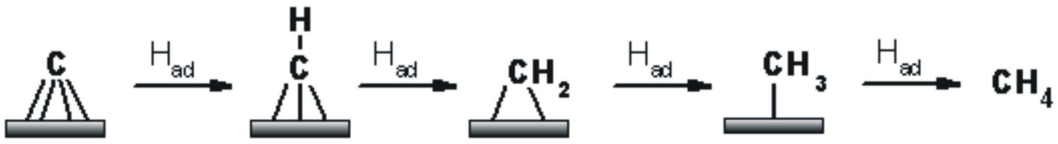

At first glance, the DFT model described below appears to disagree with the previously proposed mechanism: whereas the earlier experimental work suggested that methylene dehydrogenation is rate-limiting, the DFT energetics indicate that methylene dehydrogenation has a very low activation barrier and should occur readily. Careful microkinetic simulation of the isotopic-substitution methane formation seen in TPD experiments with isotope-substituted methylene precursors, however, reveals that the DFT mechanism does qualitatively reproduce the correct distribution of methane isotopomers. Further support for the microkinetic model comes from the fact that it predicted the production of a particular methane isotopomer (CH_3D) which was not identified in the earlier experiments, but which was detected in new experimental data reported here. The microkinetic modeling also revealed that the C_1 chemistry on V(100) exhibits two distinct regimes, depending on the availability of vacant surface sites.

The next section describes the computational modeling and experimental approaches. Afterwards, the energetics and kinetics of methane formation on V(100) are examined, a set of TPD experiments with isotope-substituted intermediates is

simulated using the microkinetic model, and the results are compared to the experimental data. Finally, the mechanistic details observed from the simulations and their potential implications for Fischer-Tropsch synthesis on V(100) are discussed.

3.2 Computational details

For methane-formation, we use a 2×2 unit cell (corresponding to 0.25 ML coverage of adsorbates) with a four-layer slab of V(100) surface. The most stable binding sites for each species and transition states for each elementary reaction steps have been obtained along the methane formation pathways using the techniques described in Chapter 2. A microkinetic model was built from the DFT thermochemistry data to simulate isotopic-substituted experimental TPD spectra,[77] which provides insights into the important intermediates and reaction pathways. Further computational details are provided in Chapter 2, Appendix A, and Appendix B.

3.3 Results and Discussion

3.3.1 Calculated C_1 species thermochemistry and reactivity on V(100)

The preferred V(100) binding sites and the corresponding adsorption energies calculated for the various species studied here are presented in Table 3.1. The calculated electronic and free energy profiles of C_1 hydrogenation on V(100) are

Table 3.1: Calculated DFT electronic binding energies, ΔE_{ads}, for adsorbates in their most stable binding sites on V(100) with 0.25 ML coverage. Note that gaseous CH_4 adsorbs dissociatively to surface $*CH_3$ and *H.

species	ΔE_{ads} (kJ/mol)	binding site
H	-279.5	two-fold
H_2	-9.6	on-top
C	-850.0	four-fold
CH	-730.4	four-fold
CH_2	-552.9	four-fold
CH_3	-193.9	two-fold
CH_4	no binding	

illustrated in Figure 3.2. The calculated energies are plotted relative to the energy of surface methylene, the starting species in the TPD experiments.

The DFT calculations indicate that surface species *H, *C, *CH, $*CH_2$ bind preferentially at four-fold sites, while $*CH_3$ prefers two-fold sites over the four-fold ones by 18 kJ/mol. Interestingly, the hydrogenation of $*CH_2$ to form $*CH_3$ is faster at a four-fold site ($E_{act} \sim 140$ kJ/mol) than at a two-fold site ($E_{act} \sim 170$ kJ/mol). The resulting $*CH_3$ can then diffuse readily to the preferred two-fold site ($E_{act} \sim 15$ kJ/mol).

The electronic and free energies profiles are similar. At low temperatures, the C_1 species stability decreases with increasing hydrogenation, as one might expect on an early transition metal surface. Above ∼500 K, however the relative free energies of *C and *CH reverse, and *CH becomes the most stable C_1 species on the V(100) surface. Also, as expected, the higher entropy of gaseous methane stabilizes it at higher temperatures.

Comparison of the relative C_1 species stabilities and reaction barriers reveals that methylene dehydrogenation ought to occur much more readily ($E_{act} \sim 25$

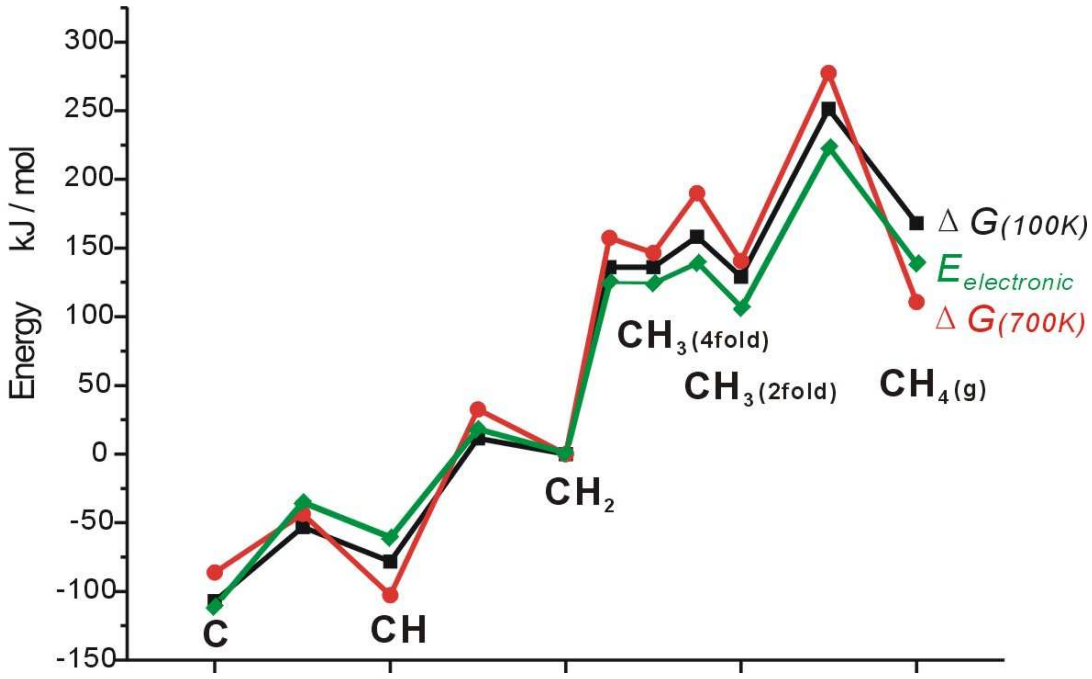

Figure 3.2: The energetics of C_1 hydrogenation to CH_4(g) on V(100). The electronic energies (green), free energies at 100 K (black), and free energies at 700 K (red) are all shown. The relative stability in terms of free energies between *C and *CH reverse around 500 K. All energies are plotted relative to that of adsorbed *CH_2 + 2 *H.

kJ/mol) than methylene hydrogenation ($E_{act} \sim 140$ kJ/mol). This would suggest that surface methylene should decompose rapidly to methylidyne or carbide. Previous DFT predictions on traditional Fischer-Tropsch catalysts found similar qualitative trends for methylene hydrogenation versus dehydrogenation.[78]

These predictions seemingly contradict the isotopic substitution TPD experiments which suggested that methylene dehydrogenation occurs slowly and is perhaps even rate-limiting in methane and/or vinyl production.[77] To make it feasible to simulate the TPD experiments and determine if the DFT model is consistent with the experimental data (Section 3.3.2), the reaction thermochemistry and the rate constants for the incorporation of either an H or D to each CH_xD_y surface species were computed next.

Table 3.2 provides a complete list of the DFT-predicted thermochemistry for all reactions included in the microkinetic model described in Section 3.3.2. This includes all possible C_1 hydrogenation and/or deuteration reactions, the surface formation and desorption of H_2/HD/D_2, and the dissociation of water on the surface. To examine the kinetic isotope effects, Table 3.3 summarizes the free energies of reaction (ΔG°_{rxn}) and activation (ΔG°_{act}) for the different isotopomers computed from the data in Table 3.2. A reaction that adds deuterium instead of hydrogen is typically 3-4 kJ/mol less endoergic and exhibits a ∼1 kJ/mol higher activation barrier. Overall, the predicted hydrogenation reaction rate constants are up to twice as fast as the analogous deuteration ones, while the dehydrogenation reactions are ∼2–6 times faster than the de-deuteration ones. In other words, for

Table 3.2: Thermochemistry for all elementary steps included in the microkinetic model. All thermodynamic functions were evaluated at 300 K and 1 bar.

Elementary step	ΔH_{rxn}(0 K) (kJ/mol)	ΔH°_{rxn} (kJ/mol)	ΔS°_{rxn} (J/mol·K)	ΔH_{act}(0 K) (kJ/mol)	ΔH°_{act} (kJ/mol)	ΔS°_{act} (J/mol·K)
*C + *H ⟶ *CH + *	25.8	36.8	78.5	51.2	56.0	21.1
*C + *D ⟶ *CD + *	25.2	36.1	80.5	51.8	56.4	19.0
*CH + *H ⟶ *CH_2 + *	78.1	74.1	-39.2	89.0	82.1	-74.1
*CH + *D ⟶ *CHD + *	76.3	72.3	-39.3	89.7	82.7	-75.9
*CD + *H ⟶ *CHD + *	76.9	73.0	-41.3	88.1	81.4	-75.4
*CD + *D ⟶ *CD_2 + *	75.1	71.1	-41.7	88.8	81.8	-77.1
*CH_2 + *H ⟶ *CH_3 + *	127.7	127.8	-16.2	180.8	178.2	-45.0
*CH_2 + *D ⟶ *CH_2D + *	125.2	125.1	-16.2	181.7	178.9	-46.1
*CHD + *H ⟶ *CH_2D + *	127.0	126.9	-16.0	180.3	177.6	-44.8
*CHD + *D ⟶ *CHD_2 + *	124.4	124.1	-16.2	181.2	178.3	-45.9
*CD_2 + *H ⟶ *CHD_2 + *	126.2	125.9	-15.8	179.7	177.0	-44.6
*CD_2 + *D ⟶ *CD_3 + *	123.5	123.0	-16.2	180.6	177.6	-45.7
*CH_2 + *H ⟶ *CH_3(4-fold) + *	135.3	134.9	-14.8	131.2	128.1	-40.0
*CH_2 + *D ⟶ *CH_2D(4-fold) + *	133.4	132.9	-15.3	131.1	127.9	-41.2
*CHD + *H ⟶ *CH_2D(4-fold) + *	135.3	134.7	-15.1	131.2	128.0	-40.2
*CHD + *D ⟶ *CHD_2(4-fold) + *	133.3	132.7	-15.8	131.1	127.7	-41.5
*CD_2 + *H ⟶ *CHD_2(4-fold) + *	135.2	134.5	-15.4	131.2	127.7	-40.5
*CD_2 + *D ⟶ *CD_3(4-fold) + *	133.2	132.3	-16.2	131.1	127.4	-41.8
*CH_3(4-fold) ⟶ *CH_3	-7.6	-7.1	-1.4	21.8	18.7	-35.1
*CH_2D(4-fold) ⟶ *CH_2D	-8.3	-7.8	-0.9	21.3	18.2	-35.2
*CHD_2(4-fold) ⟶ *CHD_2	-9.0	-8.6	-0.5	20.8	17.7	-35.3
*CD_3(4-fold) ⟶ *CD_3	-9.7	-9.3	0.0	20.3	17.3	-35.3
*CH_3 + *H ⟶ CH_4(g) + 2*	50.5	50.5	116.8	122.3	120.1	-22.1
*CH_3 + *D ⟶ CH_3D(g) + 2*	47.8	47.2	116.7	123.3	120.8	-23.3
*CH_2D + *H ⟶ CH_3D(g) + 2*	50.3	50.0	116.7	122.0	119.7	-22.4
*CH_2D + *D ⟶ CH_2D_2(g) + 2*	47.5	46.5	116.5	123.0	120.5	-23.7
*CHD_2 + *H ⟶ CH_2D_2(g) + 2*	50.1	49.3	116.7	121.8	119.5	-22.7
*CHD_2 + *D ⟶ CHD_3(g) + 2*	47.1	45.8	116.3	122.8	120.3	-24.0
*CD_3 + *H ⟶ CHD_3(g) + 2*	49.8	48.8	116.7	121.5	119.2	-23.0
*CD_3 + *D ⟶ CD_4(g) + 2*	46.7	45.2	116.0	122.6	120.0	-24.3
*H + *H ⟶ H_2(g) + 2*	113.7	118.9	93.9	109.2	111.4	9.3
*H + *D ⟶ HD(g) + 2*	114.9	119.5	97.7	109.4	111.5	10.1
*D + *D ⟶ D_2(g) + 2*	115.4	119.4	101.1	109.0	111.1	10.6
H_2O* + * ⟶ *OH + *H	-175.0	-177.1	-7.8	4.8	0.5	-37.1
*OH + * ⟶ *O + *H	-172.7	-172.9	4.2	31.2	28.4	-21.4

Table 3.3: Thermochemistry comparison of *CH_xD_y + *H hydrogenation versus *CH_xD_y + *D deuteration reactions for each C_1 surface species at 300 K and 1 bar, in kJ/mol. The ΔG values for the hydrogenation reactions are given directly, while the free energies for the deuteration reactions are listed as shifts relative to the hydrogenation values. The final column lists the ratio of the rate constants for hydrogenation (forward) and dehydrogenation (reverse) steps.

Initial *CH_xD_y surface species	Hydrogenation		Deuteration Shift		Ratio	
	ΔG_{rxn}	ΔG_{act}	$\delta(\Delta G_{rxn})$	$\delta(\Delta G_{act})$	k^H/k^D	k^H_{rev}/k^D_{rev}
*C	13.2	49.7	-1.3	0.9	1.4	2.4
*CH	85.8	104.2	-1.8	1.2	1.6	3.3
*CD	85.4	103.9	-1.8	1.1	1.6	3.2
*CH_2(2-fold)	132.7	191.6	-2.8	0.9	1.4	4.4
*CHD(2-fold)	131.7	191.0	-2.8	1.0	1.5	4.6
*CD_2(2-fold)	130.7	190.3	-2.8	1.0	1.5	4.6
*CH_2(4-fold)	139.3	140.1	-1.9	0.2	1.1	2.3
*CHD(4-fold)	139.2	140.0	-1.9	0.1	1.0	2.2
*CD_2(4-fold)	139.1	139.9	-1.9	0.1	1.0	2.2
*CH_3	-15.4	126.6	-2.7	1.2	1.6	4.8
*CH_2D	-14.9	126.5	-3.4	1.1	1.6	6.1
*CHD_2	-14.2	126.2	-3.4	1.2	1.6	6.3
*CD_3	-13.6	125.9	-3.3	1.3	1.7	6.3

steps in quasi-equilibrium, the deuteration reactions will generally exhibit higher net conversion rate than hydrogenation ones, while for slow steps or irreversible steps (the final methane associative desorption, for instance), hydrogenation occurs slightly faster than deuteration.

3.3.2 Microkinetic model for methane production

As mentioned in the Introduction, the thermochemistry calculated by DFT seemingly disagrees with the TPD data from earlier experimental work. The DFT activation barriers suggest that methylene dehydrogenation should be fast, not rate-limiting as was inferred from the experiments. To address this apparent discrepancy, the TPD experiments were simulated using the *ab initio* microkinetic model in Table 3.2.

3.3.2.1 Summary of the TPD data to be simulated

Before describing the microkinetic TPD simulations in detail, the TPD experimental data the simulations aim to reproduce are summarized.[77] A clean V(100) surface was dosed with various amounts (e.g. 1.0 or 1.5 L) of CD_2I_2 at 110 K and the temperature ramped at a rate of 10 K per second until reaching 1200 K. A variety of gaseous products, including all possible isotopomers of hydrogen, methane, and ethylene, were detected and followed via mass spectrometry; here we focus on the evolution of the methane isotopomers. The source of the hydrogen in these experiments is unknown, but it is likely to be the trace water present the ultrahigh vacuum chamber, or perhaps subsurface hydrogen in the vanadium

crystal.

It was observed that a mixture of methane isotopomers start desorbing around 200 K; those desorption rates peak near 300 K (Figure 3.3). The main product was identified as CH_2D_2 (18 amu), with additional smaller amounts of CD_4 (20 amu) and CHD_3 (19 amu). Due to significant overlap with fragments from CH_2D_2 ionization in the mass spectrometer, the production of CH_3D (17 amu) is more difficult to isolate; the signal attributed to this species was small and within the experimental error of the data deconvolution. Small amounts of CH_4 (16 amu) were possibly detected at the upper end of the methane production temperature range.

The experimental observation of a minimal formation of methane isotopomers containing fewer than two deuterium atoms supports the idea that CD_2 dissociation is slow and perhaps even rate-limiting. Also, the production of hydrogen-containing methane isotopomers peaks at slightly higher temperatures than the CD_4 desorption, suggesting that the generation of reactive hydrogen on the surface is thermally activated. The increased production of hydrogen-containing isotopomers around 250–300 K is also consistent with possibility that the extra hydrogen is produced from decomposition of water on V(100). TPD experiments with dosed water exhibit a peak around 260–270 K.[127]

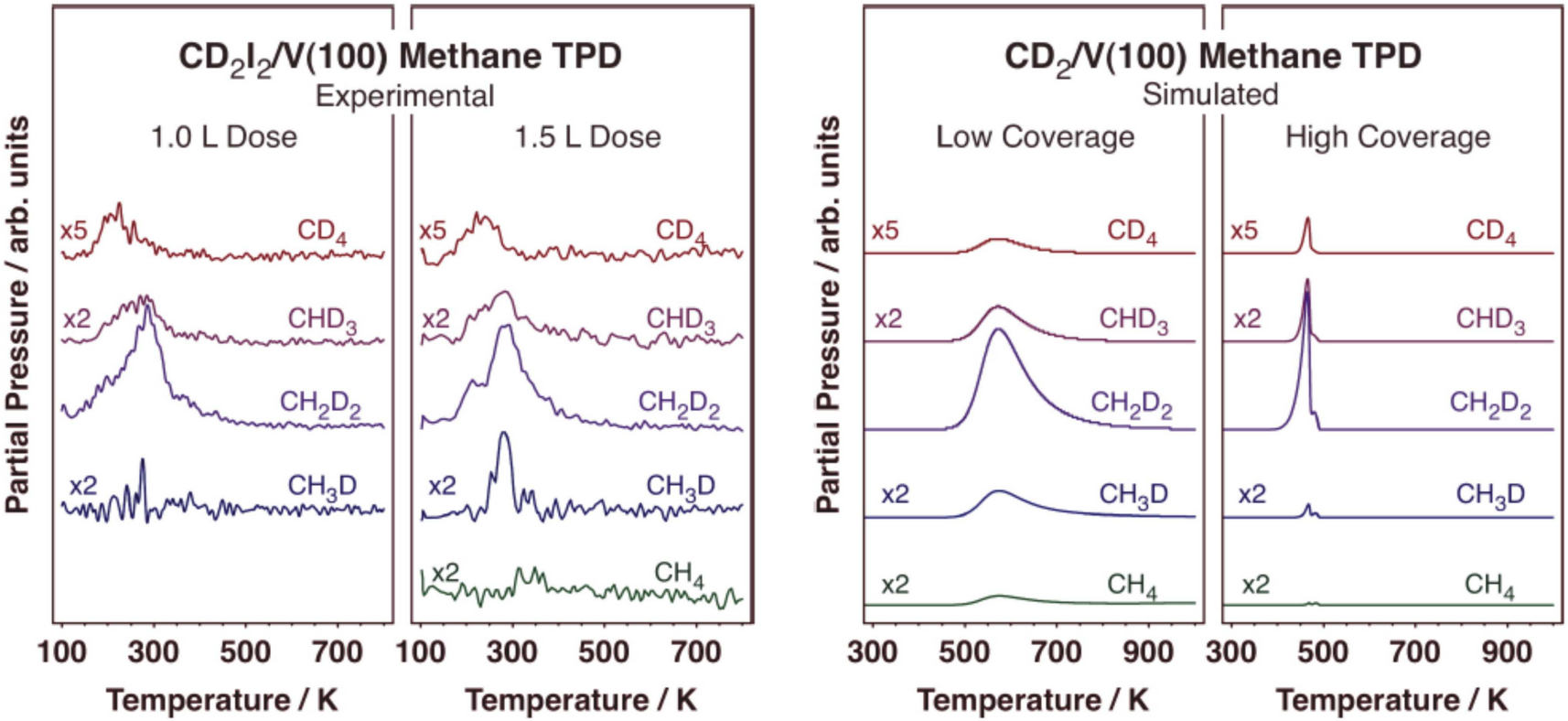

Figure 3.3: Experimental (two left frames) and simulated (two right frames) TPD spectra for methane isotopomer formation on V(100) under different conditions. The peak temperatures in the simulations are shifted to higher temperatures than those seen in the experiments, but the relative peak intensities from the simulations agree reasonably well with those from the experiments.

Table 3.4: TPD microkinetic model conditions used to initialize the V(100) surface for methane formation.

Initial fractional surface coverages θ_i:	
$^*CD_2$	0.10 ML
H_2O^*	0.10 ML
Vacant sites: either	0.80 ML (low coverage) or
	0.01 ML (high coverage)
Temperature program:	
Initial temperature	100 K
Heating rate	1 K per 100 seconds
Final temperature	1000 K

3.3.2.2 TPD simulation results

When simulating the experimental results discussed above, choices and assumptions as described in Section 2.4.2 were made regarding the TPD conditions and the behavior of the reaction mechanism. Table 3.4 summarizes the key initial conditions for the TPD simulations.

Figure 3.3 shows simulated TPD profiles for production of the methane isotopomers under the low- or high-coverage regimes defined by the conditions specified in Table 3.4, which were chosen to resemble the experimental conditions. It can be seen from that figure and from Table 3.5 that the relative product yields agree well with the experiments.[77] Indeed, the model predicts the relatively low yields of CD_4 and CHD_3, the large production of CH_2D_2, and the small amounts of CH_3D and CH_4 (see Table 3.5) seen in the TPD traces.

On the other hand, it should be noted that the simulated peak positions occur at much too high temperatures, near 500 K instead of around 300 K in the experiments. In other words, the DFT microkinetic model overestimates the activation

Table 3.5: Calculated and experimentally measured methane isotopomer distribution from TPD with different initial CD_2I_2(g) doses.

Initial CD_2I_2(g) dose	CH_4(g)	CH_3D(g)	CH_2D_2(g)	CHD_3(g)	CD_4(g)
		Simulations			
0.10 ML (low-coverage regime)	2%	8%	78%	12%	1%
0.15 ML (low-coverage regime)	0.3%	3%	63%	25%	8%
0.10 ML (high-coverage regime)	0.6%	4%	88%	6%	1%
0.15 ML (high-coverage regime)	0.2%	3%	76%	15%	6%
		Experiments			
1.0 L	1%	3%	78%	15%	3%
1.5 L	3%	7%	72%	15%	3%

barriers and underestimates the reaction rates seen in the recorded TPD data. According to the Redhead model,[128] an experimental peak at 315 K suggests a ∼70 kJ/mol activation energy for second-order methane associative desorption. The computed DFT barrier is ∼120 kJ/mol instead. Such overestimation of the hydrogenation barriers slows the overall reaction kinetics considerably. The neglect of co-adsorbate interactions on a crowded surface may be one factor affecting the predicted reaction barriers. Heterogeneities in the distribution of species on the surface and limited mobility of the adsorbed species may also contribute to this discrepancy.[126] And edges and defects on vanadium surface may stimulate surface reactions for the earlier gas desorption. More discussion on the peak position is in Section 3.4.

Of course, choosing initial model conditions that mimic the experiments is challenging and requires a number of assumptions. Fortunately, the qualitative product distribution predicted by the model is fairly insensitive to the choice of initial conditions. For instance, Figure 3.4 shows that the microkinetic model reproduces the experimental observation that CH_2D_2 is the most abundant methane

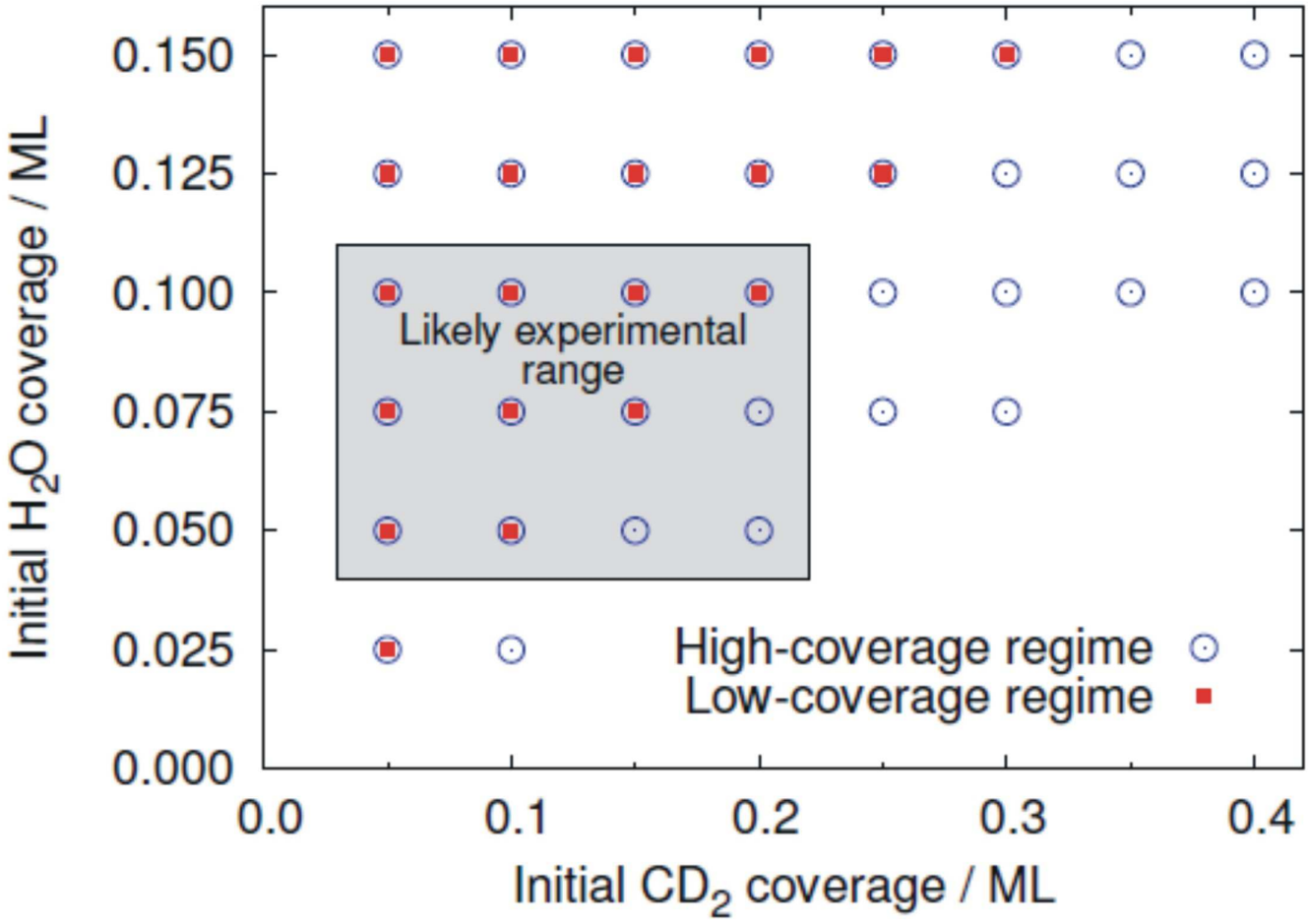

Figure 3.4: As indicated by the circles (high-coverage conditions) and squares (low-coverage conditions), CH_2D_2(g) is the major methane isotopomer produced across a wide range of initial surface conditions. The shaded region indicates the most likely experimental conditions.

isotopomer for a fairly broad range of initial conditions. Within the range of initial conditions that we believe are most likely to correspond to the experimental conditions, CH_2D_2 is always the major isotopomer produced for the high-coverage model and is usually the major isotopomer for the low-coverage model as well. Also, as one might expect, increasing the ratio of initial $*CD_2$ to H_2O* modestly increases the proportion of more heavily deuterated products (CD_4 and CHD_3) at the expense of the other, less-deuterated isotopomers. Overall, these results suggest that meaningful conclusions can be drawn from the model despite the uncertainties surrounding the exact experimental surface coverages and the estimated rate constants.

The methane isotopomer distributions shown in Figure 3.3 are similar in both the low- and high-coverage regimes, but the operative reaction mechanism differs between the two cases, as can be seen from the surface coverage profiles plotted in Figure 3.5. In the low-coverage regime, the abundance of vacant surface sites allows rapid dehydrogenation of $*CD_2$ to *C. As the surface sites are occupied and the temperature rises, however, stepwise hydrogenation and deuteration begin to occur, and methylene hydrogenation becomes the rate-limiting step. The isotopic preference for CD_2H_2 production arises from a combination of the relative proportions of hydrogen and deuterium on the surface and a modest kinetic isotope preference for hydrogenation (Table 3.3). In the 0.1 ML $*CD_2$ + 0.1 ML H_2O* case, for instance, neglecting the kinetic isotope effect reduces the proportion of CH_2D_2 from 77% to 38%.

In the high-coverage regime, on the other hand, the few available vacant surface

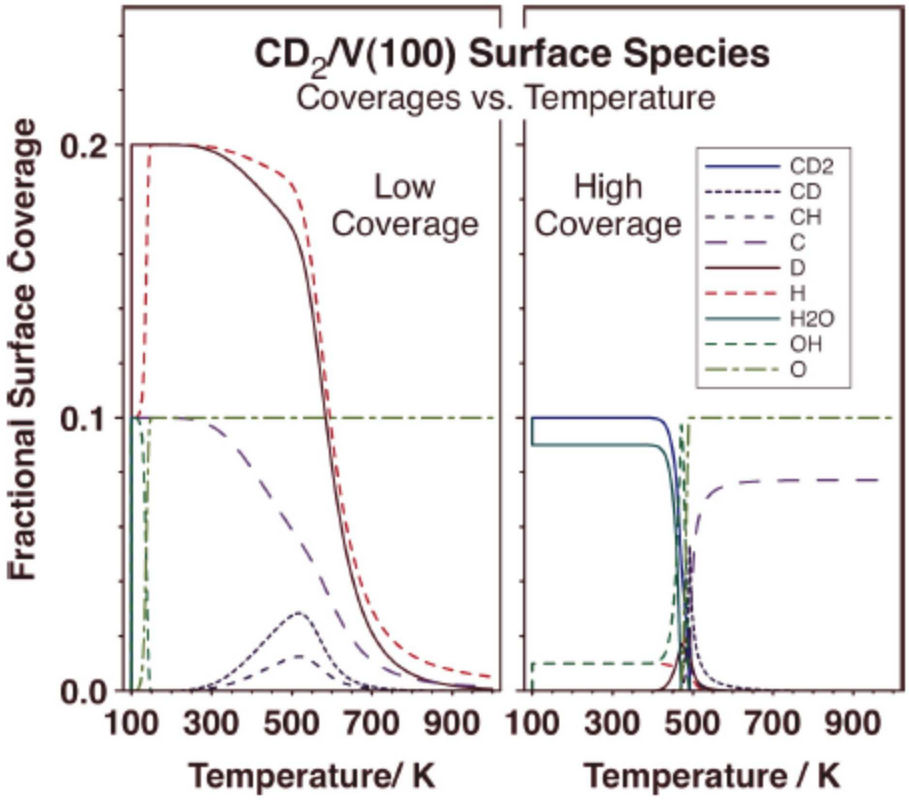

Figure 3.5: Evolution of the surface coverages of all relevant adsorbates as a function of time estimated from our microkinetic modeling of the TPD experiments with $*CD_2$ on V(100). In the low-coverage regime (left), $*CD_2$ de-deuteration occurs rapidly. In the high-coverage regime (right), $*CD_2$ de-deuteration is hindered by the lack of surface sites, and methylene hydrogenation occurs more readily.

sites are quickly occupied by hydrogen from facile water dissociation, which has an even lower barrier than that for methylene dehydrogenation according to DFT. Therefore, the absence of vacant sites means that $*CD_2$ dehydrogenation occurs slowly. Initially, hydrogen adatoms out-number deuterium ones, so hydrogenation of $*CD_2$ to CH_2D_2(g) dominates. As the hydrogen is depleted, however, more CD_2 dehydrogenation occurs, leading to the formation of other methane isotopomers in smaller quantities.

3.3.3 Mechanistic implications for Fischer-Tropsch synthesis on V(100)

The TPD simulation results reported above indicate that methane formation can occur with two different limiting behaviors. In the high-coverage regime, methylene dissociation is slow due to the low concentration of vacant surface sites. In the low-coverage regime, however, methylene dissociation occurs rapidly. Nevertheless, both mechanisms produce similar isotopic product distributions, both consistent with the experimental results. Therefore, we suggest that the aforementioned methane isotopic substitution experiments are insufficient to determine if methylene dehydrogenation is rate limiting in Fischer-Tropsch on V(100). On the other hand, additional experimental results indicate that Fischer-Tropsch products (ethylene and propene) are favored at higher CH_2I_2(g) exposures, which may correspond to the high-coverage regime where methylene dehydrogenation is slow.[77]

At the same time, our results indicate that carbide and methylidyne surface species are much more stable than adsorbed methylene or methyl moieties (Fig-

ure 3.2). This could have significant implications for the Fischer-Tropsch mechanism because it suggests that the surface may accumulate methylidyne during the TPD experiments. In the context of traditional Fischer-Tropsch chemistry, which starts from syngas (CO(g) and H_2(g)), methylidyne could also form readily after CO dissociation. Indeed, a number of Fischer-Tropsch studies on various transition metal surfaces have indicated a thermodynamic preference for methylidyne and/or carbide intermediate formation on the surface.[35,129–132] Several groups have argued in favor of a revised version of the alkenyl mechanism in which methylidyne, not methylene, is the key building block during chain growth.[35,41,133,134] Recent DFT studies have also identified a variety of other potentially important reactions that grow hydrocarbon chains by coupling C or CH with species other than vinyl.[38,41,47,68,70,76] In the future, it will be particularly interesting to see if DFT calculations can be used to predict that similar chain-growth reactions involving *C or *CH are important in Fischer-Tropsch chemistry on V(100) or on other types of surfaces and to determine whether those predictions are consistent with the Shen and Zaera experiments.

3.4 Co-adsorption effect on methane desorption temperature

As described before, the relatively high DFT barriers slow the overall reaction kinetics considerably and shift the desorption peaks to the right compared to the experimental TPD spectras. In Shen and Zaera's TPD experiments, dif-

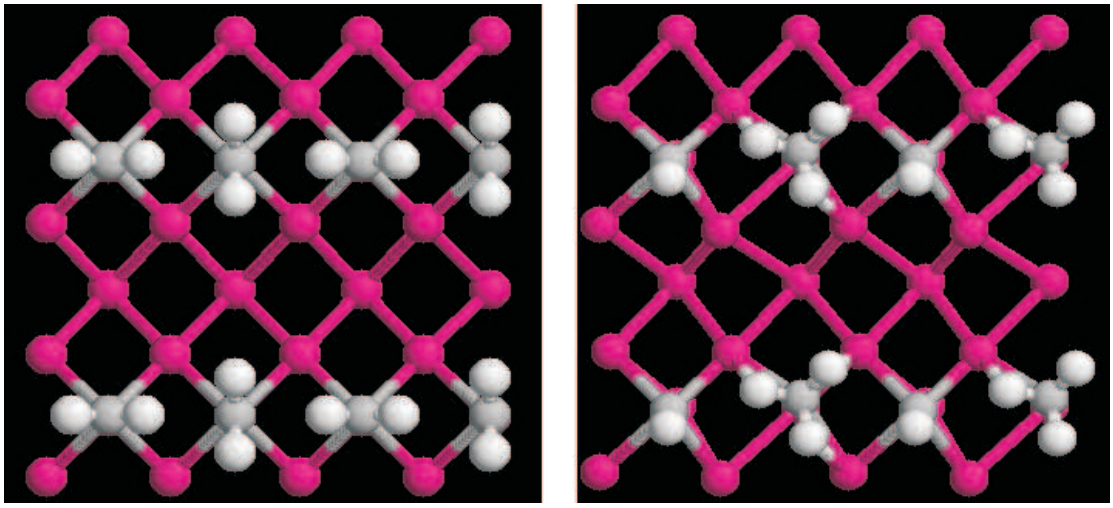

Figure 3.6: Barrier of the hydrogen transfer between two neighboring *CH_2 to the neighboring *CH and *CH_3 species is 57.7 kJ/mol, which is 70.3 kJ/mol smaller than the regular stepwise hydrogenation barrier to *CH_3.

ferent amounts of methylene diiodide are sampled on a clean V(100) surface at 110K, when its saturation coverage is estimated less than ∼20% coverage, due to its molecule size. Iodine atoms are also assumed to occupy some surface sites, above 200K with C-I bond breaking. In this way, interactions among neighboring adsorbates on the relatively crowded surfaces might effectively lower the barriers, compared to our earlier calculations.

Table 3.6: Activation energy for hydrogenation steps when *C_1 species and hydrogen co-adsorb on the surface.

Activation energy	0.25 ML (forward) (kJ/mol)	0.25 ML (backward) (kJ/mol)	0.50 ML (forward) J/mol)	0.50 ML (backward) (kJ/mol)
[C + H]* $\longrightarrow$ *CH	79.6	25.9	79.6 + 13.2	25.9
[CH + H]* $\longrightarrow$ *CH_4*	82.8	17.6	82.8 + 4.8	17.6
[CH_2 + H]* $\longrightarrow$ *CH_3(4fold)*	128.0	1.0	128.0 - 3.8	1.0
[CH_3 + H]* $\longrightarrow$ *CH_4gas	120.7	84.7	120.7 - 16	84.7

To investigate this issue, 0.5 ML coverage of adsorbates is used to describe the co-adsorption of two species binded on the 2×2 unit cell. As *H and *C_1 species

Table 3.7: Activation energy for hydrogenation and dehydrogenation steps among co-adsorbed $*C_1$ species on the surface. [A + B]* indicates the co-adsorption of both adsorbates.

Activation energy	0.25 ML (forward) (kJ/mol)	0.25 ML (backward) (kJ/mol)	0.50 ML (forward) J/mol)	0.50 ML (backward) (kJ/mol)
$*C + *H \longrightarrow *CH + *$	79.6	25.9		
$[C + CH_2]* \longrightarrow [CH + CH]*$			77.9 - 1.7	86.0
$[C + CH_3]* \longrightarrow [CH + CH_2]*$			79.6 - 37.9	127.6
$*CH + *H \longrightarrow *CH_2 + *$	82.8	17.6		
$[CH + CH]* \longrightarrow [CH_2 + C]*$			82.8 + 3.2	77.9
$[CH+ CH_3]* \longrightarrow [CH_2 + CH_2]*$			82.8 - 69.7	57.6
$*CH_2 + *H \longrightarrow *CH_3 + *$	128	1.0		
$[CH_2 + CH]* \longrightarrow [CH_3 + C]*$			128.0 - 0.4	41.7
$[CH_2 + CH_2]* \longrightarrow [CH_3 + CH]*$			128.0 - 70.3	13.1
$*CH_3 + *H \longrightarrow CH_4(gas) + 2*$	102.8	84.7		
$[CH_3 + CH]* \longrightarrow CH_4(gas)+ *C$			102.8 - 63.1	118.5
$[CH_3 + CH_2]* \longrightarrow CH_4(gas) + *CH$			102.8 - 23.1	126.3

are abundant on the surface, we investigate the co-adsorption effect between $*C_1$ and $*C_1$ species, and also between $*C_1$ and *H species. For the hydrogenation steps from carbide to methane gas product, the barrier co-adsorbing $*C_1$ and *H at 0.5 ML reduces the barrier for $*CH_2$ and $*CH_3$ hydrogenation by only $\sim$10 kJ/mol, as shown in Table 3.6. But the co-adsorption of $*C_1$ and $*C_1$ surface species decreases the hydrogenation barriers much more by allowing reactions that transfer hydrogen atoms directly between the neighboring $*C_1$ species, as shown in Table 3.7. Most notably, the barrier to form $*CH_3$ is reduced by 70.3 kJ/mol to 57.7 kJ/mol when the hydrogen is transferred from two neighboring $*CH_2$ adsorbates to *CH and $*CH_3$ species (in Figure 3.6).

Moreover, because it is experimentally difficult to remove all oxygen from the vanadium surface,[104–107] we also investigated the effect of co-adsorbed oxygen on the key reactions. Co-adsorption with oxygen lowers the hydrogenation barrier of $*CH_2$ (128.0 kJ/mol) to 73.8 (with 0.25 ML oxygen coverage) or 50.8 kJ/mol

(with 0.50 ML oxygen coverage). Also harmonic vibrational frequency calculations suggest that the co-adsorption system has less entropy, which could decrease the reaction barrier (Gibbs free energy) further. In other words, co-adsorbate interactions among $*C_1$, hydrogen, and residual oxygen adsorbates, all reduce the barriers for $*C_1$ group hydrogenation. Their neglect in the earlier model described in Section 3.3.1 and 3.3.2 may help explain the artificially elevated temperature scales of the simulated TPD spectra.

Table 3.8: Thermochemistry for hydrogenation steps with co-adsorbed $*C_1$ and *H species, also the hydrogen transfer steps with co-adsorbed $*C_1$ and $*C_1$ species. Evaluated at 300 K and 1 bar.

Elementary step	ΔH_{rxn}(0 K) (kJ/mol)	ΔH°_{rxn} (kJ/mol)	ΔS°_{rxn} (J/mol·K)	ΔH_{act}(0 K) (kJ/mol)	ΔH°_{act} (kJ/mol)	ΔS°_{act} (J/mol·K)
[C + H]* $\longrightarrow$ CH*	67.8	73.1	53.2	93.2	92.4	-4.1
[CH + H]* $\longrightarrow$ CH_2*	84.8	83.4	-127.4	95.6	91.4	-47.6
[CH_2 + H]* $\longrightarrow$ CH_3(4fold)*	133.7	136.9	36.6	129.5	130.1	11.3
[CH_3 + H]* $\longrightarrow$ CH_4gas	32.4	35.0	139.4	104.1	104.5	0.5
[C + CH_2]* $\longrightarrow$ [CH + CH]*	-16.2	-13.4	18.4	67.1	68.4	10.8
[C + CH_3]* $\longrightarrow$ [CH + CH_2]*	-98.0	-98.6	2.0	27.5	24.5	-24.4
[CH+ CH_3]* $\longrightarrow$ [CH_2 + CH_2]*	-46.8	-46.8	-5.2	5.6	3.2	-26.0
[CH_3 + CH]* $\longrightarrow$ CH_4(gas)+ *C	-40.9	-43.5	126.3	38.3	37.9	-3.5
[CH_3 + CH_2]* $\longrightarrow$ CH_4(gas) + *CH	-52.4	-41.0	241.4	73.1	75.7	28.3

To investigate the impact of these reduced barriers on the kinetics, detailed thermochemistry data have been obtained for the co-adsorption between $*C_1$ and $*C_1$ surface species, and also between $*C_1$ and *H surface species (listed in Table 3.8). TPD simulations were then run in the high-coverage regime, which corresponds to a crowded surface were co-adsorbate effects would be most important. Maximizing the co-adsorption effect by assuming that co-adsorbates diffuse readily, methane production in the resulting simulations shifts down to around 275K in the TPD simulation with different $*CH_2$ initial coverages (0.10, 0.15 and

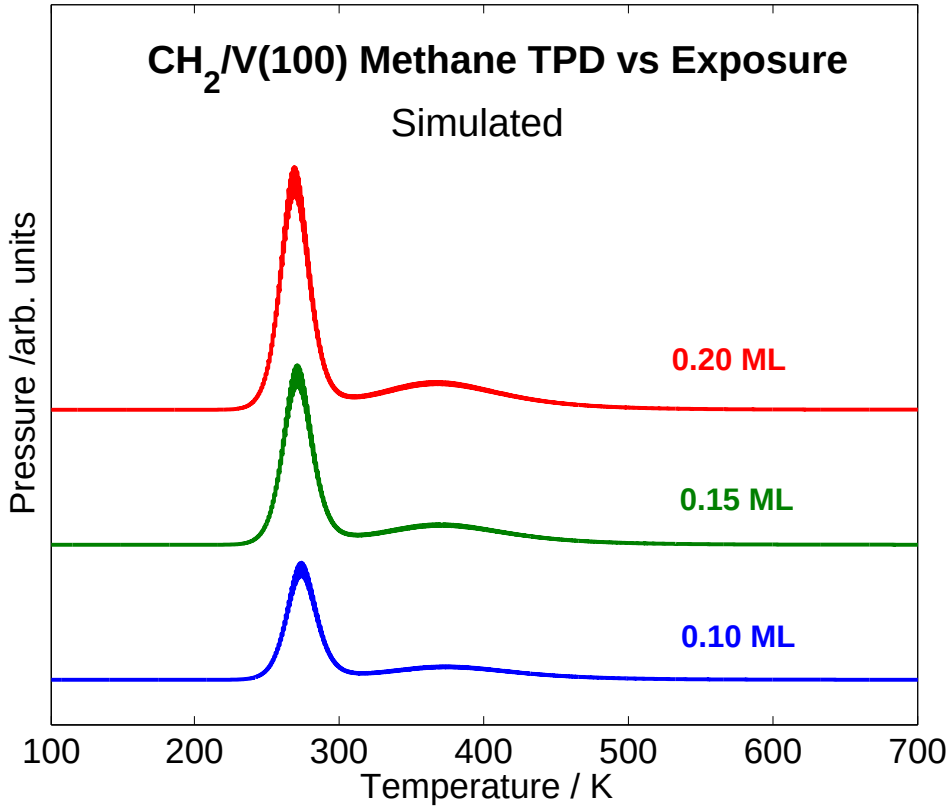

Figure 3.7: Simulated TPD spectra for methane formation on V(100) under different $*CH_2$ initial coverage, with co-adsorption effect. The methane desorption peak is located at 275 K, which agrees well with the experiments.

0.20ML), as shown in Figure 3.7, which is similar to the experimental results.

Flux analysis of the reaction kinetics indicates that the $*C_1$ and $*C_1$ surface species co-adsorbate effects alter the methane formation mechanism. As shown in Figure 3.8, the hydrogen transfer between *CH and $*CH_3$ species is the main source of methane formation. The regular stepwise hydrogenation reactions of $*C_1$ species contribute much less to methane formation in this regime. In Figure 3.9, conversion from two neighboring $*CH_2$ adsorbates to the neighboring *CH and $*CH_3$ species plays an important role from 200K, and then from 230K, hydrogen

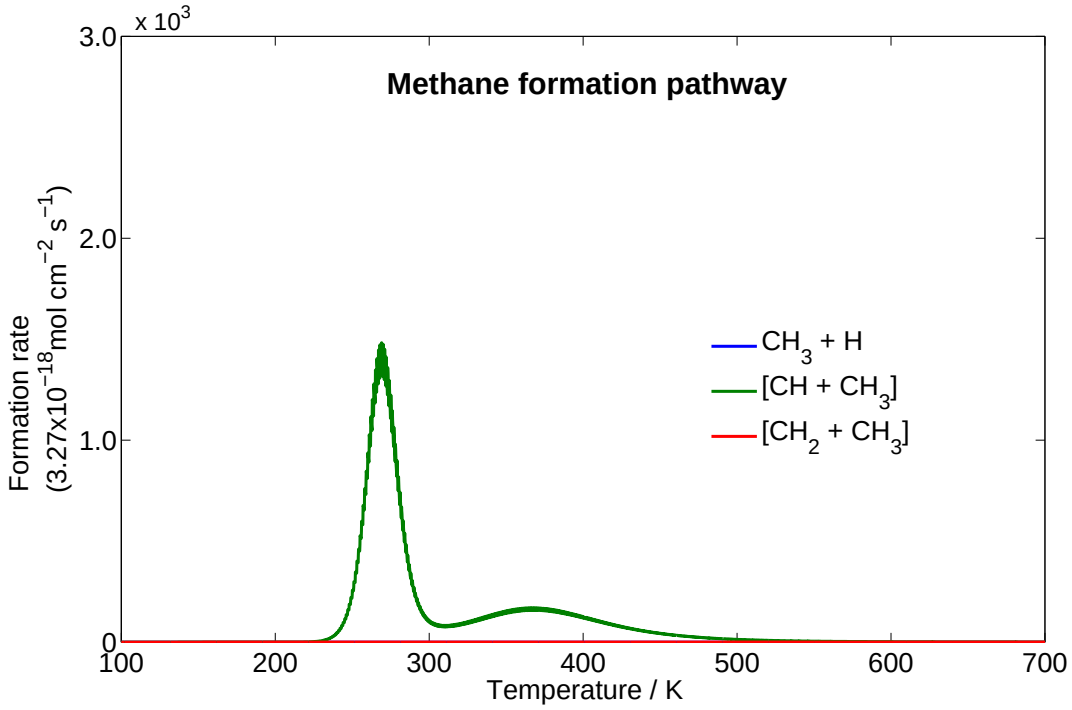

Figure 3.8: Three reaction steps lead to methane formation. The real-time reaction rate indicates only hydrogen transfer from *CH to *CH_3 stimulates the low temperature methane desorption.

transfer from *CH to *CH_3 yields methane desorption with the first strong peak. At 280K, two neighboring *CH adsorbates regenerate *CH_2, which boosts the second round of methane production from 300K with a slower pace. Co-adsorption of *C_1 and *C_1 decreases the barriers effectively, which much lower methane desorption temperature in our simulation. In this way, consideration of co-adsorbate effects will be helpful when the simulation is applied to relatively crowded surface. To fully investigate how these barriers one would need to develop a microkinetic model that considers the local environment of the reactants, using a kinetic Monte Carlo approach or some sort of probability factor to estimate the likelihood that the relevant adsorbates are located near each other. In reality, it is likely that the true chemistry involves a mixture of these co-adsorption reactions and the simpler

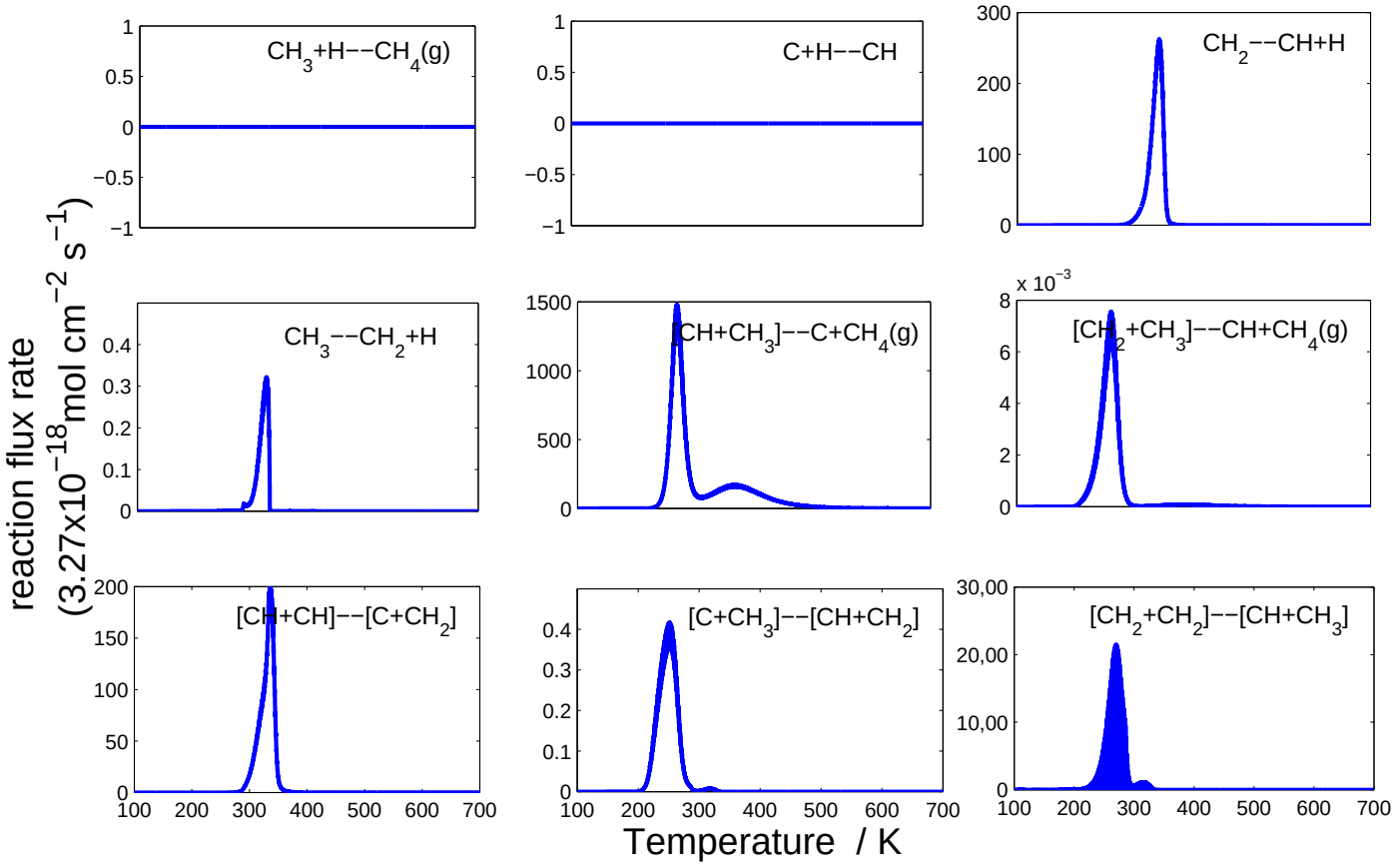

Figure 3.9: Four inactive reactions are related to *C_1 and *H co-adsorption. Conversion from two neighboring *CH_2 adsorbates to the neighboring *CH and *CH_3 species is the first step to approach methane formation. Note that the y-axis scale differs on each plot.

stepwise hydrogenation discussed earlier in this chapter. The neglect of the co-adsorbate effects likely accounts for the temperature shift in the TPD spectrum peaks.

3.5 Conclusions

A first-principles microkinetic model was constructed for methane formation on V(100). At first glance, the DFT results appear to disagree with the experimental observations by predicting a very low barrier for methylene dehydrogenation. However, this apparent discrepancy was resolved by simulating a set of isotopic-substitution temperature programmed desorption experiments. The microkinetic model reproduced the experimental isotopic distribution across a range of plausible initial conditions. It also predicted the formation of the CH_3D isotopomer, which had not been identified in previous experiments but which new experimental data here supports. The discrepancy between the peak positions in the simulations versus the experiments might arise from the neglect of co-adsorbate effects. This study highlights the value of close collaboration between theory and experiments in unraveling complex heterogeneous chemical processes.

In the context of Fischer-Tropsch chemistry on V(100), it was found that methylene dehydrogenation occurs rapidly at lower surface coverages. However, the earlier suggestion that this step occurs slowly was found to be plausible under high-coverage conditions. Still, even in the high-coverage limit, the surface accumulates measurable amounts of methylidyne species, which suggests that they

may be important chain-growth intermediates for Fischer-Tropsch synthesis on V(100).

Chapter 4

Propene-formation on V(100)

4.1 Introduction

Stepwise hydrogenation for methane-formation has been studied in Chapter 3, which validates the combination of DFT calculation and our microkinetic model. But methane is only an undesirable byproduct in FT synthesis: hydrocarbon-chain growth is the heart of FT synthesis. The preferred carbon-carbon coupling steps are still controversial.[23,57–67] Shen and Zaera presented the first strong surface-science data for propene formation via FT synthesis on single-crystal V(100) surfaces. Based on their experiments, they argued for chain-growth via the alkenyl mechanism and a key vinyl intermediates.[77] In this way, propene-formation provides a relatively simple process for investigating FT hydrocarbon-chain growth. Once again, we combine theoretical modeling and the TPD experiments from Shen and Zaera to gain an understanding of propene formation on V(100).

In Shen and Zaera's TPD experiments, methylene surface moieties were gener-

Figure 4.1: Hydrocarbon-chain growth to propene initiated with methylene

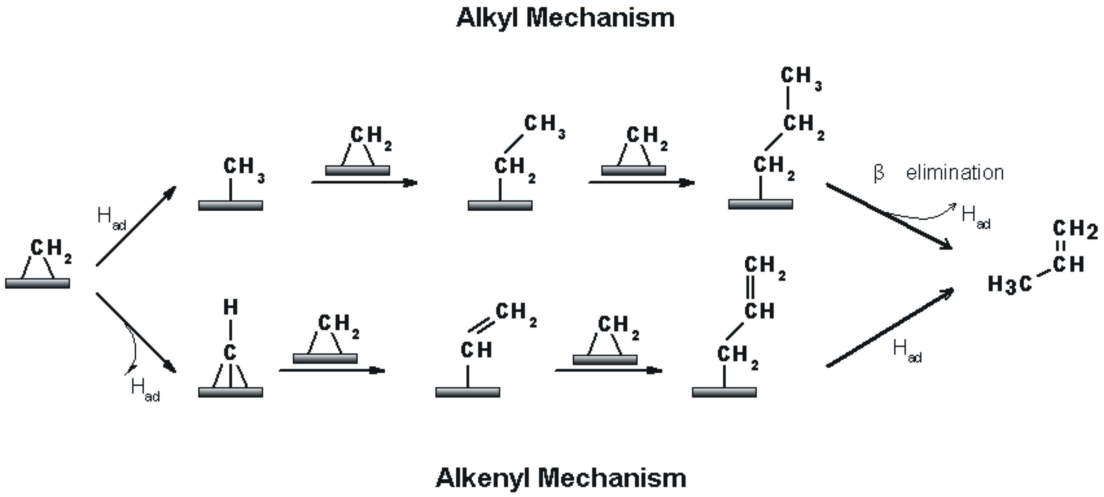

ated on a V(100) single-crystal surface by thermal activation of adsorbed CH_2I_2,.[29,135,136] Hence, the TPD experiments are initiated with $*CH_2$, and reaction pathways to propene formation with the alkyl and alkenyl mechanisms are shown in Figure 4.1.

4.2 Computational details

At first non-spin polarization DFT calculation with PW91[92] functional, were applied to the 2×2 unit cell with a two-layer slab of V(100) surface. The relative low computational cost on two-layer slab model calculations makes it possible to cover more reaction steps involved in propene formation. In the end about 70 reaction steps were used to map the propene formation on V(100) surface. A preliminary microkinetic model (Section 2.4) was constructed to investigate the kinetics. From this preliminary model, 25 key reaction steps were identified on a two-layer slab model. The rate constants and reaction thermochemistry for these key steps were refined using DFT calculations on a thicker four-layer model.

The DFT calculation on four-layer slab model were still initially done with the PW91[91,92] functional, but we also subsequently calculated all of the parameters using another functional, RPBE,[93] which is often believed to be more reliable for computing heats of adsorption.[110] In any case, the results show that the vanadium system is not very sensitive to exchange correlation energy functional. The RPBE rate constants and thermochemistry parameters were used in the microkinetic model to investigate the competition among different reaction pathways to propene formation.

4.3 Results and Discussion

4.3.1 Two-layer slab model

Coupling between two $*C_1$ surface groups is the beginning of hydrocarbon-chain growth. In the preliminary two-layer slab model, we include all possible C_1-C_1 couplings and hydrogenation reactions among $*C_2$ species, which are listed in Table 4.1. In Figure 4.2, it is obvious that the C_1-C_1 coupling barriers are larger than the hydrogenation barriers, which implies that carbon-carbon bond formation will be the rate-limiting steps in propene production. This observation is consistent with other DFT calculations on chain growth on other metal surfaces.[38,69,76] We also observe that the C-CH_3 and CH-CH_3 couplings have relatively low barriers, which may make them important in chain growth. In addition to the C_1-C_1 coupling reactions, the C_1-C_2 coupling reactions subsequent hydrogenation steps

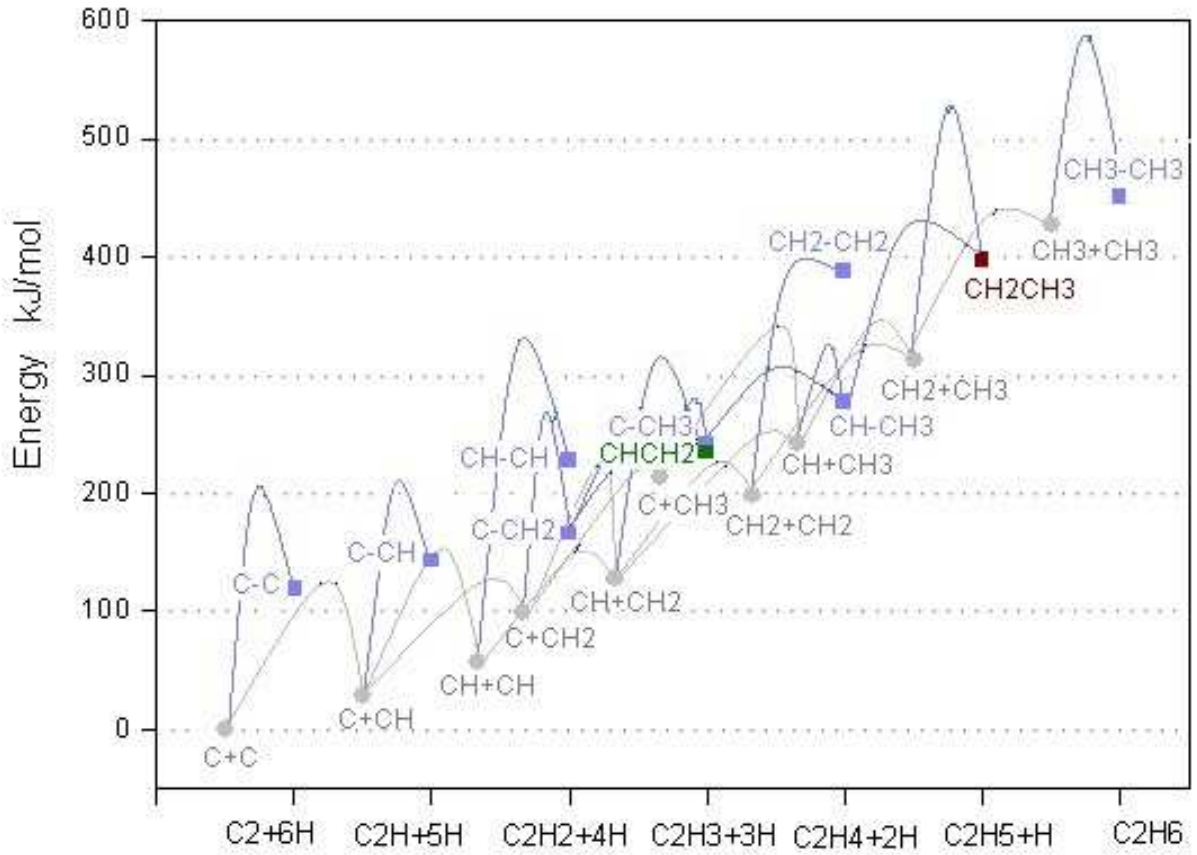

Figure 4.2: C_1-C_1 coupling barriers are larger than hydrogenation barriers. Therefore, C-C coupling steps are expected to play a critical role in the kinetics of hydrocarbon-chain growth.

Table 4.1: Electronic energy profiles for all the possible C_1-C_1 coupling and related hydrogenation reactions on V(100) in the two-layer slab model.

Elementary step	ΔE_{rxn}	ΔE_{act}
C_1-C_1 coupling*		
$*C + *C \longrightarrow *CC + *$	119.6	200.7
$*C + *CH \longrightarrow *CCH + *$	114.4	180.3
$*C + *CH_2 \longrightarrow *CCH_2 + *$	67.4	172.7
$*C + *CH_3 \longrightarrow *CCH_3 + *$	26.9	63.8
$*CH + *CH \longrightarrow *CHCH + *$	171.0	276.0
$*CH + *CH_2 \longrightarrow *CHCH_2 + *$	108.3	201.8
$*CH + *CH_3 \longrightarrow *CHCH_3 + *$	35.5	80.9
$*CH_2 + *CH_2 \longrightarrow *CH_2CH_2 + *$	139.7	198.1
$*CH_2 + *CH_3 \longrightarrow *CH_2CH_3 + *$	84.9	221.5
$*CH_3 + *CH_3 \longrightarrow *CH_3CH_3 + *$	22.8	159.5
Hydrogenation		
$*CC + *C \longrightarrow *CCH + *$	23.1	87.8
$*CCH + *H \longrightarrow *CCH_2 + *$	23.2	84.8
$*CCH + *H \longrightarrow *CHCH + *$	84.9	104.3
$*CCH_2 + *H \longrightarrow *CCH_3 + *$	74.7	76.6
$*CCH_2 + *H \longrightarrow *CHCH_2 + *$	69.2	101.6
$*CCH_3 + *H \longrightarrow *CHCH_3 + *$	36.9	65.0
$*CHCH + *H \longrightarrow *CHCH_2 + *$	7.6	51.0
$*CHCH_2 + *H \longrightarrow *CHCH_3 + *$	42.4	83.2
$*CHCH_2 + *H \longrightarrow *CH_2CH_2 + *$	101.7	120.6
$*CHCH_3 + *H \longrightarrow *CH_2CH_3 + *$	119.7	153.7
$*CH_2CH_2 + *H \longrightarrow *CH_2CH_3 + *$	60.4	78.0
$*CH_2CH_3 + *H \longrightarrow *CH_3CH_3 + *$	53.0	66.7

were also investigated, and their energetics are provided in Table 4.2.

When we focused on C_1 species in Chapter 3, it was found that the surface accumulates methylidyne under both low- and high-coverage regime, which suggests that methylidyne may be an important chain-growth intermediates for Fischer-Tropsch synthesis on V(100). In the examination of the C_1-C_1 coupling reaction barriers involving methylidyne in Table 4.1 and 4.2, it seems that ethylidene (CH-CH_3) might be another important intermediate to consider in addition to vinyl and ethyl. On vanadium, the C_1-C_1 coupling barrier to form ethylidene (CH-CH_3, 80.9kJ/mol) is much lower than the barriers to form vinyl (CH-CH_2, 201.8kJ/mol) or ethyl (CH_2-CH_3, 221.5kJ/mol). In other words, a mechanism in which ethylidene was the key chain-growth intermediate would likely be much faster than pathways involving vinyl or ethyl. In particular, based on analysis of all the potential reaction pathways in Table 4.1 and 4.2, we hypothesize that the ethylidene mechanism in Figure 4.3 would be the preferred route for propene formation. This mechanism first involves the formation of surface *CH and *CH_3, as per the discussion in Chapter 3. These two species couple to form ethylidene. Subsequent insertion of another methylidyne (*CH) produces adsorbed *$CHCHCH_3$, which can then be hydrogenated to form final propene product. In the end, we identified 25 key reaction steps involved in (1) methane formation, (2) the three propene formation mechanisms in Figure 4.4, and (3) ethylene production as a byproduct of the C_2 species. The energetics of these key reactions were refined on the four-layer slab model as described previously (shown in Table 4.3).

Table 4.2: Electronic energy profiles for all the possible C_1-C_2 coupling and related hydrogenation reactions on V(100) in the two-layer slab model.

Elementary step	ΔE_{rxn}	ΔE_{act}
C_1-C_2 coupling		
*CC + *C $\longrightarrow$ *CCC + *	95.9	117.7
*CC + *CH $\longrightarrow$ *CCCH + *	113.6	159.8
*CC + *CH_2 $\longrightarrow$ *CCCH_2 + *	76.0	164.5
*CC + *CH_3 $\longrightarrow$ *CCCH_3 + *	-16.2	75.4
*CCH + *C $\longrightarrow$ *CCHC + *	6.7	67.4
*CCH + *CH $\longrightarrow$ *CCHCH + *	23.9	82.5
*CCH + *CH_2 $\longrightarrow$ *CCHCH_2 + *	65.5	158.6
*CCH + *CH_3 $\longrightarrow$ *CCHCH_3 + *	5.8	120.6
*C + *CCH $\longrightarrow$ *CCCH + *	118.8	308.4
*CH + *CCH $\longrightarrow$ *CHCCH + *	164.3	182.7
*CH_2 + *CCH $\longrightarrow$ *CH_2CCH + *	116.0	208.0
*CH_3 + *CCH $\longrightarrow$ *CH_3CCH + *	35.4	120.4
*CCH_2 + *C $\longrightarrow$ *CCH_2C + *	107.6	111.0
*CCH_2 + CH $\longrightarrow$ *CCH_2CH + *	142.9	149.8
*CCH_2 + *CH_2 $\longrightarrow$ *CCH_2CH_2 + *	180.9	207.4
*CCH_2 + *CH_3 $\longrightarrow$ *CCH_2CH_3 + *	4.2	126.3
*C + *CCH_2 $\longrightarrow$ *CCCH_2 + *	128.2	206.6
*CH + *CCH_2 $\longrightarrow$ *CHCCH_2 + *	163.0	201.8
*CH_2 + *CCH_2 $\longrightarrow$ *CH_2CCH_2 + *	167.3	189.6
*CH_3 + *CCH_2 $\longrightarrow$ *CH_3CCH_2 + *	82.6	110.2
*C + *$CHCH_2$ $\longrightarrow$ *CCHCH_2 + *	71.6	192.3
*CH + *$CHCH_2$ $\longrightarrow$ *CHCHCH_2 + *	124.1	202.6
*CH_2 + *$CHCH_2$ $\longrightarrow$ *CH_2CHCH_2 + *	138.5	211.1
*CH_3 + *$CHCH_2$ $\longrightarrow$ *CH_3CHCH_2 + *	57.7	167.4
*$CHCH_2$ + *C $\longrightarrow$ *CHCH_2C + *	101.9	145.5
*$CHCH_2$ + *CH $\longrightarrow$ *CHCH_2CH + *	134.4	165.7
*$CHCH_2$ + *CH_2 $\longrightarrow$ *CHCH_2CH_2 + *	*not stable*	
*$CHCH_2$ + *CH_3 $\longrightarrow$ *CHCH_2CH_3 + *	15.2	136.3
*C + *CH_2CH_3 $\longrightarrow$ *CCH_2CH_3 + *	-13.4	89.4
*CH + *CH_2CH_3 $\longrightarrow$ *CHCH_2CH_3 + *	38.6	90.7
*CH_2 + *CH_2CH_3 $\longrightarrow$ *$CH_2CH_2CH_3$ + *	50.0	189.5
*C + *$CHCH_3$ $\longrightarrow$ *CCHCH_3 + *	84.7	181.9
*CH + *$CHCH_3$ $\longrightarrow$ *CHCHCH_3 + *	99.5	183.8
*CH_2 + *$CHCH_3$ $\longrightarrow$ *CH_2CHCH_3 + *	130.6	245.8
Hydrogenation		
*$CCCH_2$+*H $\longrightarrow$ *CHCCH_2 + *	65.2	99.7
*$CCCH_3$+*H $\longrightarrow$ *CCHCH_3 + *	45.1	73.4
*$CCCH_3$+*H $\longrightarrow$ *CHCCH_3 + *	74.7	97.5
*CCHC + *H $\longrightarrow$ *CCHCH + *	45.4	125.2
*CCHCH + *H $\longrightarrow$ *CCHCH_2 + *	111.8	193.8
*CCH_2CH +*H $\longrightarrow$ *CCH_2CH_2 + *	97.0	130.5
*CCH_2CH +*H $\longrightarrow$ *$CHCH_2$CH + *	49.4	133.9
*$CHCCH_2$ +*H $\longrightarrow$ *CH_2CCH_2 + *	72.3	114.7
*$CHCHCH_2$ + *H $\longrightarrow$ *CH_2CHCH_2 + *	84.7	140.1
*$CHCHCH_3$ + *H $\longrightarrow$ *$CHCH_2CH_3$ + *	58.7	102.2
*$CHCHCH_3$ + *H $\longrightarrow$ *CH_2CHCH_3 + *	101.2	139.3
*CH_2CCH_2 + *H $\longrightarrow$ *CH_2CCH_3 + *	30.4	71.7
*CH_2CHCH_2 +*H $\longrightarrow$ *CH_2CHCH_3 + *	34.3	91.9
*CH_2CHCH_3 +*H $\longrightarrow$ *$CH_2CH_2CH_3$ + *	39.1	92.3

Figure 4.3: $CHCH_3$ mechanism

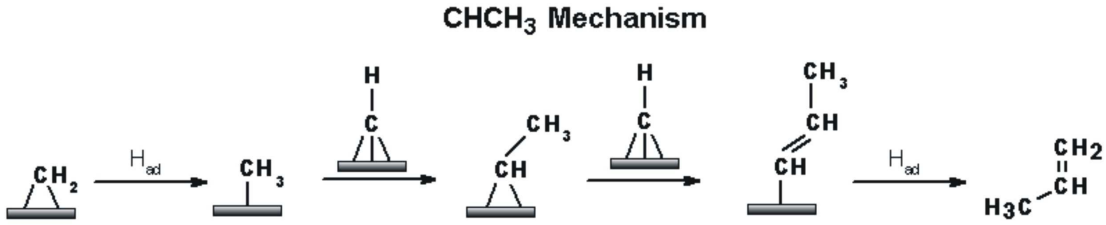

4.3.2 Detailed comparison of the alkyl, alkenyl and ethylidene mechanisms

4.3.2.1 Calculated thermochemistry and reactivity of key reaction steps in propene-formation on V(100)

With the key reaction steps, we refine the thermochemistry data within the four-layer slab model (shown in Table 4.3). Figure 4.5 shows the energy profiles of propene formation from diiodomethane adsorption in TPD experiments on V(100). It is obvious that ethyl formation is hindered both kinetically and thermodynamically relative to vinyl formation, due to large activation barriers and thermodynamically unstable reaction intermediates. Although $*CHCH_3$ is slightly less stable than vinyl, the C-C coupling barrier required to form it is much smaller, which suggests $*CHCH_3$ may be kinetically important in hydrocarbon-chain growth. Potential co-adsorbate interactions appear to preferentially lower the CH-CH_3 coupling barrier relative to the other carbon-carbon coupling reactions, as shown in Table 4.4, where the CH-CH_3 barrier decreases from 124.5 kJ/mol to 81.2 kJ/mol.

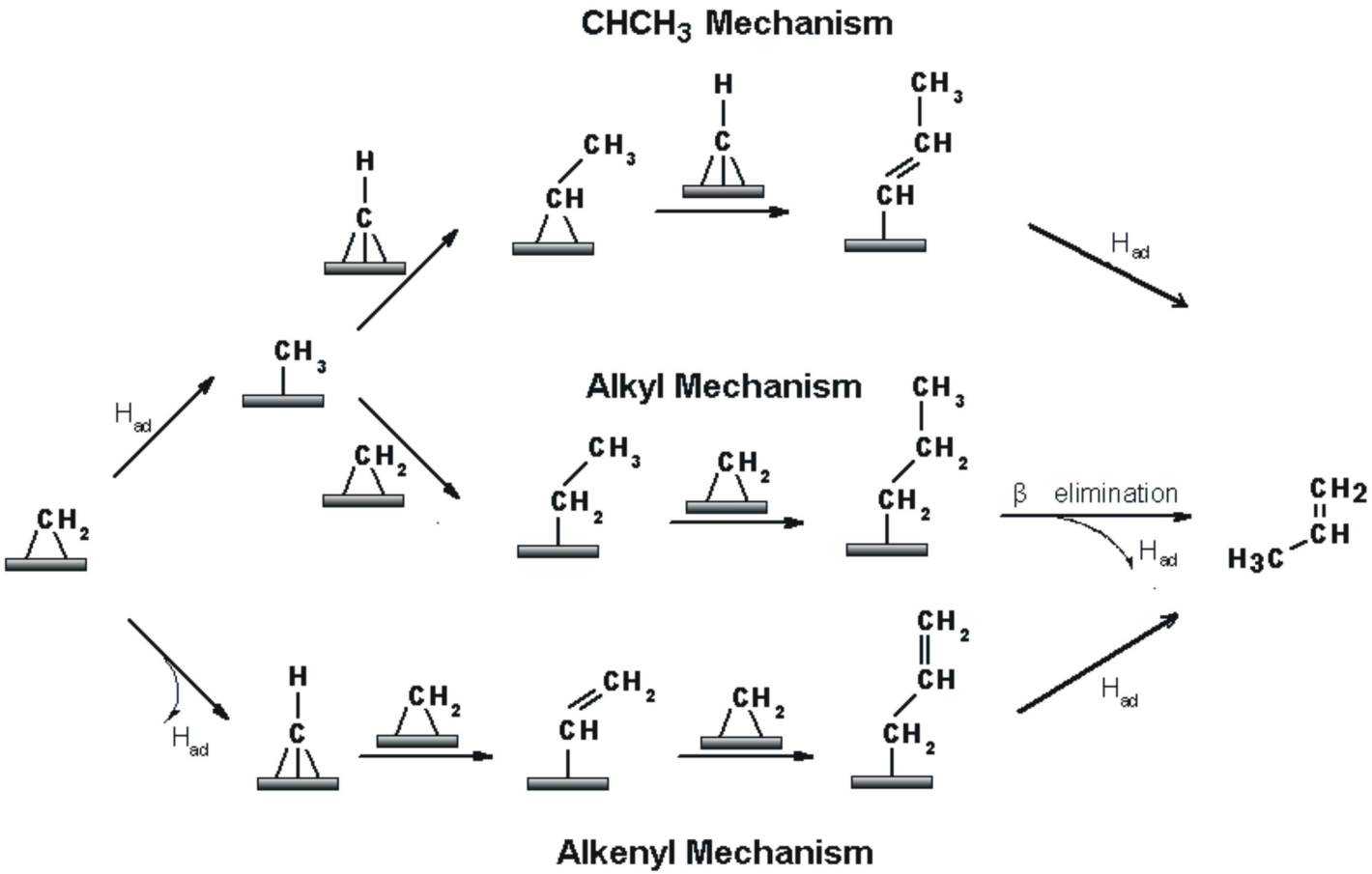

Figure 4.4: Competition among three mechanisms: ethyl *vs.* vinyl *vs.* $CHCH_3$

Figure 4.5: The energetics of propene formation from diiodomethane adsorption in TPD experiments on V(100). And to better describe the energy profile of current three propene-formation mechanisms in the TPD experiments, the thermochemistry of adsorption of diiodomethane should be considered, which was estimated via a thermodynamic cycle for the overall FTS reaction that combines the surface reaction 3 $^*CH_2 \longrightarrow$ propene* + 2 vac^*, the desorption of propene*, and the gas-phase reaction 3 CH_2I_2(g) $\longrightarrow$ propene(g) + I_2(g). The thermodynamics of the last, gas-phase reaction were computed in Q-Chem[137] using B3LYP/6-311G** to avoid the need for an iodine pseudopotential. Though this is a different functional and basis set than those used for the surface reactions, the B3LYP $\Delta H°(298) = -141$ kJ/mol for the gas-phase reaction agrees reasonably well with the NIST experimental range of $\Delta H°(298) = -146$–158 kJ/mol (the range in this value is primarily due to the uncertainty in the diiodomethane measurements).

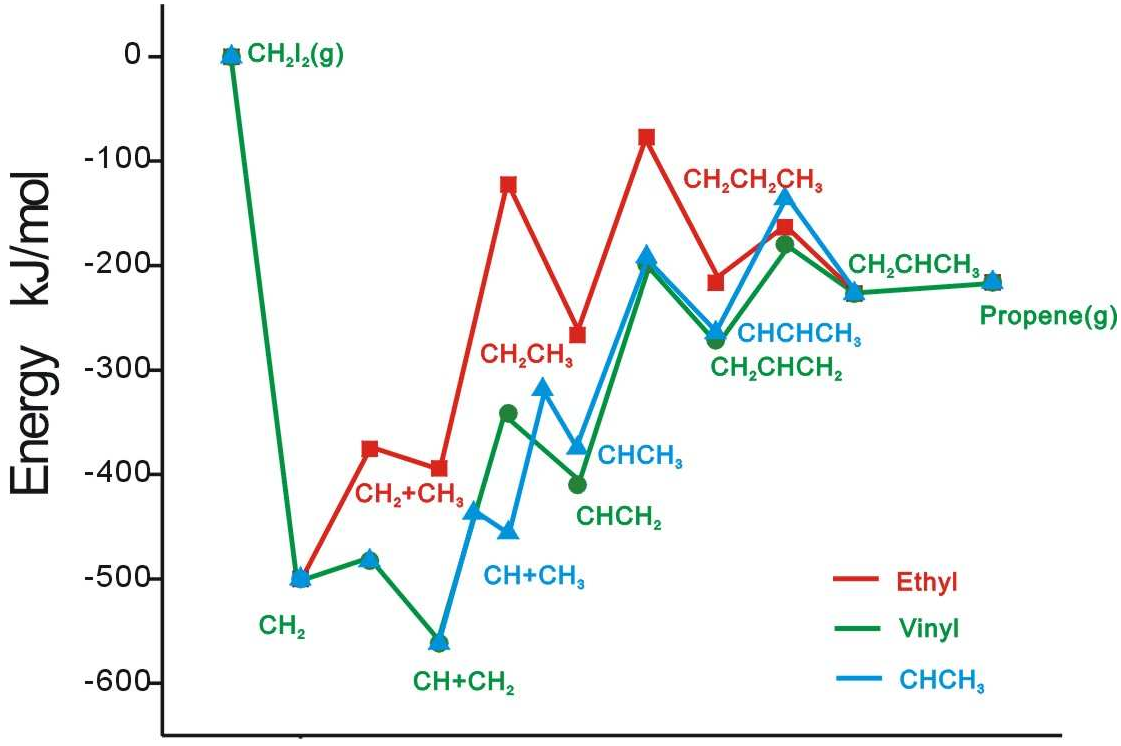

Table 4.3: Thermochemistry for key reaction steps in $C_1 \sim C_3$ gas formation included in the microkinetic model. All thermodynamic functions were evaluated at 300 K and 1 bar.

Elementary step	ΔH_{rxn}(0 K) (kJ/mol)	ΔH°_{rxn} (kJ/mol)	ΔS°_{rxn} (J/mol·K)	ΔH_{act}(0 K) (kJ/mol)	ΔH°_{act} (kJ/mol)	ΔS°_{act} (J/mol·K)
$*CH_3 + *H \longrightarrow CH_4(g) + 2*$	50.5	50.5	116.8	122.3	120.1	-22.1
$*CHCH \longrightarrow CHCH(g) + *$	342.8	346.2	155.3	342.8	346.2	155.3
$*CH_2CH_2 \longrightarrow CH_2CH_2(g) + *$	96.4	98.0	161.6	96.4	98.0	161.6
$*CH_2CHCH_3 \longrightarrow CH_2CHCH_3(g) + *$	17.3	19.0	193.4	17.3	19.0	193.4
$*C + *H \longrightarrow *CH + *$	25.8	36.8	78.5	51.2	56.0	21.1
$*CH + *H \longrightarrow *CH_2 + *$	78.1	74.1	-39.2	89.0	82.1	-74.1
$*CH_2 + *H \longrightarrow *CH_3 + *$	127.7	127.8	-16.2	180.8	178.2	-45.0
$*CH_2 + *H \longrightarrow *CH_3$(4-fold) + *	135.3	134.9	-14.8	131.2	128.1	-40.0
$*CH_3$(4-fold) $\longrightarrow *CH_3$	-7.6	-7.1	-1.4	21.8	18.7	-35.1
$*CH_2 + *CH_3 \longrightarrow *CH_2CH_3 + *$	130.6	127.7	-36.5	276.7	271.9	-45.3
$*CH + *CH_2 \longrightarrow *CHCH_2 + *$	158.6	151.6	-74.8	229.4	220.2	-107.8
$*CH + *CH_3 \longrightarrow *CHCH_3 + *$	91.3	81.1	-110.0	147.0	137.3	-107.2
$*CHCH + *H \longrightarrow *CHCH_2 + *$	54.0	54.3	4.2	89.9	86.3	-44.1
$*CHCH_2 + *H \longrightarrow *CHCH_3 + *$	68.0	64.5	-50.0	102.6	98.0	-57.2
$*CHCH_2 + *H \longrightarrow *CH_2CH_2 + *$	140.9	139.8	-27.7	145.9	140.2	-43.1
$*CHCH_3 + *H \longrightarrow *CH_2CH_3 + *$	117.4	120.7	34.3	161.1	162.7	12.5
$*CH_2 + *CH_2CH_3 \longrightarrow *CH_2CH_2CH_3 + *$	172.8	169.0	-46.2	333.1	327.1	-75.0
$*CH_2 + *CHCH_2 \longrightarrow *CH_2CHCH_2 + *$	217.2	212.4	-67.2	302.8	297.9	-62.8
$*CH + *CHCH_3 \longrightarrow *CHCHCH_3 + *$	132.4	126.2	-63.6	203.4	199.5	-33.5
$*CH_2CH_2CH_3 + * \longrightarrow *CH_2CHCH_3 + H$	-30.1	-31.0	-12.1	33.4	31.8	-8.5
$*CH_2CHCH_2 + *H \longrightarrow *CH_2CHCH_3 + *$	111.0	110.8	-6.8	137.6	136.9	-1.3
$*CHCHCH_3 + H \longrightarrow *CH_2CHCH_3 + *$	205.9	206.7	0.5	255.0	253.2	-16.3
$*CH + *CH \longrightarrow *CHCH + *$	182.7	171.4	-118.2	229.4	216.8	-124.9
$*CH_2 + *CH_2 \longrightarrow *CH_2CH_2 + *$	221.4	217.2	-63.3	289.3	267.4	-129.5
$*CHCH_3 \longrightarrow *CH_2CH_2$	72.9	75.3	22.3	196.4	193.1	-12.9

Table 4.4: Activation energy for C-C coupling steps among co-adsorbed C_1 species on the surface. Evaluated at 300 K and 1 bar. [A + B]* indicates the co-adsorption of both adsorbates.

Elementary step for C-C coupling	ΔE_{rxn} (kJ/mol)	ΔE_{act} (kJ/mol)
$*CH + *CH_3 \longrightarrow *CHCH_3 + *$	61.7	124.5
$[CH + CH_3]* \longrightarrow *CHCH_3$	18.5	81.2
$*CH + *CH_2 \longrightarrow *CHCH_2 + *$	139.9	214.6
$[CH + CH_2]* \longrightarrow *CHCH_2$	126.1	200.8
$*CH_2 + *CH_3 \longrightarrow *CH_2CH_3 + *$	97.4	256.7
$[CH_2 + CH_3]* \longrightarrow *CH_2CH_3$	97.9	257.2
$*CH + *CH \longrightarrow *CHCH + *$	159.0	210.4
$[CH + CH]* \longrightarrow *CHCH$	147.9	199.3
$*CH_2 + *CH_2 \longrightarrow *CH_2CH_2 + *$	200.2	277.0
$[CH_2 + CH_2]* \longrightarrow *CH_2CH_2$	139.6	216.4
$*CH + *CHCH_3 \longrightarrow *CHCHCH_3 + *$	113.6	193.7
$[CH + CHCH_3]* \longrightarrow *CHCHCH_3$	93.4	173.5
$*CH_2 + *CHCH_2 \longrightarrow *CH_2CHCH_2 + *$	189.0	287.1
$[CH_2 + CHCH_2]* \longrightarrow *CH_2CHCH_2$	150.2	160.0
$*CH_2 + *CH_2CH_3 \longrightarrow *CH_2CH_2CH_3 + *$	151.4	323.1
$[CH_2 + CH_2CH_3]* \longrightarrow *CH_2CH_2CH_3$	120.5	200.9

Besides propene, the C_2 gas products (ethylene and ethyne) are also included in our model. According to the DFT calculations, ethyne binds to the surface strongly, and its desorption energy is over 300 kJ/mol. On the other hand, it hydrogenates to ethylene readily, and ethylene desorbs much more easily. In addition, ethylene formation from direct coupling of two CH_2 groups is very slow, with a barrier of 277.0 kJ/mol. This means that gaseous ethylene observed in the experiments probably forms via hydrogenation or dehydrogenation of other $*C_2$ species (perhaps from vinyl or ethylidene, for instance).

Figure 4.6: Experimental TPD spectra for $C_1 \sim C_3$ gas products under different CH_2I_2 exposures: methane production is the dominant reaction pathway for low CH_2I_2 coverages; ethylene and propene desorptions are both observed with higher CH_2I_2 coverages.[102]

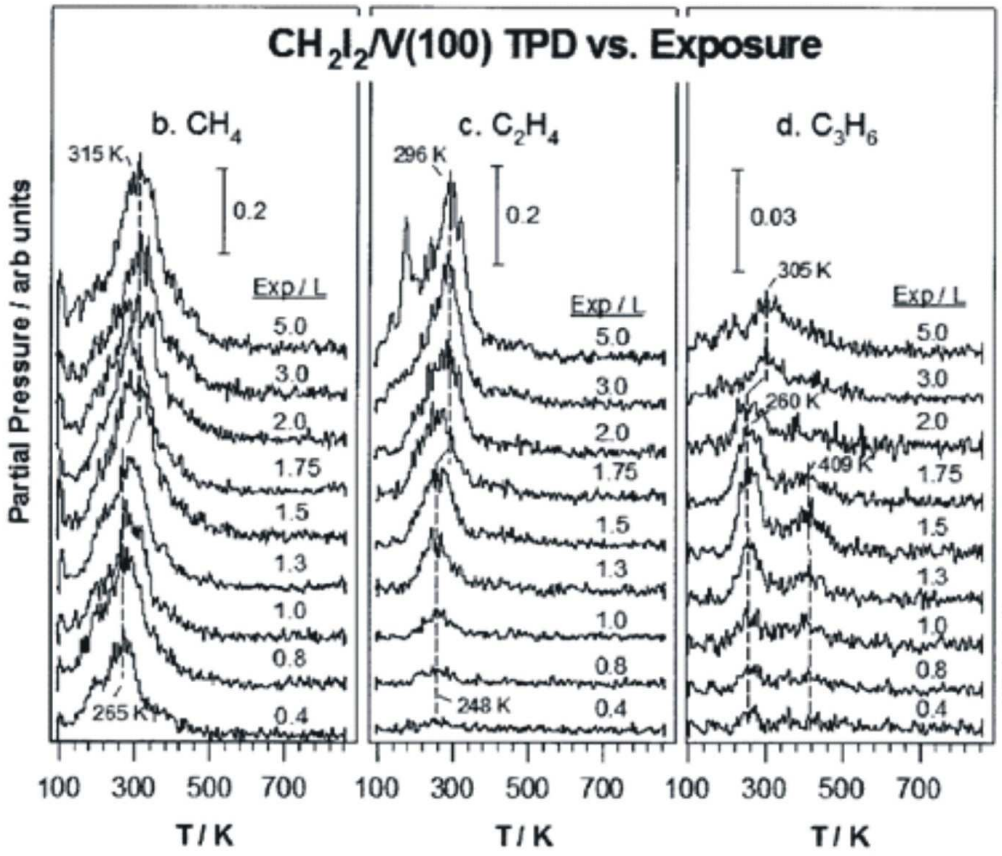

4.3.2.2 Summary of the TPD data to be simulated

Before describing the microkinetic TPD simulations in detail, the TPD experimental data the simulations aim to reproduce are summarized.[77,102] A clean V(100) surface was dosed with various amounts of CH_2I_2 (from 0.4 to 5.0 L) at 110 K and the temperature ramped at a rate of 10 K per second until reaching 1200 K. A variety of gaseous products, including methane (315 K), ethylene (295 K), propene (300 K) were detected and followed via mass spectrometry.

It was observed that the desorption rates of $C_1 \sim C_3$ gas products peak near 300 K (Figure 4.6).[102] Methane production is the dominant reaction pathway for

Figure 4.7: Experimental TPD spectra showing the amount of propene obtained after dosing different combinations of hydrocarbon precursors on V(100). a) Ruling out $*C_2H_5$ and $*C_2H_4$ as major hydrocarbon-chain growth intermediates. b) Propene formation via vinyl intermediate, prepared by bromoethene, iodoethene, or ethyne precursors. c) Propene isotopomer ($C_3H_4D_2$) formation from co-adsorption of [D_2]diiodomethane and vinyl intermediate.[77]

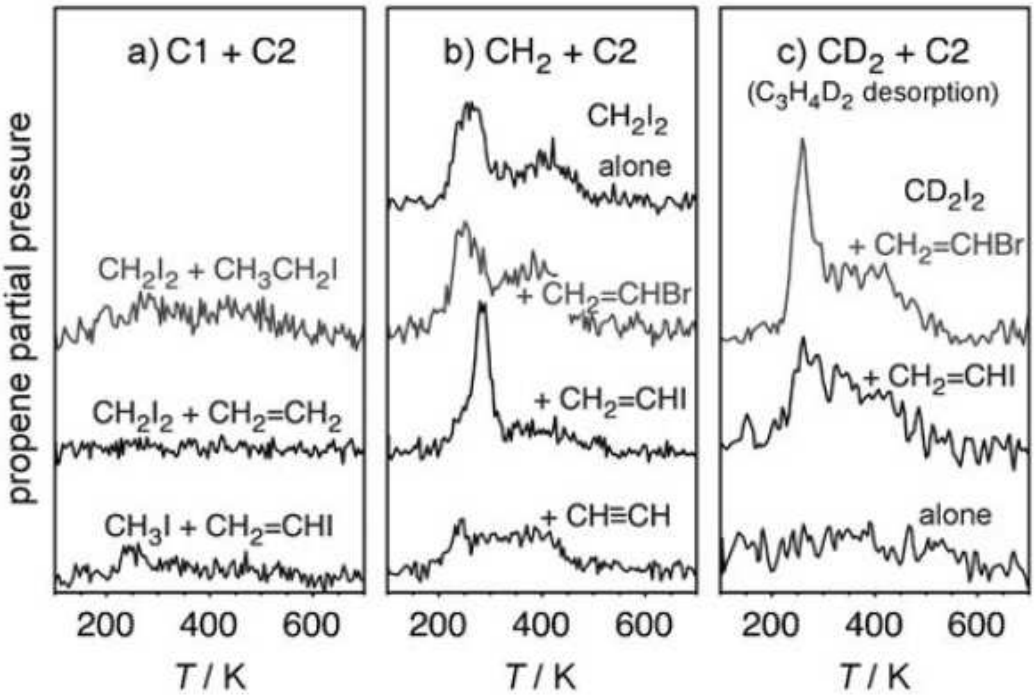

low CH_2I_2 coverages. The desorption yield of ethylene is quite small at low CH_2I_2 coverages, but it does become comparable to that of methane beyond 1.5 L CH_2I_2 exposure. Propene is a minor product in all cases, but again, its production increases with increasing dosages of CH_2I_2.

To help understand the mechanism, Shen and Zaera performed additional TPD experiments in which they co-adsorbed various C_1 and C_2 species to see how that affected the propene yield, as shown in Figure 4.7.[77,102] They inferred that $*CH_2CH_3$ and $*CH_2CH_2$ could not be the possible hydrocarbon-chain growth intermediates, since no significant propene formed after co-adsorbing CH_2I_2 with either ethyl (Figure 4.7 a, top trace) or ethylene (Figure 4.7 a, second trace).

They also argued against the direct coupling between *CH_3 and *$CHCH_2$ (Figure 4.7 a, bottom trace). In contrast, co-adsorbing vinyl with methylene surface species prepared by bromoethene, iodoethene, or ethyne (Figure 4.7 b, bottom three traces) all lead to considerable propene production, which they argued supports a direct CH_2-$CHCH_2$ coupling step in alkenyl mechanism. They also used deuterium isotope labeling experiments with CD_2I_2 (Figure 4.7 c) to argue the last hydrogenation step involves a *CH_2 =$CHCH_2$ intermediate to form propene gas.

4.3.2.3 TPD simulation results with microkinetic model for propene production

The thermochemistry calculated by DFT supports ethylidene surface species as a potential key intermediate as well as vinyl and ethyl. This possibility was not addressed in the earlier experimental work. Therefore, the microkinetic model is used here to assess the role of ethylidene in propene synthesis and to determine whether this alternative mechanism is consistent with the experimental evidence. As before, various model choices and assumptions described in Section 2.4.2 were made regarding the TPD conditions and the behavior of the reaction mechanism. Unlike in Chapter 3, only the high-coverage regime has been considered for ethylene and propene production. Analysis of the kinetics suggests that methane formation will be more likely in the low coverage regime, and this is consistent with the TPD experiments shown in Figure 4.6 that indicate that C_2 and C_3 species are formed in significant quantities only at high coverages. Table 4.5 summarizes

the key initial conditions for the TPD simulations.

Table 4.5: TPD microkinetic model conditions used to initialize the V(100) surface for propene formation.

Initial fractional surface coverages θ_i:	
$*CH_2$	0.10∼0.25 ML
H_2O*	0.10 ML
Vacant sites:	0.01 ML (high coverage)
Temperature program:	
Initial temperature	100 K
Heating rate	1 K per 100 seconds
Final temperature	1000 K

Figure 4.8 shows simulated TPD profiles for gas desorption of methane, ethylene and propene, with the high-coverage regime defined by the conditions specified in Table 4.5, with different $*CH_2$ initial coverages. The relative product yields of methane, ethylene, and propene qualitatively agree with the experiments.[77,102] At lower initial $*CH_2$ coverages, methane is the primary product. As the initial coverage of $*CH_2$ increases, the amount of ethylene produced increases until it is comparable with the methane production. Propene production also increases with increasing doses of initial $*CH_2$, though it is produced in much smaller quantities than methane or ethylene. Moreover, just as in the experiments, no gaseous ethyne production is observed in the simulations.

The key differences between the simulations and experiments are the TPD peak positions. Once again, the peak positions occur around 500 K, instead of near 300 K as in the experiments. As discussed in Chapter 3, this discrepancy may well arise from the neglect of co-adsorbate interactions in the model.

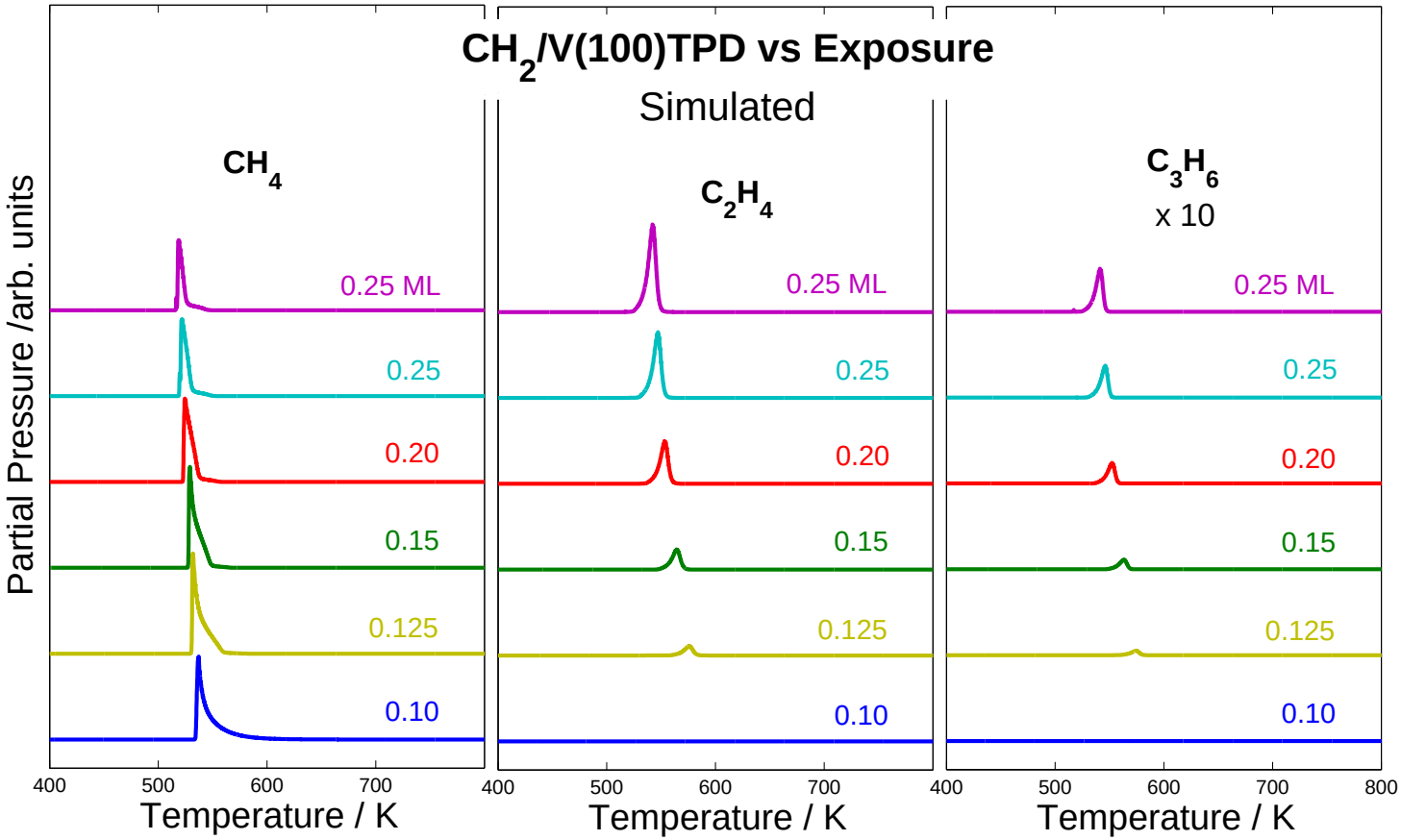

Figure 4.8: Simulated TPD spectra for methane (left side), ethylene(middle) and propene(right side). The peak temperatures in the simulations are shifted to higher temperatures than those seen in the experiments, but the relative desorption yields as a function of CH_2 initial coverage agree reasonably well with those from the experiments.

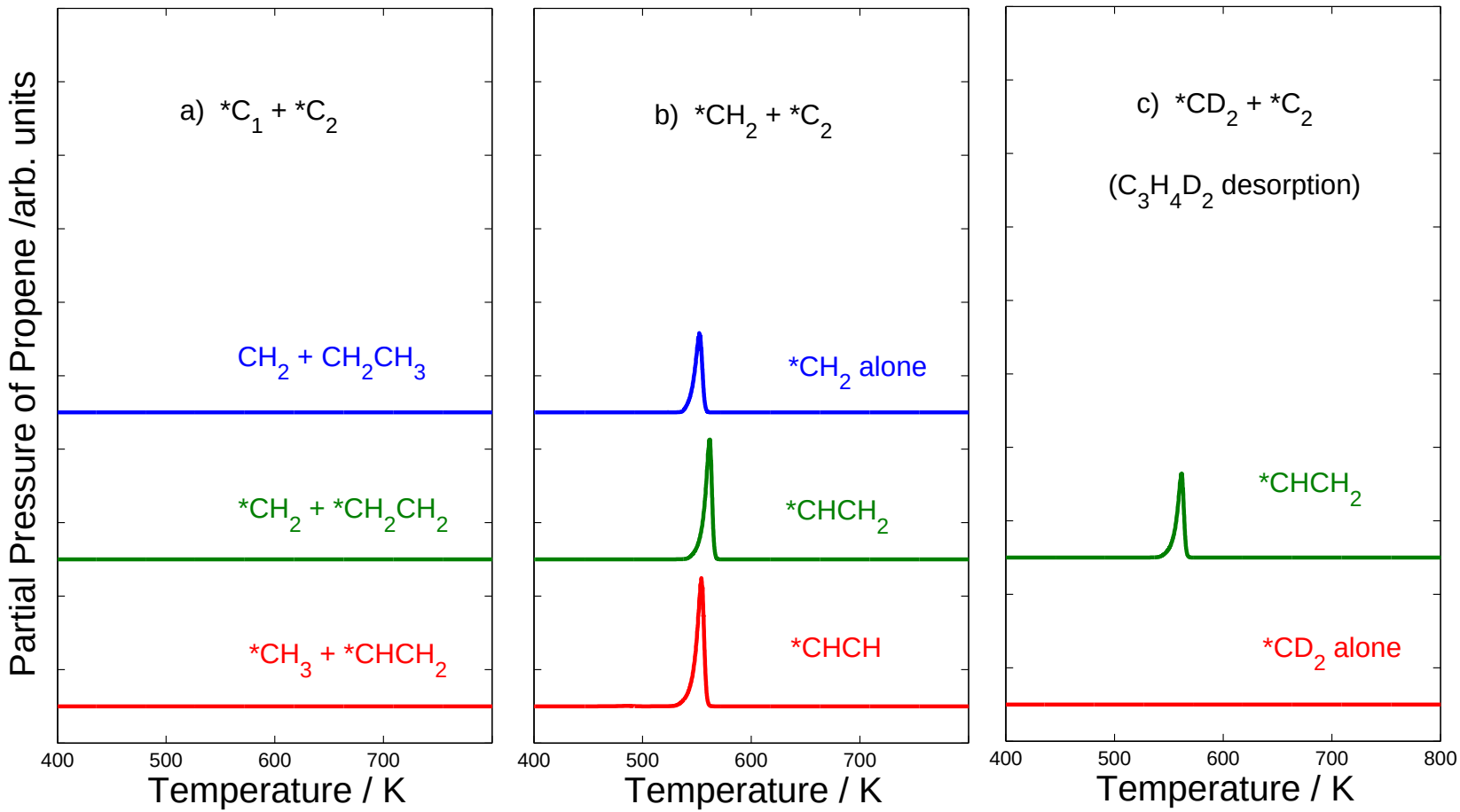

Figure 4.9: Simulated propene TPD spectra obtained after different co-adsorption systems on V(100). Desorption yields of propene agree well with experimental results.[77]

We also investigated initially dosing the surface with both $*CH_2$ and various $*C_2$ species to mimic the TPD experiments in Figure 4.7. Figure 4.9 shows the results, which are similar to those from the TPD experiments. As in the experimental TPD profiles in Figure 4.7, dosing the surface with methylene and ethyl, methylene and ethylene, or methyl and vinyl does not produce propene gas in any significant quantities (Figure 4.9 a). On the other hand, combinations of methylene and vinyl or methylene and ethyne do produce propene (Figure 4.9 b).

We also mimicked the kinetic isotope TPD experiments in Figure 4.9 c by dosing the surface with $*CD_2$ and $*CHCH_2$. Rather than compute explicit kinetic isotope effects for each reaction as was done in Chapter 3, we obtained an estimated isotope effect by averaging over the data in Table 3.2 and other $*C_1 \sim *C_3$ isotope calculations. In this manner, we estimate that dehydrogenation reactions occur approximately three times faster than de-deuteration ones. Secondary isotope effects are typically smaller, so we neglect any effect from deuterium substitution on the carbon-carbon coupling reactions. The resulting isotopically labeled TPD simulation also agrees reasonably well with the experiments in that dosing the surface with a mixture of $*CD_2$ and $*CHCH_2$ yields $C_3H_4D_2$ (Figure 4.9 c).

Overall, while the TPD peaks occur at too high of temperatures in the simulations, the model accurately reproduces many key qualitative observations from the Shen and Zaera experiments.

4.3.2.4 Real-time flux analysis

Flux analysis was used to interpret detailed mechanism which leads to the simulation results described above.

Reaction flux rates for each step in the alkenyl, alkyl and ethylidene mechanisms are shown in Figure 4.10. On every stage to propene production, C_1-C_1 coupling, C_1-C_2 coupling and hydrogenation/dehydrogenation to propene adsorbates, reaction fluxes along the ethylidene mechanism surpass the others. In addition, Figure 4.11 clearly shows that hydrogenation of $CHCHCH_3$ in the ethylidene mechanism is the dominant pathway to propene production. Virtually no propene is formed via the alkenyl or alkyl mechanisms. We also observe that ethylene formation occurs via the hydrogenation of vinyl (Figure 4.11), which is consistent with what was inferred from the DFT calculations in Section 4.3.2.1.

Figure 4.12 shows that the coverage of surface species during the TPD simulations. Ethyl, ethylidene and vinyl all do appear on the vanadium surface. At first, the lack of surface sites hinders dissociation of CH_2, and methylene hydrogenation occurs more readily, followed by CH_2-CH_3 coupling and also CH-CH_3 coupling later. When the surface is not that crowded after methane desorption at 450 K, ethyl is dissociated back to methylene and methyl surface species. From 520 K, the hydrocarbon-chain growth continues from $*C_2$ species to $*C_3$ species through $*CHCH_3$ intermediate. Meanwhile vinyl is formed from dehydrogenation of $*CHCH_3$, and then yields ethylene desorption after hydrogenation. In this way,

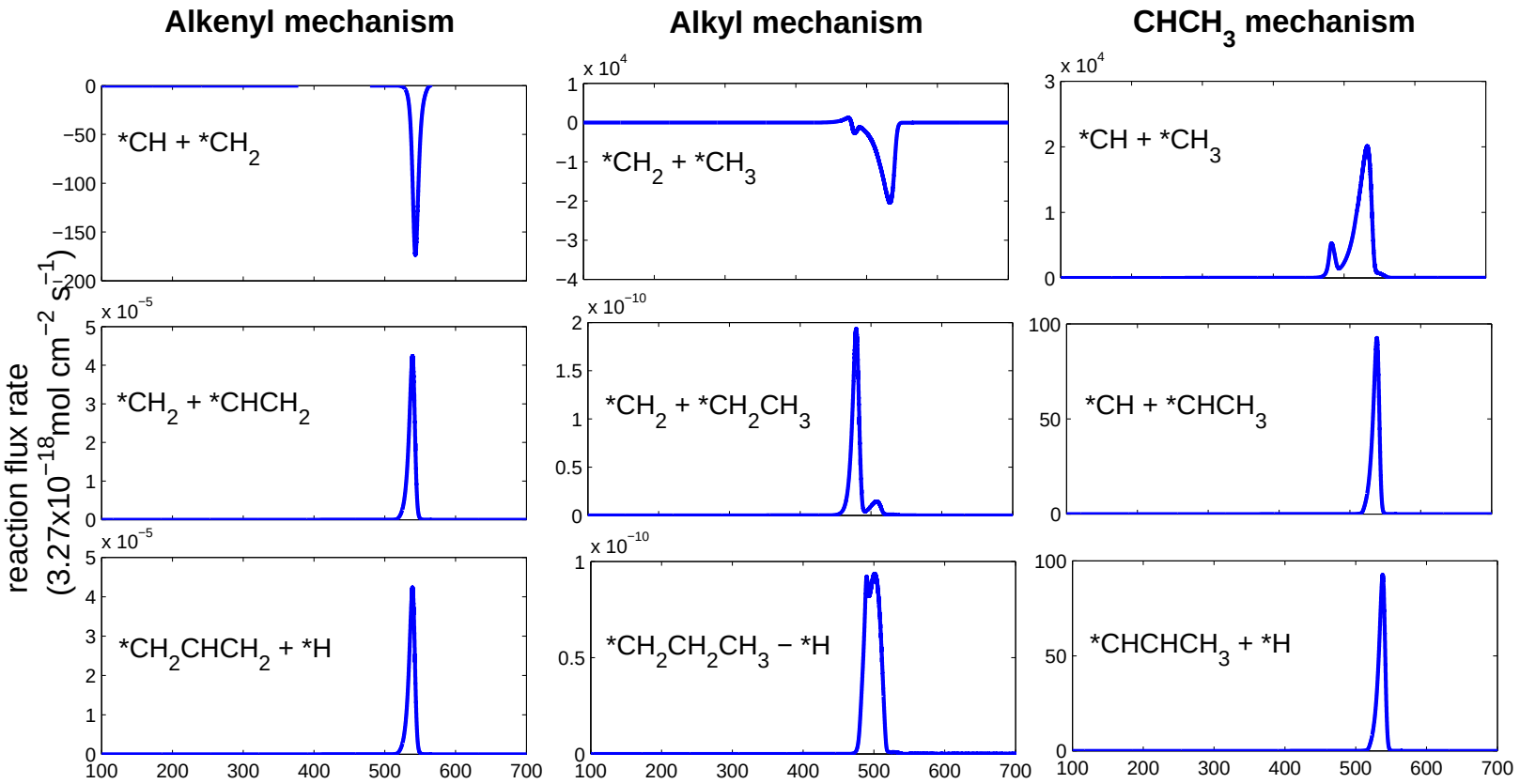

Figure 4.10: Flux rates for each step in alkenyl, alkyl and $CHCH_3$ mechanism: on every stage to propene production, C_1-C_1 coupling, C_1-C_2 coupling and hydrogenation/dehydrogenation to propene, $CHCH_3$ mechanism has the dominant contribution. Note that the y-axis scale differs on each plot.

Figure 4.11: Preferred pathway for propene and ethylene formation. The real-time reaction rate indicates hydrogenation of $CHCHCH_3$ is the last step to propene production; ethylene forms from the hydrogenation of vinyl.

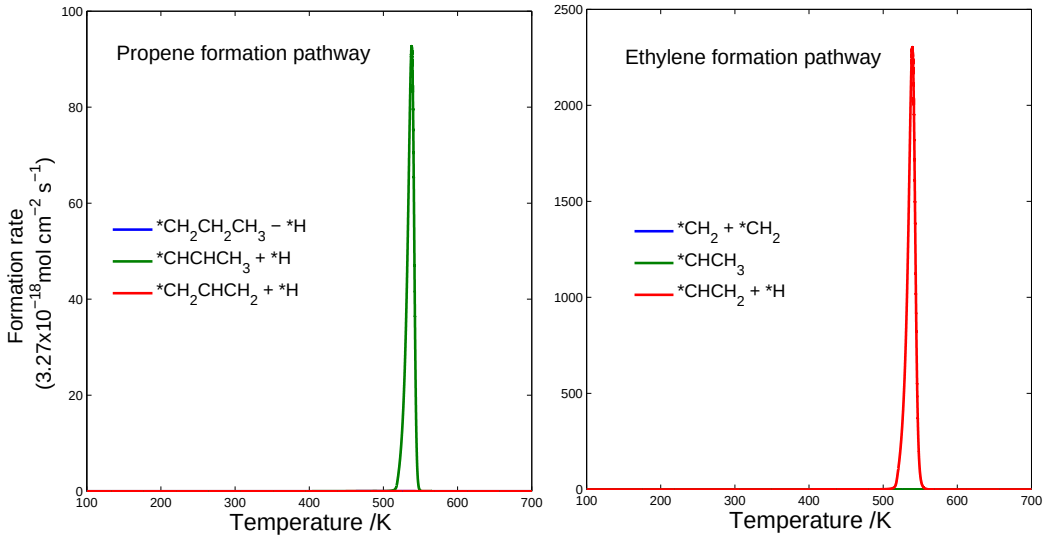

neither ethyl nor vinyl contributes significantly to propene formation. Even the ethylene production could be traced to the dehydrogenation of ethylidene to vinyl.

Flux analysis also enables us to understand the results of the different initial dosing combinations in Figure 4.9. In particular, when methylene and ethylene are dosed together (Figure 4.9 a, middle trace), fast desorption of ethylene prevents significant propene production. When methylene and ethyl are combined (Figure 4.9 a, top trace), the ethyl dehydrogenates rapidly to form ethylene and desorbs without forming propene. In contrast, the combination of methylene and vinyl or methylene and ethyne (Figure 4.9 b, bottom two traces) produces propene because both vinyl and ethyne can be hydrogenated to form the key ethylidene intermediate. Finally, the propene isotopomer $C_3H_4D_2$ production which was observed in experiments that co-adsorbed $*CD_2$ and vinyl (Figure 4.9 c, top trace) does not result from CD_2-$CHCH_2$ coupling, but from $CHCH_2D$-CD coupling (Fig-

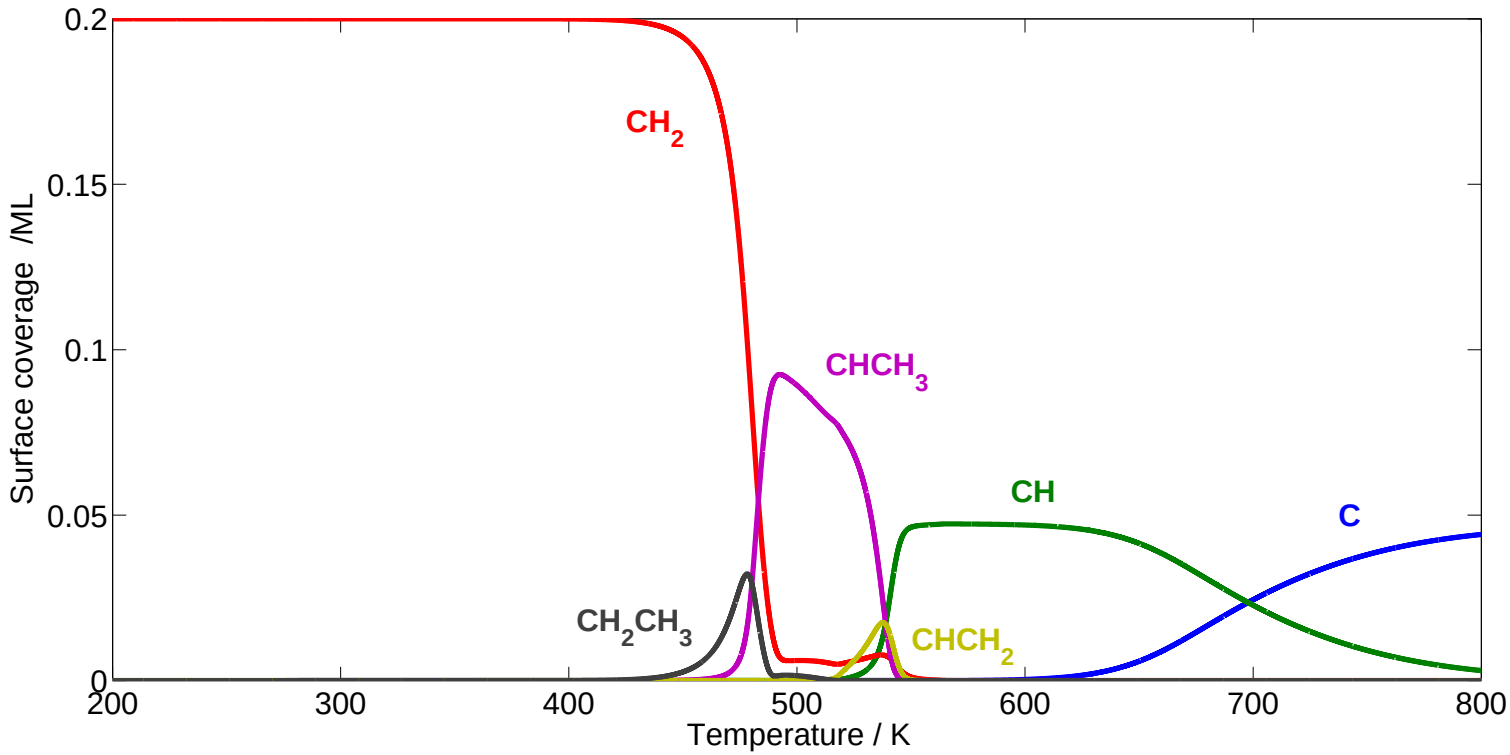

Figure 4.12: Evolution of the surface coverages of all detectable adsorbates as a function of time estimated from our microkinetic modeling of the TPD experiments with $^*CH_2$ on V(100).

ure 4.9 c, top trace). Overall, our model reproduces the major experimental TPD observations well. However it attributes these results to a mechanism in which ethylidene, not vinyl, is the key chain-growth intermediate.

4.4 Comparison with the mechanism on traditional FT catalysts

4.4.1 Background

Our studies of FT chemistry on V(100) in Chapter 3 and 4 suggest that ethylidene is a key reaction intermediate in hydrocarbon-chain growth. Although vanadium-based catalysts have many important applications in industry, e.g. vanadium phosphorous oxide (VPO) in converting n-butane to maleic anhydride,[138] and vanadium oxides applied in the partial oxidation of hydrocarbons,[139,140] metallic vanadium is still a poor FT catalyst. Metallic vanadium oxidizes readily, produces large amounts of methane instead of longer-chain hydrocarbons due to the high activation barriers for the chain-growth reactions. In FT synthesis, the syngas production via steam reforming typically accounts for 60-70% of the capital costs of the total plant.[71] Therefore, maximum utilization of syngas in the FT reactors is very important. Methane formation, which is the reverse process of steam reforming, is unfortunately an undesirable by-product of FT synthesis. In this way, suppressing methane-formation is necessary, and the selectivity toward hydrocarbon-chain growth over methane formation is a key criterion used to judge

FT catalysts. To better understand the FT chemistry, the study on practical FT catalyst metals is necessary.

Across the periodic table, only Ru, Fe, Co and Ni, have enough activity for commercial utilization. Ni is too hydrogenating and mainly produces unwanted methane, like vanadium. Ru has the highest activity and selectivity towards long-chain hydrocarbons, but it is expensive and found in low abundance on earth, making it impractical for large-scale application. Hence, Fe and Co are typically employed in industry at present, since they are much cheaper while maintaining fairly good selectivity. Fe is better for high-temperature FT processes (573-623K), with the yields of C_1-C_{15} hydrocarbons and a large fraction of valuable chemicals such as α-olefins and oxygenates. Fe and Co both work in low-temperature FT processes (473-513K), which leads to the production of linear long-chain hydrocarbons (ultra-clean diesel fuels). Since most FT research has focused on using it to produce liquid fuels, most FT technologies developed in the last two decades utilize the low-temperature process. Co is considered as the optimal choice for the synthesis of long-chain hydrocarbons, although it is more expensive than Fe.[141]

There are already some DFT calculations on the practical FT catalysts (e.g. Co, Fe and Ru) in the scientific literatures. Hu's group investigated methane selectivity on Rh, Co, Ru, Fe, Re flat and stepped surfaces, and believes that C-CH and CH-CH coupling might be preferred in the competition between hydrogenation to methane and hydrocarbon-chain growth, according to the estimation of effective barriers (ΔE_{eff}).[48,68–73] Studies on the Ru(0001) surface by the van Santen group indicate that CH-CH_2 and CH-CH_3 are important on that catalyst.[35,74,75] Calcu-

lations from the Ziegler group focused on the Fe(100) surface, and their reaction energy profiles suggest that CH-CH_3 might be a key intermediate.[38,76]

Among current DFT calculations focused on FT synthesis, basically there are two methods to determine the important reaction pathways: (1) qualitative analysis on energy profiles, higher reaction barriers, lower reaction rates;[38,76] (2) quantitative microkinetic modeling to analyze the detailed kinetics, as we have done in Chapter 3 and 4. Mechanisms through ethyl, vinyl and ethylidene intermediates will be tested with the above three method, which could bring us a general idea about the FT chemistry on several catalysts.

4.4.2 Comparison of reaction energetics and kinetics

4.4.2.1 Computational details

In this section, we combine DFT predictions from a number of different studies. The calculation parameters (e.g. planewave cutoff energies and k-point sampling), the exchange-correlation functionals and model surfaces used vary across the different studies (Table 4.6). This should not cause significant problems, however, since the energy profiles for any particular elementary reaction step from different groups are not compared quantitatively. We investigate the mechanism competition on the same catalyst surface, and then only compare the kinetically dominant mechanisms across different catalysts.

Table 4.6: Summary on computational details of literature data, with DFT calculation on practical FT catalysts

	Hu group[71]					Ziegler group[38,76]	van Santen group[35,74,75]	Our group
Software package	SIESTA					VASP	VASP	DACAPO
Exchange-correlation functional	GGA-PBE GGA-PBE					GGA-PW91 (exchange-correlation effects) GGA-usPPS (ion-electron interaction)	GGA-PW91 (exchange-correlation effects) GGA-usPPS (ion-electron interaction)	GGA-RPBE
Cut-off energy	200 Ry					360 eV	300 eV	340 eV
K-points	$4 \times 5 \times 1$					$7 \times 7 \times 1$	$5 \times 5 \times 5$	$4 \times 4 \times 4$
Locate TS	Constrained optimization					ciNEB	NEB	NEB + TS search
Catalyst surface	Rh	Co	Ru	Fe	Re	Fe(100)	Ru(0001)	V(100)
Spin	×	✓	×	✓	×	✓	×	×

Table 4.7: Energy profile for propene formation on Fe(100) surface, obtained by Ziegler group.[38,76]

Elementary step on Fe(100)	ΔE_{rxn} (kJ/mol)	ΔE_{act} (kJ/mol)
$*CH_2 + *CH_3 \longrightarrow *CH_2CH_3 + *$	24	145
$*CH + *CH_2 \longrightarrow *CHCH_2 + *$	31	114
$*CH + *CH_3 \longrightarrow *CHCH_3 + *$	42	84
$*CH_2 + *CH_2CH_3 \longrightarrow *CH_2CH_2CH_3 + *$	-57	44
$*CH_2 + *CHCH_2 \longrightarrow *CH_2CHCH_2 + *$	-15	95
$*CH + *CHCH_3 \longrightarrow *CHCHCH_3 + *$	0	70
$*CH_2CH_2CH_3 + * \longrightarrow *CH_2CHCH_3 + H$	20	55
$*CH_2CHCH_2 + *H \longrightarrow *CH_2CHCH_3 + *$	-13	98
$*CHCHCH_3 + H \longrightarrow *CH_2CHCH_3 + *$	-3	71

4.4.2.2 Qualitative analysis on energy profiles

Reaction barriers pay a critical role in determining reaction kinetics, so simple analysis of the reaction energy profiles provides valuable information about the mechanism competition. In the methane-formation in Figure 4.13, vanadium surface shows qualitatively similar chemistry to the other catalysts, including the traditional FT catalysts Co and Fe. Specifically, methylene is not the most stable species. Instead, it can dehydrogenate quickly to methylidyne and hydrogen surface species.

For propene formation, the Ziegler group performed DFT calculations on the Fe(100) surface,[38,76] as seen in Table 4.7. Just as for V(100), ethylidene formation exhibits a significantly lower activation barrier (84 kJ/mol) than vinyl (114 kJ/mol) or ethyl (145 kJ/mol), suggesting that ethylidene may also be an important intermediate on Fe.

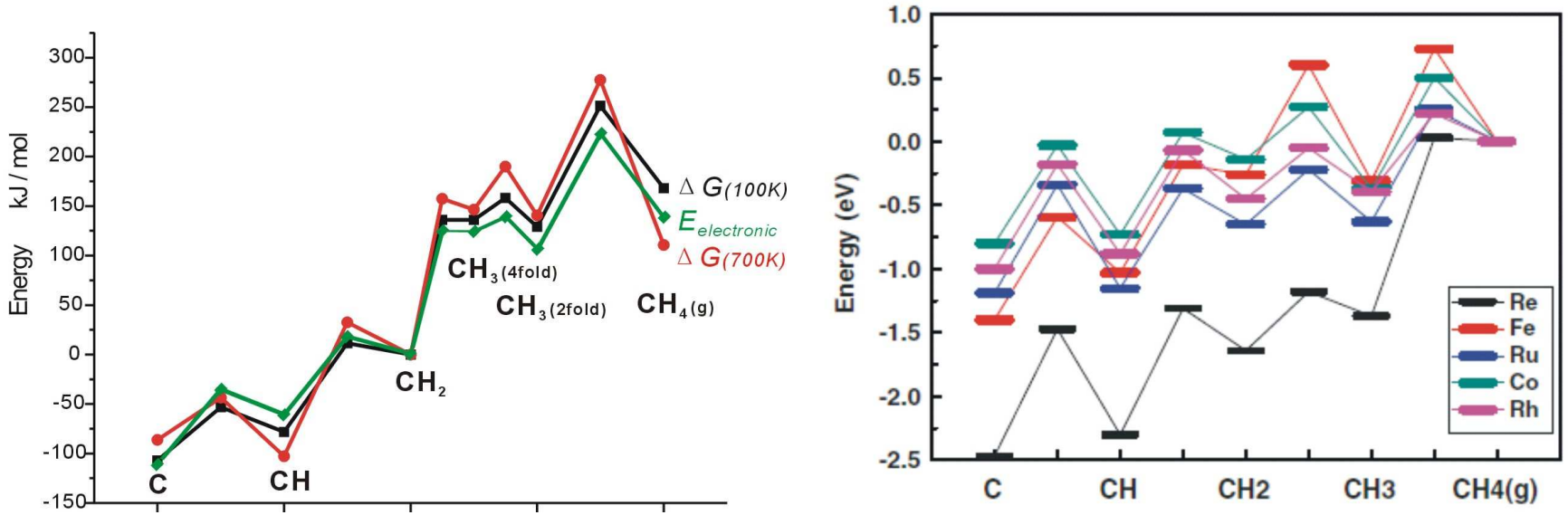

Figure 4.13: Energy profiles of C_1 species on Re, Fe, Ru, Co, Rh surfaces (right frame) obtained by Hu group[71] and energy profiles of C_1 species on V surface (left frame) obtained by our group.

4.4.2.3 Quantitative analysis on the real-time reaction flux

Using the reaction energetics in Table 4.7,[38,76] we adapted our microkinetic model to Fe(100). With 0.20 ML initial coverage of CH_2, at a constant temperature of 534 K (similar to the industrial FT temperatures), CH-CH_3 coupling is still the dominant pathway for hydrocarbon-chain growth (Figure 4.14), just as we saw on V(100).

However, unlike vanadium, iron promotes chain growth due to the lower carbon-carbon coupling reaction barriers. Propene accounts for roughly 20% of the production on iron in our simulations, compared to less than 2% on vanadium. Overall, these comparisons suggest that the FT mechanism behaves similarly on iron and vanadium. Therefore, the Shen and Zaera experiments on V(100) may provide insights onto the chemistry occurring on iron. Further investigation is needed to determine how this mechanism compares to that which occurs on cobalt.

Figure 4.14: Flux analysis on Fe surface: CH-CH_3 coupling is the dominant pathway at the beginning of hydrocarbon-chain growth.

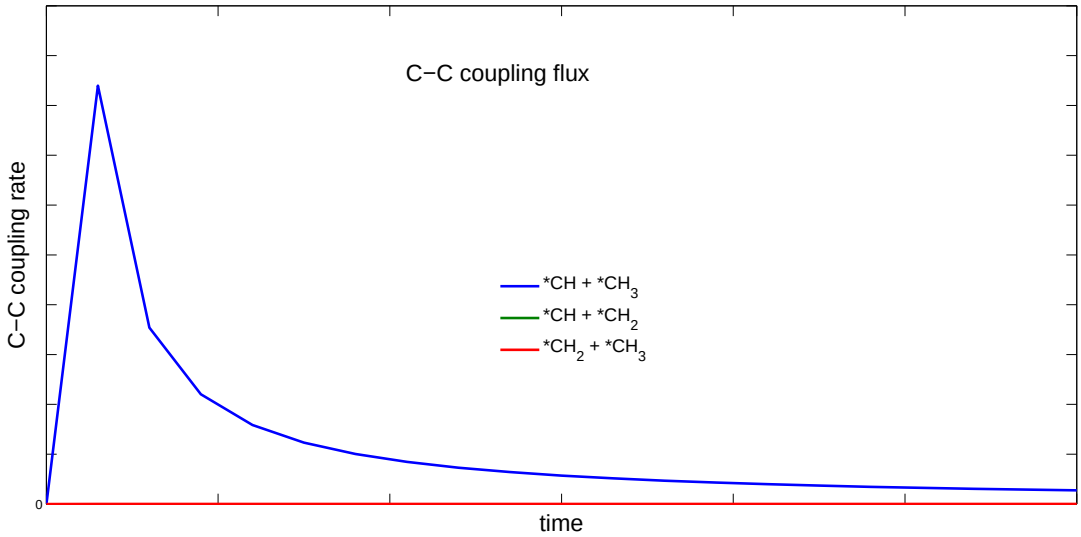

4.5 Conclusions

The mechanism leading to the production of C_1-C_3 hydrocarbons (e.g. methane, ethylene and propene) in FT chemistry on V(100) are explored. The DFT calculations here support inferences from earlier studies that the alkyl mechanism is too energetically unfavorable to play a significant role in FT propene synthesis on V(100). The earlier studies had argued for the alkenyl mechanism instead. However, the model developed here suggests a new interpretation of the experiments in which ethylidene, $*CHCH_3$, is the key chain-growth intermediate.

A microkinetic model was constructed to find out the active pathway(s) for propene formation, among alkenyl, alkyl and $CHCH_3$ mechanism. A set of simulations based on this model qualitatively reproduce the experimental TPD profiles with desorption yields of methane, ethylene and propene. Flux analysis indicates vinyl and ethyl almost have no influence on hydrogen-carbon chain growth to $*C_3$ species, while $*CHCH_3$ appears to be the critical intermediate.

We also compared our model predictions for Fischer-Tropsch synthesis on V(100) with other DFT predictions on the surfaces of traditional Fischer-Tropsch catalyst surfaces such as cobalt, iron and ruthenium.[35,38,68,69,71,74–76,142] While more study is needed before conclusions can be drawn regarding the cobalt and ruthenium surfaces, the ethylidene mechanism appears to be viable on iron surfaces. The similarity of the predicted mechanisms on iron and vanadium suggest that the Shen and Zaera experiments on vanadium may indeed provide useful experimental insights into iron-catalyzed Fischer-Tropsch synthesis.

Chapter 5

Conclusions

Fischer-Tropsch (FT) synthesis has long been one of most important industrial reactions for synthetic fuel production, but much controversy still surrounds the nature of the hydrocarbon chain-propagation intermediates: does it involve the alkyl mechanism with an ethyl intermediate, the alkenyl mechanism with a vinyl intermediate, or some alternative mechanism? The temperature-programmed desorption and x-ray photoelectron spectroscopy experiments by Shen and Zaera[77] provided the first strong surface-science data for this chemistry occurring on vanadium (100) under ultrahigh vacuum. Based on this data, they argued that vinyl formation and its coupling with methylene were the key propene formation steps. However, it was unclear if this was the best interpretation for the data and how meaningful those experiments were for the chemistry occurring on more practical transition metal catalysts.

Compared to studies on complex real-world catalysts, the single-crystal, ultrahigh vacuum experiments provide an excellent opportunity of validating DFT

predictions of the Fischer-Tropsch surface chemistry and building toward a unified theoretical and experimental interpretation of the mechanism. Specifically we investigated whether the alkenyl mechanism is favored over the alkyl mechanism, and whether one of those mechanisms or some alternative mechanism provided the best explanation for the experimental data on V(100). A first-principles microkinetic model with DFT calculation results was constructed to investigate Fischer-Tropsch chemistry on V(100), with particular emphasis on identifying the key hydrocarbon-chain growth intermediates.

The model was first implemented to focus on C_1 groups and the relatively simple chemistry of methane production. Initially, the DFT results appeared to disagree with the experimental observations by predicting a very low barrier for methylene dehydrogenation. However, this apparent discrepancy was resolved by simulating a set of isotopic-substitution temperature programmed desorption experiments. The microkinetic model reproduced the experimental isotopic distribution across a range of plausible initial conditions. It also predicted the formation of the CH_3D isotopomer, which had not been identified in previous experiments but which new experimental data here supports. According to the model, the experimental data that was previously used to argue that methylene dehydrogenation is rate-limiting results from some combination of limited residual background hydrogen in the experimental system and/or limited vacant vanadium surface sites at which the dehydrogenation can occur. This study highlights the value of close collaboration between theory and experiments in unraveling complex heterogeneous chemical processes.

Next, a more complete model describing the production of C_1-C_3 hydrocarbon products (e.g. methane, ethylene and propene) in FT chemistry was explored. The DFT calculations agree well with the experimental inferences that the alkyl mechanism is kinetically hindered compared to the alkenyl one. More significantly, we identified ethylidene ($*CHCH_3$) as another potential key intermediate. The ethylidene mechanism exhibits comparatively low C-C coupling activation barriers that facilitate hydrocarbon-chain growth. Microkinetic modeling demonstrated that this ethylidene mechanism dominates over the alkyl and alkenyl mechanisms, and that it can reproduce key features of the experimental data. Specifically, the model reproduces the qualitatively correct ratios of methane, ethylene, and propene products. It also correctly reproduces and explains major features from the multiple TPD experiments that co-adsorbed methylene with various other potential reaction intermediates. All of this data suggests that the ethylidene mechanism uncovered by the DFT calculations and microkinetic model described here provides a viable interpretation for the Fischer-Tropsch chemistry observed in the Shen and Zaera experiments.

Finally, we compared our model predictions for Fischer-Tropsch synthesis on V(100) with other DFT predictions on the surfaces of traditional Fischer-Tropsch catalyst surfaces such as cobalt, iron and ruthenium.[35,38,68,69,71,74–76,142] While more study is needed before conclusions can be drawn regarding the cobalt and ruthenium surfaces, the ethylidene mechanism appears to be viable on iron surfaces. The similarity of the predicted mechanisms on iron and vanadium suggest that the Shen and Zaera experiments on vanadium may indeed provide useful experimental

insights into iron-catalyzed Fischer-Tropsch synthesis.

Future research should focus on (1) designing co-adsorption and/or isotopic substitution TPD experiments to help discriminate between the alkenyl and ethylidene mechanisms on V(100) and (2) further theoretical (and perhaps experimental surface science) efforts to examine the transferability of this chemistry to catalysts such as cobalt or ruthenium.

Reference

[1] *BP Statistical Review of World Energy 2013*; 2013.

[2] Petrus, L.; Noordermeer, M. A. *Green Chem.* **2006**, *8*, 861–867.

[3] Bayer, A. *Chem. Ing. Tech.* **1992**, *64*, year.

[4] *Opinion of the EEA Scientific Committee on Greenhouse Gas Accounting in Relation to Bioenergy*; European Enviroment Agency's Scientific Committee, 2013.

[5] *EU Renewable Energy*; European Commission, 2013.

[6] Bergius, F. *Zeitschrift Des Vereines Deutscher* **1925**, *69*, 1313–1320.

[7] Maynard, E. In *Transforming the Global Biosphere*; Watchmaker Publishing, 2003.

[8] Chase, M. In *NIST-JANAF Themochemical Tables,Fourth Edition*; J. Phys. Chem. Ref. Data, 1998; Vol. 9, pp 1–1951.

[9] Tullo, A. H.; Tremblay, J.-F. *Chem. Eng. News* **2008**, *86*, 15–22.

[10] Tullo, A. *Chem. Eng. News* **2003**, 18.

[11] Chiusoli, G. P.; Maitlis, P. M. *Metal-catalysis in Industrial Organic Processes*; Royal Society of Chemistry, 2008.

[12] Klier, K. *Adv. Catal.* **1982**, *31*, 243–313.

[13] Sabatier, P.; Senderens, J. *Compt. Rend.* **1902**, *134*, 514–516.

[14] Fischer, F.; Tropsch, H. *Ber. Dtsch. Chem. Ges. A* **1926**, *830–831*, 59.

[15] Fischer, F.; Tropsch, H. *Brennst. Chem.* **1926**, *97–104*, 7.

[16] Proskurowski, G.; Lilley, M. D.; Seewald, J. S.; Früh-Green, G. L.; Olson, E. J.; Lupton, J. E.; Sylva, S. P.; Kelley, D. S. *Science* **2008**, *319*, 604–607.

[17] McCollom, T. M.; Ritter, G.; Simoneit, B. R. *Origins Life Evol. B.* **1999**, *29*, 153–166.

[18] Sanchez-Escribano, V.; Vargas, L.; Finocchio, E.; Busca, G. *Appl. Catal. A-Gen.* **2007**, *316*, 68–74.

[19] Zaera, F. *J. Mol. Catal.* **1994**, *86*, 221–242.

[20] Schulz, H.; Claeys, M. *Appl. Catal. A-Gen.* **1999**, *186*, 71–90.

[21] Leckel, D. *Energ. Fuel.* **2009**, *23*, 2342–2358.

[22] Jacoby, M. *Chem. Eng. News* **2008**, *86*, 36–37.

[23] Maitlis, P. M.; Zanotti, V. *Chem. Commun.* **2009**, 1619–1634.

[24] Temkin, O. N.; Zeigarnik, A. V.; Kuz, A. E.; Bruk, L. G.; Slivinskii, E. V. *Russ. Chem. B+* **2002**, *51*, 1–36.

[25] Frennet, A.; Hubert, C. *J. Mol. Catal. A: Chem.* **2000**, *163*, 163–188.

[26] Wojciechowski, B. *Catal. Rev.* **1988**, *30*, 629–702.

[27] Ugo, R. *Catal. Rev.* **1975**, *11*, 225–297.

[28] Muetterties, E.; Stein, J. *Chem. Rev.* **1979**, *79*, 479–490.

[29] Zaera, F. *Chem. Rev.* **1995**, *95*, 2651–2693.

[30] Somorjai, G. *Introduction to Surface Science and Catalysis*, 1994.

[31] Kolasinski, K. W. In *Surface science: foundations of catalysis and nanoscience, third edition*; Wiley Online Library, 2004; Chapter Chemisorption, physisorption and dynamics, pp 115–183.

[32] Greeley, J.; Nørskov, J. K.; Mavrikakis, M. *Ann. Rev. Phys. Chem.* **2002**, *53*, 319–348.

[33] Honkala, K.; Hellman, A.; I. N. Remediakis, e. *Science* **2005**, *307*, 555–558.

[34] Hellman, A.; Baerends, E. J. *J. Phys. Chem. B* **2006**, *110*, 17719–17735.

[35] Ciobıcă, I.; Kramer, G. J.; Ge, Q.; Neurock, M.; Van Santen, R. *J. Catal.* **2002**, *212*, 136–144.

[36] Yang, H.; Whitten, J. L. *Langmuir* **1995**, *11*, 853–859.

[37] Yang, H. *Surf. Sci.* **1995**, *343*, 61–70.

[38] Lo, J. M.; Ziegler, T. *J. Phys. Chem. C* **2007**, *111*, 13149–13162.

[39] Gong, X.; Raval, R.; Hu, P. *J. Chem. Phys.* **2005**, *122*, 024711.

[40] Ge, Q.; Neurock, M. *J. Phys. Chem. B* **2006**, *110*, 15368–15380.

[41] Liu, Z.; Hu, P. *J. Am. Chem. Soc.* **2002**, *124*, 11568–11569.

[42] Cheng, J.; Song, T.; Hu, P.; Lok, C. M.; Ellis, P.; French, S. *J. Catal.* **2008**, *255*, 20–28.

[43] Inderwildi, O. R.; Jenkins, S. J.; King, D. A. *J. Phys. Chem. C* **2008**, *112*, 1305–1307.

[44] Huang, D.-M.; Cao, D.-B.; Li, Y.-W.; Jiao, H. *J. Phys. Chem. B* **2006**, *110*, 13920–13925.

[45] Huo, C.-F.; Li, Y.-W.; Wang, J.; Jiao, H. *J. Phys. Chem. C* **2008**, *112*, 3840–3848.

[46] Lo, J. M.; Ziegler, T. *J. Phys. Chem. C* **2008**, *112*, 3679–3691.

[47] Cheng, J.; Hu, P.; Ellis, P.; French, S.; Kelly, G.; Lok, C. M. *J. Phys. Chem. C* **2008**, *112*, 6082–6086.

[48] Cheng, J.; Gong, X.-Q.; Hu, P.; Lok, C. M.; Ellis, P.; French, S. *J. Catal.* **2008**, *254*, 285–295.

[49] Crawford, P.; Hu, P. *J. Phys. Chem. B* **2006**, *110*, 24929–24935.

[50] Gong, X.-Q.; Raval, R.; Hu, P. *Surf. Sci.* **2004**, *562*, 247–256.

[51] Liao, X.-Y.; Cao, D.-B.; Wang, S.-G.; Ma, Z.-Y.; Li, Y.-W.; Wang, J.; Jiao, H. *J. Mol. Catal. A: Chem.* **2007**, *269*, 169–178.

[52] Lo, J. M.; Ziegler, T. *J. Phys. Chem. C* **2007**, *111*, 11012–11025.

[53] Yang, T.; Wen, X.-D.; Huo, C.-F.; Li, Y.-W.; Wang, J.; Jiao, H. *J. Phys. Chem. C* **2008**, *112*, 6372–6379.

[54] Turner, M. L.; Marsih, N.; Mann, B. E.; Quyoum, R.; Long, H. C.; Maitlis, P. M. *J. Am. Chem. Soc.* **2002**, *124*, 10456–10472.

[55] Vannice, M.; Garten, R. *J. Catal.* **1979**, *56*, 236–248.

[56] Kaminsky, M. P.; N. Winograd, e. *J. Am. Chem. Soc.* **1986**, *108*, 1315–1316.

[57] Craxford, S.; Rideal, E. K. *J. Chem. Soc.* **1939**, 1604–1614.

[58] Craxford, S. *Trans. Faraday Soc.* **1946**, *42*, 576–580.

[59] Biloen, P.; Sachtler, W. *Adv. Catal.* **1981**, *30*, 165–216.

[60] Brady, R. *J. Am. Chem. Soc* **1980**, *102*, 6181–6182.

[61] Biloen, P.; Helle, J.; Sachtler, W. M. *J. Catal.* **1979**, *58*, 95–107.

[62] Brady, R. C.; Pettit, R. *J. Am. Chem. Soc.* **1981**, *103*, 1287–1289.

[63] Turner, M. L.; Long, H. C.; Shenton, A.; Byers, P. K.; Maitlis, P. M. *Chem. Eur. J.* **1995**, *1*, 549–556.

[64] Mims, C.; McCandlish, L.; Melchior, M. *Catal. lett.* **1988**, *1*, 121–125.

[65] Krishna, K. R.; Bell, A. T. *Catal. lett.* **1992**, *14*, 305–313.

[66] Maitlis, P. M. *J. Organ. Chem.* **2004**, *689*, 4366–4374.

[67] Maitlis, P. M.; Zanotti, V. *Catal. lett.* **2008**, *122*, 80–83.

[68] Cheng, J.; Hu, P.; Ellis, P.; French, S.; Kelly, G.; Lok, C. M. *Top. Catal.* **2010**, *53*, 326–337.

[69] Cheng, J.; P. Hu, e. *J. Phys. Chem. C* **2008**, *112*, 6082–6086.

[70] Cheng, J.; Hu, P.; Ellis, P.; French, S.; Kelly, G.; Lok, C. M. *J. Catal.* **2008**, *257*, 221–228.

[71] Cheng, J.; Hu, P.; Ellis, P.; French, S.; Kelly, G.; Lok, C. M. *J. Phys. Chem. C* **2009**, *113*, 8858–8863.

[72] Cheng, J.; Hu, P. *Angew. Chem Int. Ed* **2011**, *50*, 7650–7654.

[73] Cheng, J.; Hu, P.; Ellis, P.; French, S.; Kelly, G.; Lok, C. M. *J. Phys. Chem. C* **2009**, *114*, 1085–1093.

[74] van Santen, R. A.; Ghouri, M. M.; Shetty, S.; Hensen, E. M. *Catal. Sci. Technol.* **2011**, *1*, 891–911.

[75] Markvoort, A. J.; van Santen, R. A. *Angew. Chem Int. Ed* **2012**, *51*, 9015–9019.

[76] Lo, J. M.; Ziegler, T. *J. Phys. Chem. C* **2008**, *112*, 13681–13691.

[77] Shen, M.; Zaera, F. *Angew. Chem. Int. Ed.* **2008**, *47*, 6583–6585.

[78] Cheng, J.; P. Hu, e. *Top. Catal.* **2010**, *53*, 326–337.

[79] Cheng, J.; P. Hu, e. *J. Catal.* **2008**, *257*, 221–228.

[80] Ciobica, I. M.; G. J. Kramer, e. *J. Catal.* **2002**, *212*, 136–144.

[81] Lo, J. M. H.; Ziegler, T. *J. Phys. Chem. C.* **2008**, *112*, 3667–3678.

[82] Lo, J. M.; Ziegler, T. *J. Phys. Chem. C* **2008**, *112*, 13642–13649.

[83] Lo, J. M. H.; Ziegler, T. *J. Phys. Chem. C.* **2008**, *112*, 13681–13691.

[84] Dacapo v2.7.7, https://wiki.fysik.dtu.dk/dacapo.

[85] Hammer, B.; Norskov, J. K. *Phys. Rev. B.* **1999**, *59*, 7413–7421.

[86] Bahn, S. R.; Jacobsen, K. W. *Comput. Sci. Eng.* **2002**, *4*, 56–66.

[87] Bihlmayer, G.; Asada, T.; Blügel, S. *Phys. Rev. B* **2000**, *62*, R11937–R11940.

[88] Batyrev, I. G.; Cho, J. H.; Kleinman, L. *Phys. Rev. B.* **2001**, *63*, 172420.

[89] Kresse, W. P. R., G.; Bergermayer *Phys. Rev. B.* **2002**, *66*, 146401.

[90] Lacina, D.; Yang, J.; Erskine, J. *Phys. Rev. B* **2007**, *75*, 195423.

[91] Perdew, J. P.; Chevary, J. A.; Vosko, S. H.; Jackson, K. A.; Pederson, M. R.; Singh, D. J.; Fiolhais, C. *Phys. Rev. B* **1992**, *46*, 6671–6687.

[92] K. Burke, Y. W., J. P. Perdew In *Electronic Density Functional Theory: Recent Progress and New Directions*; J. F. Dobson, G. V., Das, M. P., Eds.; Plenum, 1998; pp 81–112.

[93] Hammer, B.; Hansen, L. B.; Norskov, J. K. *Phys. Rev. B.* **1999**, *59*, 7413–7421.

[94] Vanderbilt, D. H. *Phys. Rev. B.* **1990**, *41*, 7892–7895.

[95] Vasyutinskiy, B. M.; Kartmazov, G. N.; Smirnov, Y. M.; Finkel, V. A. *Phys. Met. Metall.* **1966**, *21*, 134.

[96] Jonsson, H.; Mills, G.; Jacobsen, K. W. In *Classical and Quantum Dynamics in Condensed Phase Simulations*; Berne, B. J., Ciccotti, G., Coker, D. F., Eds.; World Scientific: Singapore, 1998; Chapter 'Nudged elastic band method for finding minimum energy paths of transitions', pp 385–404.

[97] Mills, G.; Jonsson, H. *Phys. Rev. Lett.* **1994**, *72*, 1124–1127.

[98] Mills, G.; Jonsson, H.; Schenter, G. K. *Surf. Sci.* **1995**, *324*, 305–337.

[99] Jensen, F. In *Introduction to Computational Chemistry*; John Wiely & Sons: Chichester, 2007; Chapter 'Statistical mechanics and transitional state theory', pp 429–434.

[100] Blaylock, D. W.; Ogura, T.; Green, W. H.; Beran, G. J. *J. Phys. Chem. C* **2009**, *113*, 4898–4908.

[101] Somorjai, G. In *Introduction to Surface Chemistry and Catalysis*; Wiley-Interscience: New York, 1993; Chapter 'Dynamics at surfaces', pp 319–361.

[102] Shen, M. Ph.D. thesis, University of California, Riverside, 2007.

[103] Zaera, F. *Acc. Chem. Res.* **1992**, *25*, 260–265.

[104] Jensen, V.; Andersen, J.; Nielsen, H.; Adams, D. *Surf. Sci.* **1981**, *112*, L785–L789.

[105] Koller, R.; Bergermayer, W.; Kresse, G.; Hebenstreit, E.; Konvicka, C.; Schmid, M.; Podloucky, R.; Varga, P. *Surf. Sci.* **2001**, *480*, 11–24.

[106] Kralj, M.; Pervan, P.; Milun, M.; Wandelt, K.; Mandrino, D.; Jenko, M. *Surf. Sci.* **2003**, *526*, 166–176.

[107] Shen, M.; Ma, Q.; Lee, I.; Zaera, F. *J. Phys. Chem. C* **2007**, *111*, 6033–6040.

[108] Wilson, J.; Guo, H.; Morales, R.; Podgornov, E.; Lee, I.; Zaera, F. *Phys. Chem. Chem. Phys.* **2007**, *9*, 3830–3852.

[109] Registry of Mass Spectral Data, Volume I, Edited by Einan Stenhagen, Sixten Abrahamson, and Fred W. McLafferty, Wiley-Interscience, New York, 1974.

[110] Hammer, B.; Norskov, J. K. *Adv. Catal.* **2000**, *45*, 71–129.

[111] Jones, R. O.; Gunnarsson, O. *Rev. Mod. Phys.* **1989**, *61*, 689–746.

[112] Perdew, J. P.; Burke, K.; Ernzerhof, M. *Phys. Rev. Lett.* **1996**, *77*, 3865–3868.

[113] Zhang, Y.; Yang, W. *Phys. Rev. Lett.* **1998**, *80*, 890–890.

[114] Zhao, Y.; González-García, N.; Truhlar, D. G. *J. Phys. Chem. A* **2005**, *109*, 2012–2018.

[115] Lynch, B. J.; Truhlar, D. G. *J. Phys. Chem. A* **2001**, *105*, 2936–2941.

[116] Cohen, A. J.; Mori-Sánchez, P.; Yang, W. *Science* **2008**, *321*, 792–794.

[117] Quintal, M. M.; Karton, A.; Iron, M. A.; Boese, A. D.; Martin, J. M. *J. Phys. Chem. A* **2006**, *110*, 709–716.

[118] de Jong, G. T.; Geerke, D. P.; Diefenbach, A.; Matthias Bickelhaupt, F. *Chem. Phys.* **2005**, *313*, 261–270.

[119] Siegbahn, P. E. *J. Bio. Inorg. Chem.* **2006**, *11*, 695–701.

[120] Sakong, S.; Groß, A. *J. Catal.* **2005**, *231*, 420–429.

[121] Kratzer, P.; Hammer, B.; No, J. et al.Kratzer, P and Hammer, Bjørk and No, JK and others *J. Chem. Phys.* **1996**, *105*, 5595–5604.

[122] Abbott, H.; Bukoski, A.; Kavulak, D.; Harrison, I. *J. Chem. Phys.* **2003**, *119*, 6407–6410.

[123] Pallassana, V.; Neurock, M.; Lusvardi, V. S.; Lerou, J. J.; Kragten, D. D.; van Santen, R. A. *J. Phys. Chem. B* **2002**, *106*, 1656–1669.

[124] Stuve, E.; Madix, R. *J. Phys. Chem.* **1985**, *89*, 3183–3185.

[125] Rostrup-Nielsen, J. R.; Sehested, J.; Nørskov, J. K. *Adv. Catal.* **2002**, *47*, 65–139.

[126] Zaera, F. *Acc. Chem. Res.* **2002**, *35*, 129–136.

[127] Shen, M.; Zaera, F. *J. Phys. Chem. C* **2007**, *111*, 13570–13578.

[128] Redhead, P. *Vacuum* **1963**, *12*, 203–211.

[129] Barteau, M.; Broughton, J.; Menzel, D. *App. Surf. Sci.* **1984**, *19*, 92–115.

[130] Steinbach, F.; Kiss, J.; Krall, R. *Surf. Sci.* **1985**, *157*, 401–412.

[131] Wu, M. C.; Goodman, D. W. *J. Am. Chem. Soc.* **1994**, *116*, 1364–1371.

[132] Zhou, X.-L.; Liu, Z.-M.; Kiss, J.; Sloan, D.; White, J. *J. Am. Chem. Soc.* **1995**, *117*, 3565–3592.

[133] Maitlis, P. M.; Zanotti, V. *Catal. lett.* **2008**, *122*, 80–83.

[134] Maitlis, P. M.; Zanotti, V. *Chem. Commun.* **2009**, 1619–1634.

[135] Bent, B. E. *Chem. Rev.* **1996**, *96*, 1361–1390.

[136] Guo, H.; Zaera, F. *Surf. Sci.* **2003**, *547*, 284–298.

[137] Shao, Y. et al. *Phys. Chem. Chem. Phys.* **2006**, *8*, 3172–3191.

[138] Centi, F. *Catal. Tod.* **1993**, *16*, 5–26.

[139] Hucknall, D. J. In *Selective Oxidation of Hydrocarbons*; Academic Press: New York, 1974.

[140] A. Bielanski, J. H. In *Oxygen in Catalysis*; CRC Press: New York, 1991.

[141] Khodakov A. Y., F. P., Chu W. *Chem. Rev.* **2007**, *107*, 1692–1744.

[142] Storsæter, D. C. A. H., Sølvi *Surf. Sci.* **2006**, *600*, 2051–2063.

Appendix A

Matlab code structure of microkinetic model

Matlab code was developed to integrate the microkinetic model equations to simulate the surface reactions and gaseous product desorption occurring in the TPD experiments. The Matlab code structure is illustrated in Figure A.1.

In TPD experiments, the sample gas is initially dosed on to the single-crystal metal surface at low temperature ($T_{initial}$). Then the system is heated at a constant rate β (that is $\Delta T/\Delta t$), stimulating surface reactions and gaseous product desorption. Although the temperature rises continuously in the experiments, for simplicity we model the heating as a set of short, constant-temperature intervals ΔT (e.g. $\Delta T = 1.0$ K, $\Delta t = 100$ s; or $\Delta T = 0.1$ K, $\Delta t = 10$ s for a smoother simulated TPD curve), and with the temperature changing in discrete steps between each interval. This allows one to compute a set of fixed rate and equilibrium constants for the current temperature:

$$K_c(T) = e^{-\Delta G_{rxn}(T)/RT} \tag{A.1}$$

Figure A.1: Matlab code structure of microkinetic model. (1) The initial concentration $\theta_{i,0}$ for each species involved is set. If it is not the initial temperature, the initial concentrations of species are assumed to be the final concentrations of the last heating step ($T-\Delta T$). (2) The rate constants are updated with the increasing temperatures. (3) The differential equations with variables of all species concentrations are solved for a certain heating step. The same procedures from (1) to (3) are repeated to simulate the next heating step until the final temperature.

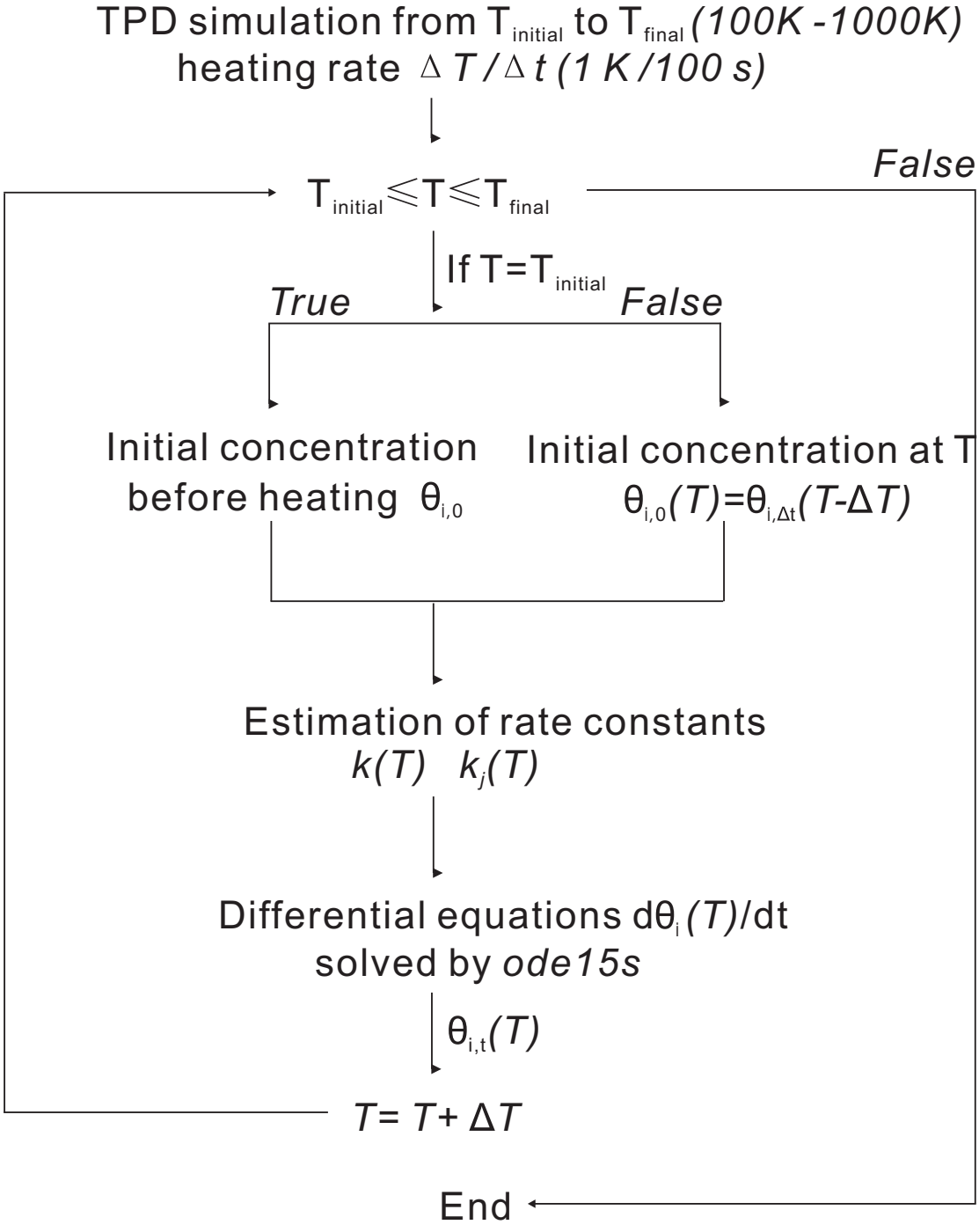

$$k_{for}(T) = \frac{k_B T}{h} e^{-\Delta G_{act}(T)/RT} \tag{A.2}$$

$$k_{rev}(T) = \frac{k_{for}(T)}{K_c(T)} \tag{A.3}$$

where $K_c(T)$ is the equilibrium constant, $k_{for}(T)$ is the forward reaction rate constant, $k_{rev}(T)$ is the reverse reaction rate constant, $\Delta G_{rxn}(T)$ is the reaction free energy, and $\Delta G_{act}(T)$ is the free energy of activation calculated by DFT method. As stated previously, the temperature variation of ΔH and ΔS was ignored when computing $\Delta G(T)$.

The reaction flux for any elementary step j at the certain temperature T can be expressed as:

$$reaction\ flux_j = k_{for,j} \prod_{l=1}^{S_{\mathrm{R}}} \theta_l^{-\nu_{j,l}} - k_{rev,j} \prod_{l=1}^{S_{\mathrm{P}}} \theta_l^{\nu_{j,l}} \tag{A.4}$$

where $\nu_{j,l}$ is the stoichiometric coefficient of species i in reaction j; $k_{for,j}$ and $k_{rev,j}$ are the rate constants for the forward and reverse reaction j that are estimated by thermochemistry data; θ represents the variable of species surface coverage. The rate constants are updated with the increasing temperatures.

In the heating interval at the certain temperature, linking all the elementary steps that species i involved, a complete set of time-dependent ordinary differential equations with variables of all species concentrations (or surface coverages θ_i) is built:

$$\frac{\mathrm{d}\theta_i}{\mathrm{d}t} = \sum_{j=1}^{\text{no.rxns}} \nu_{j,i} [k_{for,j} \prod_{l=1}^{S_{\mathrm{R}}} \theta_l^{-\nu_{j,l}} - k_{rev,j} \prod_{l=1}^{S_{\mathrm{P}}} \theta_l^{\nu_{j,l}}] \tag{A.5}$$

It is solved using the stiff ordinary differential equation solver (`ode15s` in Matlab), time stepping to steady state for a specified reaction time (Δt). All species concentrations could be mapped at this heating step. And the final distributions of the

species at this moment provides the initial conditions in next heating step. Such cycles of differential equations and heating are repeated until the final temperature (T_{final}) is reached.

Appendix B

Differential equation set to simulate methane formation

For the simulations of methane formation with isotopic labeling (Chapter 3), twenty-eight gaseous and surface species and thirty-five reactions are included in the model, as shown in Table 3.2.

The elementary reaction steps are listed below, where 'V' refers to a vacant surface site, species with 'gas' in the name are gaseous, and all others are surface species. For jth elementary reaction step, k_j and ki_j correspond to the forward and reverse reactant rate constants, respectively.

1. CH3 + H $\longrightarrow$ CH4gas + 2V
2. CH3 + D $\longrightarrow$ CH3Dgas + 2V
3. CH2D + H $\longrightarrow$ CH3Dgas + 2V
4. CH2D + D $\longrightarrow$ CH2D2gas + 2V
5. CHD2 + H $\longrightarrow$ CH2D2gas + 2V
6. CHD2 + D $\longrightarrow$ CHD3gas + 2V

7. CD3 + H $\longrightarrow$ CHD3gas + 2V

8. CD3 + D $\longrightarrow$ CD4gas + 2V

9. H + H $\longrightarrow$ H2gas + 2V

10. H + D $\longrightarrow$ HDgas + 2V

11. D + D $\longrightarrow$ D2gas + 2V

12. C + H $\longrightarrow$ CH + V

13. C + D $\longrightarrow$ CD + V

14. CH + H $\longrightarrow$ CH2 + V

15. CH + D $\longrightarrow$ CHD + V

16. CD + H $\longrightarrow$ CHD + V

17. CD + D $\longrightarrow$ CD2 + V

18. CH2 + H $\longrightarrow$ CH3 + V

19. CH2 + D $\longrightarrow$ CH2D + V

20. CHD + H $\longrightarrow$ CH2D + V

21. CHD + D $\longrightarrow$ CHD2 + V

22. CD2 + H $\longrightarrow$ CHD2 + V

23. CD2 + D $\longrightarrow$ CD3 + V

24. CH2 + H $\longrightarrow$ CH3_4f + V

25. CH2 + D $\longrightarrow$ CH2D_4f + V

26. CHD + H $\longrightarrow$ CH2D_4f + V

27. CHD + D $\longrightarrow$ CHD2_4f + V

28. CD2 + H $\longrightarrow$ CHD2_4f + V

29. CD2 + D $\longrightarrow$ CD3_4f + V

30. CH3_4f + V $\longrightarrow$ CH3 + V

31. CH2D_4f + V $\longrightarrow$ CH2D + V

32. CHD2_4f + V $\longrightarrow$ CHD2 + V

33. CD3_4f + V $\longrightarrow$ CD3 + V

34. OH + V $\longrightarrow$ Oxy + H

35. H2O + V $\longrightarrow$ OH + H

The differential equations are listed below, where θ_i represents the surface coverage of species i:

$\frac{\mathrm{d}\theta_{H2gas}}{\mathrm{d}t} = +k9 * \theta_H * \theta_H - ki9 * \theta_{H2gas} * \theta_V * \theta_V;$

$\frac{\mathrm{d}\theta_{HDgas}}{\mathrm{d}t} = +k10 * \theta_H * \theta_D - ki10 * \theta_{HDgas} * \theta_V * \theta_V;$

$\frac{\mathrm{d}\theta_{D2gas}}{\mathrm{d}t} = +k11 * \theta_D * \theta_D - ki11 * \theta_{D2gas} * \theta_V * \theta_V;$

$\frac{\mathrm{d}\theta_{CH4gas}}{\mathrm{d}t} = +k1 * \theta_{CH3} * \theta_H - ki1 * \theta_{CH4gas} * \theta_V * \theta_V;$

$\frac{\mathrm{d}\theta_{CH3Dgas}}{\mathrm{d}t} = +k2 * \theta_{CH3} * \theta_D - ki2 * \theta_{CH3Dgas} * \theta_V * \theta_V + k3 * \theta_{CH2D} * \theta_H - ki3 * \theta_{CH3Dgas} * \theta_V * \theta_V;$

$\frac{\mathrm{d}\theta_{CH2D2gas}}{\mathrm{d}t} = +k4 * \theta_{CH2D} * \theta_D - ki4 * \theta_{CH2D2gas} * \theta_V * \theta_V + k5 * \theta_{CHD2} * \theta_H - ki5 * \theta_{CH2D2gas} * \theta_V * \theta_V;$

$\frac{\mathrm{d}\theta_{CHD3gas}}{\mathrm{d}t} = +k6 * \theta_{CHD2} * \theta_D - ki6 * \theta_{CHD3gas} * \theta_V * \theta_V + k7 * \theta_{CD3} * \theta_H - ki7 * \theta_{CHD3gas} * \theta_V * \theta_V;$

$\frac{\mathrm{d}\theta_{CD4gas}}{\mathrm{d}t} = +k8 * \theta_{CD3} * \theta_D - ki8 * \theta_{CD4gas} * \theta_V * \theta_V;$

$\frac{\mathrm{d}\theta_C}{\mathrm{d}t} = -k12 * \theta_C * \theta_H + ki12 * \theta_{CH} * \theta_V - k13 * \theta_C * \theta_D + ki13 * \theta_{CD} * \theta_V;$

$$\frac{\mathrm{d}\theta_{CH}}{\mathrm{d}t} = +k12 * \theta_C * \theta_H - ki12 * \theta_{CH} * \theta_V - k14 * \theta_{CH} * \theta_H + ki14 * \theta_{CH2} * \theta_V - k15 * \theta_{CH} * \theta_D + ki15 * \theta_{CHD} * \theta_V;$$

$$\frac{\mathrm{d}\theta_{CD}}{\mathrm{d}t} = +k13 * \theta_C * \theta_D - ki13 * \theta_{CD} * \theta_V - k16 * \theta_{CD} * \theta_H + ki16 * \theta_{CHD} * \theta_V - k17 * \theta_{CD} * \theta_D + ki17 * \theta_{CD2} * \theta_V;$$

$$\frac{\mathrm{d}\theta_{CH2}}{\mathrm{d}t} = +k14 * \theta_{CH} * \theta_H - ki14 * \theta_{CH2} * \theta_V - k18 * \theta_{CH2} * \theta_H + ki18 * \theta_{CH3} * \theta_V - k19 * \theta_{CH2} * \theta_D + ki19 * \theta_{CH2D} * \theta_V - k24 * \theta_{CH2} * \theta_H + ki24 * \theta_{CH3\_4f} * \theta_V - k25 * \theta_{CH2} * \theta_D + ki25 * \theta_{CH2D\_4f} * \theta_V;$$

$$\frac{\mathrm{d}\theta_{CHD}}{\mathrm{d}t} = +k15 * \theta_{CH} * \theta_D - ki15 * \theta_{CHD} * \theta_V + k16 * \theta_{CD} * \theta_H - ki16 * \theta_{CHD} * \theta_V - k20 * \theta_{CHD} * \theta_H + ki20 * \theta_{CH2D} * \theta_V - k21 * \theta_{CHD} * \theta_D + ki21 * \theta_{CHD2} * \theta_V - k26 * \theta_{CHD} * \theta_H + ki26 * \theta_{CH2D\_4f} * \theta_V - k27 * \theta_{CHD} * \theta_D + ki27 * \theta_{CHD2\_4f} * \theta_V;$$

$$\frac{\mathrm{d}\theta_{CD2}}{\mathrm{d}t} = +k17 * \theta_{CD} * \theta_D - ki17 * \theta_{CD2} * \theta_V - k22 * \theta_{CD2} * \theta_H + ki22 * \theta_{CHD2} * \theta_V - k23 * \theta_{CD2} * \theta_D + ki23 * \theta_{CD3} * \theta_V - k28 * \theta_{CD2} * \theta_H + ki28 * \theta_{CHD2\_4f} * \theta_V - k29 * \theta_{CD2} * \theta_D + ki29 * \theta_{CD3\_4f} * \theta_V;$$

$$\frac{\mathrm{d}\theta_{CH3}}{\mathrm{d}t} = -k1 * \theta_{CH3} * \theta_H + ki1 * \theta_{CH4gas} * \theta_V * \theta_V - k2 * \theta_{CH3} * \theta_D + ki2 * \theta_{CH3Dgas} * \theta_V * \theta_V + k18 * \theta_{CH2} * \theta_H - ki18 * \theta_{CH3} * \theta_V + k30 * \theta_{CH3\_4f} * \theta_V - ki30 * \theta_{CH3} * \theta_V;$$

$$\frac{\mathrm{d}\theta_{CH2D}}{\mathrm{d}t} = -k3 * \theta_{CH2D} * \theta_H + ki3 * \theta_{CH3Dgas} * \theta_V * \theta_V - k4 * \theta_{CH2D} * \theta_D + ki4 * \theta_{CH2D2gas} * \theta_V * \theta_V + k19 * \theta_{CH2} * \theta_D - ki19 * \theta_{CH2D} * \theta_V + k20 * \theta_{CHD} * \theta_H - ki20 * \theta_{CH2D} * \theta_V + k31 * \theta_{CH2D\_4f} * \theta_V - ki31 * \theta_{CH2D} * \theta_V;$$

$$\frac{\mathrm{d}\theta_{CHD2}}{\mathrm{d}t} = -k5 * \theta_{CHD2} * \theta_H + ki5 * \theta_{CH2D2gas} * \theta_V * \theta_V - k6 * \theta_{CHD2} * \theta_D + ki6 * \theta_{CHD3gas} * \theta_V * \theta_V + k21 * \theta_{CHD} * \theta_D - ki21 * \theta_{CHD2} * \theta_V + k22 * \theta_{CD2} * \theta_H - ki22 *$$

$\theta_{CHD2} * \theta_V + k32 * \theta_{CHD2\_4f} * \theta_V - ki32 * \theta_{CHD2} * \theta_V;$

$\frac{\mathrm{d}\theta_{CD3}}{\mathrm{d}t} = -k7 * \theta_{CD3} * \theta_H + ki7 * \theta_{CHD3gas} * \theta_V * \theta_V - k8 * \theta_{CD3} * \theta_D + ki8 * \theta_{CD4gas} *$
$\theta_V * \theta_V + k23 * \theta_{CD2} * \theta_D - ki23 * \theta_{CD3} * \theta_V + k33 * \theta_{CD3\_4f} * \theta_V - ki33 * \theta_{CD3} * \theta_V;$

$\frac{\mathrm{d}\theta_{CH3\_4f}}{\mathrm{d}t} = +k24 * \theta_{CH2} * \theta_H - ki24 * \theta_{CH3\_4f} * \theta_V - k30 * \theta_{CH3\_4f} * \theta_V + ki30 * \theta_{CH3} * \theta_V;$

$\frac{\mathrm{d}\theta_{CH2D\_4f}}{\mathrm{d}t} = +k25 * \theta_{CH2} * \theta_D - ki25 * \theta_{CH2D\_4f} * \theta_V + k26 * \theta_{CHD} * \theta_H - ki26 *$
$\theta_{CH2D\_4f} * \theta_V - k31 * \theta_{CH2D\_4f} * \theta_V + ki31 * \theta_{CH2D} * \theta_V;$

$\frac{\mathrm{d}\theta_{CHD2\_4f}}{\mathrm{d}t} = +k27 * \theta_{CHD} * \theta_D - ki27 * \theta_{CHD2\_4f} * \theta_V + k28 * \theta_{CD2} * \theta_H - ki28 *$
$\theta_{CHD2\_4f} * \theta_V - k32 * \theta_{CHD2\_4f} * \theta_V + ki32 * \theta_{CHD2} * \theta_V;$

$\frac{\mathrm{d}\theta_{CD3\_4f}}{\mathrm{d}t} = +k29 * \theta_{CD2} * \theta_D - ki29 * \theta_{CD3\_4f} * \theta_V - k33 * \theta_{CD3\_4f} * \theta_V + ki33 * \theta_{CD3} * \theta_V;$

$\frac{\mathrm{d}\theta_V}{\mathrm{d}t} = +2 * k1 * \theta_{CH3} * \theta_H - 2 * ki1 * \theta_{CH4gas} * \theta_V * \theta_V + 2 * k2 * \theta_{CH3} * \theta_D - 2 * ki2 *$
$\theta_{CH3Dgas} * \theta_V * \theta_V + 2 * k3 * \theta_{CH2D} * \theta_H - 2 * ki3 * \theta_{CH3Dgas} * \theta_V * \theta_V + 2 * k4 * \theta_{CH2D} * \theta_D -$
$2 * ki4 * \theta_{CH2D2gas} * \theta_V * \theta_V + 2 * k5 * \theta_{CHD2} * \theta_H - 2 * ki5 * \theta_{CH2D2gas} * \theta_V * \theta_V + 2 * k6 *$
$\theta_{CHD2} * \theta_D - 2 * ki6 * \theta_{CHD3gas} * \theta_V * \theta_V + 2 * k7 * \theta_{CD3} * \theta_H - 2 * ki7 * \theta_{CHD3gas} * \theta_V * \theta_V +$
$2 * k8 * \theta_{CD3} * \theta_D - 2 * ki8 * \theta_{CD4gas} * \theta_V * \theta_V + 2 * k9 * \theta_H * \theta_H - 2 * ki9 * \theta_{H2gas} * \theta_V * \theta_V +$
$2 * k10 * \theta_H * \theta_D - 2 * ki10 * \theta_{HDgas} * \theta_V * \theta_V + 2 * k11 * \theta_D * \theta_D - 2 * ki11 * \theta_{D2gas} * \theta_V * \theta_V +$
$k12 * \theta_C * \theta_H - ki12 * \theta_{CH} * \theta_V + k13 * \theta_C * \theta_D - ki13 * \theta_{CD} * \theta_V + k14 * \theta_{CH} * \theta_H - ki14 *$
$\theta_{CH2} * \theta_V + k15 * \theta_{CH} * \theta_D - ki15 * \theta_{CHD} * \theta_V + k16 * \theta_{CD} * \theta_H - ki16 * \theta_{CHD} * \theta_V + k17 *$
$\theta_{CD} * \theta_D - ki17 * \theta_{CD2} * \theta_V + k18 * \theta_{CH2} * \theta_H - ki18 * \theta_{CH3} * \theta_V + k19 * \theta_{CH2} * \theta_D - ki19 *$
$\theta_{CH2D} * \theta_V + k20 * \theta_{CHD} * \theta_H - ki20 * \theta_{CH2D} * \theta_V + k21 * \theta_{CHD} * \theta_D - ki21 * \theta_{CHD2} * \theta_V +$
$k22 * \theta_{CD2} * \theta_H - ki22 * \theta_{CHD2} * \theta_V + k23 * \theta_{CD2} * \theta_D - ki23 * \theta_{CD3} * \theta_V + k24 * \theta_{CH2} *$
$\theta_H - ki24 * \theta_{CH3\_4f} * \theta_V + k25 * \theta_{CH2} * \theta_D - ki25 * \theta_{CH2D\_4f} * \theta_V + k26 * \theta_{CHD} * \theta_H -$

$$ki26*\theta_{CH2D\_4f}*\theta_V+k27*\theta_{CHD}*\theta_D-ki27*\theta_{CHD2\_4f}*\theta_V+k28*\theta_{CD2}*\theta_H-ki28*\theta_{CHD2\_4f}*\theta_V+k29*\theta_{CD2}*\theta_D-ki29*\theta_{CD3\_4f}*\theta_V-k30*\theta_{CH3\_4f}*\theta_V+ki30*\theta_{CH3}*\theta_V+k30*\theta_{CH3\_4f}*\theta_V-ki30*\theta_{CH3}*\theta_V-k31*\theta_{CH2D\_4f}*\theta_V+ki31*\theta_{CH2D}*\theta_V+k31*\theta_{CH2D\_4f}*\theta_V-ki31*\theta_{CH2D}*\theta_V-k32*\theta_{CHD2\_4f}*\theta_V+ki32*\theta_{CHD2}*\theta_V+k32*\theta_{CHD2\_4f}*\theta_V-ki32*\theta_{CHD2}*\theta_V-k33*\theta_{CD3\_4f}*\theta_V+ki33*\theta_{CD3}*\theta_V+k33*\theta_{CD3\_4f}*\theta_V-ki33*\theta_{CD3}*\theta_V-k34*\theta_{OH}*\theta_V+ki34*\theta_{Oxy}*\theta_H-k35*\theta_{H2O}*\theta_V+ki35*\theta_{OH}*\theta_H;$$

$$\frac{\mathrm{d}\theta_H}{\mathrm{d}t}=-k1*\theta_{CH3}*\theta_H+ki1*\theta_{CH4gas}*\theta_V*\theta_V-k3*\theta_{CH2D}*\theta_H+ki3*\theta_{CH3Dgas}*\theta_V*\theta_V-k5*\theta_{CHD2}*\theta_H+ki5*\theta_{CH2D2gas}*\theta_V*\theta_V-k7*\theta_{CD3}*\theta_H+ki7*\theta_{CHD3gas}*\theta_V*\theta_V-2*k9*\theta_H*\theta_H+2*ki9*\theta_{H2gas}*\theta_V*\theta_V-k10*\theta_H*\theta_D+ki10*\theta_{HDgas}*\theta_V*\theta_V-k12*\theta_C*\theta_H+ki12*\theta_{CH}*\theta_V-k14*\theta_{CH}*\theta_H+ki14*\theta_{CH2}*\theta_V-k16*\theta_{CD}*\theta_H+ki16*\theta_{CHD}*\theta_V-k18*\theta_{CH2}*\theta_H+ki18*\theta_{CH3}*\theta_V-k20*\theta_{CHD}*\theta_H+ki20*\theta_{CH2D}*\theta_V-k22*\theta_{CD2}*\theta_H+ki22*\theta_{CHD2}*\theta_V-k24*\theta_{CH2}*\theta_H+ki24*\theta_{CH3\_4f}*\theta_V-k26*\theta_{CHD}*\theta_H+ki26*\theta_{CH2D\_4f}*\theta_V-k28*\theta_{CD2}*\theta_H+ki28*\theta_{CHD2\_4f}*\theta_V+k34*\theta_{OH}*\theta_V-ki34*\theta_{Oxy}*\theta_H+k35*\theta_{H2O}*\theta_V-ki35*\theta_{OH}*\theta_H;$$

$$\frac{\mathrm{d}\theta_D}{\mathrm{d}t}=-k2*\theta_{CH3}*\theta_D+ki2*\theta_{CH3Dgas}*\theta_V*\theta_V-k4*\theta_{CH2D}*\theta_D+ki4*\theta_{CH2D2gas}*\theta_V*\theta_V-k6*\theta_{CHD2}*\theta_D+ki6*\theta_{CHD3gas}*\theta_V*\theta_V-k8*\theta_{CD3}*\theta_D+ki8*\theta_{CD4gas}*\theta_V*\theta_V-k10*\theta_H*\theta_D+ki10*\theta_{HDgas}*\theta_V*\theta_V-2*k11*\theta_D*\theta_D+2*ki11*\theta_{D2gas}*\theta_V*\theta_V-k13*\theta_C*\theta_D+ki13*\theta_{CD}*\theta_V-k15*\theta_{CH}*\theta_D+ki15*\theta_{CHD}*\theta_V-k17*\theta_{CD}*\theta_D+ki17*\theta_{CD2}*\theta_V-k19*\theta_{CH2}*\theta_D+ki19*\theta_{CH2D}*\theta_V-k21*\theta_{CHD}*\theta_D+ki21*\theta_{CHD2}*\theta_V-k23*\theta_{CD2}*\theta_D+ki23*\theta_{CD3}*\theta_V-k25*\theta_{CH2}*\theta_D+ki25*\theta_{CH2D\_4f}*\theta_V-k27*\theta_{CHD}*\theta_D+ki27*\theta_{CHD2\_4f}*\theta_V-k29*\theta_{CD2}*\theta_D+ki29*\theta_{CD3\_4f}*\theta_V;$$

$$\frac{\mathrm{d}\theta_{OH}}{\mathrm{d}t}=-k34*\theta_{OH}*\theta_V+ki34*\theta_{Oxy}*\theta_H+k35*\theta_{H2O}*\theta_V-ki35*\theta_{OH}*\theta_H;$$

$$\frac{\mathrm{d}\theta_{H2O}}{\mathrm{d}t} = -k35 * \theta_{H2O} * \theta_V + ki35 * \theta_{OH} * \theta_H;$$

$$\frac{\mathrm{d}\theta_{Oxy}}{\mathrm{d}t} = +k34 * \theta_{OH} * \theta_V - ki34 * \theta_{Oxy} * \theta_H;$$

Appendix C

Differential equation set to simulate propene formation

For the propene formation mechanism discussed in Chapter 4, the final microkinetic model covers twenty-four gaseous and surface species and twenty-eight reactions, as shown in Table 4.3.

The elementary reaction steps are listed below, where 'V' refers to a vacant surface site, species with 'gas' in the name are gaseous, and all others are surface species. For jth elementary reaction step, k_j and ki_j correspond to the forward and reverse reactant rate constants, respectively.

1. CH3 + H $\longrightarrow$ CH4gas + V
2. CHCH + non $\longrightarrow$ CHCHgas + V
3. CH2CH2 + non $\longrightarrow$ CH2CH2gas + V
4. CH2CHCH3 + non $\longrightarrow$ CH2CHCH3gas + V
5. H + H $\longrightarrow$ H2gas + V
6. C + H $\longrightarrow$ CH + V

7. CH + H $\longrightarrow$ CH2 + V

8. CH2 + H $\longrightarrow$ CH3 + V

9. CH2 + H $\longrightarrow$ CH3_4f + V

10. CH3_4f + V $\longrightarrow$ CH3 + V

11. CH2 + CH3 $\longrightarrow$ CH2CH3 + V

12. CH + CH2 $\longrightarrow$ CHCH2 + V

13. CH + CH3 $\longrightarrow$ CHCH3 + V

14. CHCH + H $\longrightarrow$ CHCH2 + V

15. CHCH2 + H $\longrightarrow$ CHCH3 + V

16. CHCH2 + H $\longrightarrow$ CH2CH2 + V

17. CHCH3 + H $\longrightarrow$ CH2CH3 + V

18. CH2 + CH2CH3 $\longrightarrow$ CH2CH2CH3 + V

19. CH2 + CHCH2 $\longrightarrow$ CH2CHCH2 + V

20. CH + CHCH3 $\longrightarrow$ CHCHCH3 + V

21. CH2CH2CH3 + V $\longrightarrow$ CH2CHCH3 + H

22. CH2CHCH2 + H $\longrightarrow$ CH2CHCH3 + V

23. CHCHCH3 + H $\longrightarrow$ CH2CHCH3 + V

24. CH + CH $\longrightarrow$ CHCH + V

25. CH2 + CH2 $\longrightarrow$ CH2CH2 + V

26. CHCH3 + V $\longrightarrow$ CH2CH2 + V

27. OH + V $\longrightarrow$ Oxy + H

28. H2O + V $\longrightarrow$ OH + H

The differential equations are listed below, where θ_i represents the surface

coverage of species i:

$$\frac{\mathrm{d}\theta_{CH4gas}}{\mathrm{d}t} = +k1 * \theta_{CH3} * \theta_H - ki1 * \theta_{CH4gas} * \theta_V * \theta_V;$$

$$\frac{\mathrm{d}\theta_{CHCHgas}}{\mathrm{d}t} = +k2 * \theta_{CHCH} * \theta_{non} - ki2 * \theta_{CHCHgas} * \theta_V;$$

$$\frac{\mathrm{d}\theta_{CH2CH2gas}}{\mathrm{d}t} = +k3 * \theta_{CH2CH2} * \theta_{non} - ki3 * \theta_{CH2CH2gas} * \theta_V;$$

$$\frac{\mathrm{d}\theta_{CH2CHCH3gas}}{\mathrm{d}t} = +k4 * \theta_{CH2CHCH3} * \theta_{non} - ki4 * \theta_{CH2CHCH3gas} * \theta_V;$$

$$\frac{\mathrm{d}\theta_{H2gas}}{\mathrm{d}t} = +k5 * \theta_H * \theta_H - ki5 * \theta_{H2gas} * \theta_V * \theta_V;$$

$$\frac{\mathrm{d}\theta_C}{\mathrm{d}t} = -k6 * \theta_C * \theta_H + ki6 * \theta_{CH} * \theta_V;$$

$$\frac{\mathrm{d}\theta_{CH}}{\mathrm{d}t} = +k6 * \theta_C * \theta_H - ki6 * \theta_{CH} * \theta_V - k7 * \theta_{CH} * \theta_H + ki7 * \theta_{CH2} * \theta_V - k12 * \theta_{CH} * \theta_{CH2} + ki12 * \theta_{CHCH2} * \theta_V - k13 * \theta_{CH} * \theta_{CH3} + ki13 * \theta_{CHCH3} * \theta_V - k20 * \theta_{CH} * \theta_{CHCH3} + ki20 * \theta_{CHCHCH3} * \theta_V - 2 * k24 * \theta_{CH} * \theta_{CH} + 2 * ki24 * \theta_{CHCH} * \theta_V;$$

$$\frac{\mathrm{d}\theta_{CH2}}{\mathrm{d}t} = +k7 * \theta_{CH} * \theta_H - ki7 * \theta_{CH2} * \theta_V - k8 * \theta_{CH2} * \theta_H + ki8 * \theta_{CH3} * \theta_V - k9 * \theta_{CH2} * \theta_H + ki9 * \theta_{CH3\_4f} * \theta_V - k11 * \theta_{CH2} * \theta_{CH3} + ki11 * \theta_{CH2CH3} * \theta_V - k12 * \theta_{CH} * \theta_{CH2} + ki12 * \theta_{CHCH2} * \theta_V - k18 * \theta_{CH2} * \theta_{CH2CH3} + ki18 * \theta_{CH2CH2CH3} * \theta_V - k19 * \theta_{CH2} * \theta_{CHCH2} + ki19 * \theta_{CH2CHCH2} * \theta_V - 2 * k25 * \theta_{CH2} * \theta_{CH2} + 2 * ki25 * \theta_{CH2CH2} * \theta_V;$$

$$\frac{\mathrm{d}\theta_{CH3}}{\mathrm{d}t} = -k1 * \theta_{CH3} * \theta_H + ki1 * \theta_{CH4gas} * \theta_V * \theta_V + k8 * \theta_{CH2} * \theta_H - ki8 * \theta_{CH3} * \theta_V + k10 * \theta_{CH3\_4f} * \theta_V - ki10 * \theta_{CH3} * \theta_V - k11 * \theta_{CH2} * \theta_{CH3} + ki11 * \theta_{CH2CH3} * \theta_V - k13 * \theta_{CH} * \theta_{CH3} + ki13 * \theta_{CHCH3} * \theta_V;$$

$$\frac{\mathrm{d}\theta_{CH3\_4f}}{\mathrm{d}t} = +k9 * \theta_{CH2} * \theta_H - ki9 * \theta_{CH3\_4f} * \theta_V - k10 * \theta_{CH3\_4f} * \theta_V + ki10 * \theta_{CH3} * \theta_V;$$

$$\frac{\mathrm{d}\theta_{CHCH}}{\mathrm{d}t} = -k2 * \theta_{CHCH} * \theta_{non} + ki2 * \theta_{CHCHgas} * \theta_V - k14 * \theta_{CHCH} * \theta_H + ki14 *$$

$\theta_{CHCH2} * \theta_V + k24 * \theta_{CH} * \theta_{CH} - ki24 * \theta_{CHCH} * \theta_V;$

$\frac{\mathrm{d}\theta_{CHCH2}}{\mathrm{d}t} = +k12 * \theta_{CH} * \theta_{CH2} - ki12 * \theta_{CHCH2} * \theta_V + k14 * \theta_{CHCH} * \theta_H - ki14 * \theta_{CHCH2} * \theta_V - k15 * \theta_{CHCH2} * \theta_H + ki15 * \theta_{CHCH3} * \theta_V - k16 * \theta_{CHCH2} * \theta_H + ki16 * \theta_{CH2CH2} * \theta_V - k19 * \theta_{CH2} * \theta_{CHCH2} + ki19 * \theta_{CH2CHCH2} * \theta_V;$

$\frac{\mathrm{d}\theta_{CH2CH2}}{\mathrm{d}t} = -k3 * \theta_{CH2CH2} * \theta_{non} + ki3 * \theta_{CH2CH2gas} * \theta_V + k16 * \theta_{CHCH2} * \theta_H - ki16 * \theta_{CH2CH2} * \theta_V + k25 * \theta_{CH2} * \theta_{CH2} - ki25 * \theta_{CH2CH2} * \theta_V + k26 * \theta_{CHCH3} * \theta_V - ki26 * \theta_{CH2CH2} * \theta_V;$

$\frac{\mathrm{d}\theta_{CHCH3}}{\mathrm{d}t} = +k13 * \theta_{CH} * \theta_{CH3} - ki13 * \theta_{CHCH3} * \theta_V + k15 * \theta_{CHCH2} * \theta_H - ki15 * \theta_{CHCH3} * \theta_V - k17 * \theta_{CHCH3} * \theta_H + ki17 * \theta_{CH2CH3} * \theta_V - k20 * \theta_{CH} * \theta_{CHCH3} + ki20 * \theta_{CHCHCH3} * \theta_V - k26 * \theta_{CHCH3} * \theta_V + ki26 * \theta_{CH2CH2} * \theta_V;$

$\frac{\mathrm{d}\theta_{CH2CH3}}{\mathrm{d}t} = +k11 * \theta_{CH2} * \theta_{CH3} - ki11 * \theta_{CH2CH3} * \theta_V + k17 * \theta_{CHCH3} * \theta_H - ki17 * \theta_{CH2CH3} * \theta_V - k18 * \theta_{CH2} * \theta_{CH2CH3} + ki18 * \theta_{CH2CH2CH3} * \theta_V;$

$\frac{\mathrm{d}\theta_{CH2CHCH2}}{\mathrm{d}t} = +k19 * \theta_{CH2} * \theta_{CHCH2} - ki19 * \theta_{CH2CHCH2} * \theta_V - k22 * \theta_{CH2CHCH2} * \theta_H + ki22 * \theta_{CH2CHCH3} * \theta_V;$

$\frac{\mathrm{d}\theta_{CHCHCH3}}{\mathrm{d}t} = +k20 * \theta_{CH} * \theta_{CHCH3} - ki20 * \theta_{CHCHCH3} * \theta_V - k23 * \theta_{CHCHCH3} * \theta_H + ki23 * \theta_{CH2CHCH3} * \theta_V;$

$\frac{\mathrm{d}\theta_{CH2CHCH3}}{\mathrm{d}t} = -k4 * \theta_{CH2CHCH3} * \theta_{non} + ki4 * \theta_{CH2CHCH3gas} * \theta_V + k21 * \theta_{CH2CH2CH3} * \theta_V - ki21 * \theta_{CH2CHCH3} * \theta_H + k22 * \theta_{CH2CHCH2} * \theta_H - ki22 * \theta_{CH2CHCH3} * \theta_V + k23 * \theta_{CHCHCH3} * \theta_H - ki23 * \theta_{CH2CHCH3} * \theta_V;$

$\frac{\mathrm{d}\theta_{CH2CH2CH3}}{\mathrm{d}t} = +k18 * \theta_{CH2} * \theta_{CH2CH3} - ki18 * \theta_{CH2CH2CH3} * \theta_V - k21 * \theta_{CH2CH2CH3} *$

$\theta_V + ki21 * \theta_{CH2CHCH3} * \theta_H$;

$\frac{\mathrm{d}\theta_V}{\mathrm{d}t} = +2 * k1 * \theta_{CH3} * \theta_H - 2 * ki1 * \theta_{CH4gas} * \theta_V * \theta_V + k2 * \theta_{CHCH} * \theta_{non} - ki2 * \theta_{CHCHgas} * \theta_V + k3 * \theta_{CH2CH2} * \theta_{non} - ki3 * \theta_{CH2CH2gas} * \theta_V + k4 * \theta_{CH2CHCH3} * \theta_{non} - ki4 * \theta_{CH2CHCH3gas} * \theta_V + 2 * k5 * \theta_H * \theta_H - 2 * ki5 * \theta_{H2gas} * \theta_V * \theta_V + k6 * \theta_C * \theta_H - ki6 * \theta_{CH} * \theta_V + k7 * \theta_{CH} * \theta_H - ki7 * \theta_{CH2} * \theta_V + k8 * \theta_{CH2} * \theta_H - ki8 * \theta_{CH3} * \theta_V + k9 * \theta_{CH2} * \theta_H - ki9 * \theta_{CH3\_4f} * \theta_V - k10 * \theta_{CH3\_4f} * \theta_V + ki10 * \theta_{CH3} * \theta_V + k10 * \theta_{CH3\_4f} * \theta_V - ki10 * \theta_{CH3} * \theta_V + k11 * \theta_{CH2} * \theta_{CH3} - ki11 * \theta_{CH2CH3} * \theta_V + k12 * \theta_{CH} * \theta_{CH2} - ki12 * \theta_{CHCH2} * \theta_V + k13 * \theta_{CH} * \theta_{CH3} - ki13 * \theta_{CHCH3} * \theta_V + k14 * \theta_{CHCH} * \theta_H - ki14 * \theta_{CHCH2} * \theta_V + k15 * \theta_{CHCH2} * \theta_H - ki15 * \theta_{CHCH3} * \theta_V + k16 * \theta_{CHCH2} * \theta_H - ki16 * \theta_{CH2CH2} * \theta_V + k17 * \theta_{CHCH3} * \theta_H - ki17 * \theta_{CH2CH3} * \theta_V + k18 * \theta_{CH2} * \theta_{CH2CH3} - ki18 * \theta_{CH2CH2CH3} * \theta_V + k19 * \theta_{CH2} * \theta_{CHCH2} - ki19 * \theta_{CH2CHCH2} * \theta_V + k20 * \theta_{CH} * \theta_{CHCH3} - ki20 * \theta_{CHCHCH3} * \theta_V - k21 * \theta_{CH2CH2CH3} * \theta_V + ki21 * \theta_{CH2CHCH3} * \theta_H + k22 * \theta_{CH2CHCH2} * \theta_H - ki22 * \theta_{CH2CHCH3} * \theta_V + k23 * \theta_{CHCHCH3} * \theta_H - ki23 * \theta_{CH2CHCH3} * \theta_V + k24 * \theta_{CH} * \theta_{CH} - ki24 * \theta_{CHCH} * \theta_V + k25 * \theta_{CH2} * \theta_{CH2} - ki25 * \theta_{CH2CH2} * \theta_V - k26 * \theta_{CHCH3} * \theta_V + ki26 * \theta_{CH2CH2} * \theta_V + k26 * \theta_{CHCH3} * \theta_V - ki26 * \theta_{CH2CH2} * \theta_V - k27 * \theta_{OH} * \theta_V + ki27 * \theta_{Oxy} * \theta_H - k28 * \theta_{H2O} * \theta_V + ki28 * \theta_{OH} * \theta_H$;

$\frac{\mathrm{d}\theta_H}{\mathrm{d}t} = -k1 * \theta_{CH3} * \theta_H + ki1 * \theta_{CH4gas} * \theta_V * \theta_V - 2 * k5 * \theta_H * \theta_H + 2 * ki5 * \theta_{H2gas} * \theta_V * \theta_V - k6 * \theta_C * \theta_H + ki6 * \theta_{CH} * \theta_V - k7 * \theta_{CH} * \theta_H + ki7 * \theta_{CH2} * \theta_V - k8 * \theta_{CH2} * \theta_H + ki8 * \theta_{CH3} * \theta_V - k9 * \theta_{CH2} * \theta_H + ki9 * \theta_{CH3\_4f} * \theta_V - k14 * \theta_{CHCH} * \theta_H + ki14 * \theta_{CHCH2} * \theta_V - k15 * \theta_{CHCH2} * \theta_H + ki15 * \theta_{CHCH3} * \theta_V - k16 * \theta_{CHCH2} * \theta_H + ki16 * \theta_{CH2CH2} * \theta_V - k17 * \theta_{CHCH3} * \theta_H + ki17 * \theta_{CH2CH3} * \theta_V + k21 * \theta_{CH2CH2CH3} * \theta_V - ki21 * \theta_{CH2CHCH3} * \theta_H - k22 * \theta_{CH2CHCH2} * \theta_H + ki22 * \theta_{CH2CHCH3} * \theta_V - k23 * \theta_{CHCHCH3} * \theta_H + ki23 *$

$$\theta_{CH2CHCH3} * \theta_V + k27 * \theta_{OH} * \theta_V - ki27 * \theta_{Oxy} * \theta_H + k28 * \theta_{H2O} * \theta_V - ki28 * \theta_{OH} * \theta_H;$$

$$\frac{\mathrm{d}\theta_{OH}}{\mathrm{d}t} = -k27 * \theta_{OH} * \theta_V + ki27 * \theta_{Oxy} * \theta_H + k28 * \theta_{H2O} * \theta_V - ki28 * \theta_{OH} * \theta_H;$$

$$\frac{\mathrm{d}\theta_{H2O}}{\mathrm{d}t} = -k28 * \theta_{H2O} * \theta_V + ki28 * \theta_{OH} * \theta_H;$$

$$\frac{\mathrm{d}\theta_{Oxy}}{\mathrm{d}t} = +k27 * \theta_{OH} * \theta_V - ki27 * \theta_{Oxy} * \theta_H;$$